Longitudinal Locomotion Assessment to Study Neurodegeneration in *C. elegans* Models of Tauopathies

Inauguraldissertation

zur

Erlangung der Würde eines Doktors der Philosophie

vorgelegt der

Philosophisch-Naturwissenschaftlichen Fakultät

der Universität Basel

von

Gabriel Schweighauser

aus Basel, Basel-Stadt

Basel, 2018

Genehmigt von der Philosophisch-Naturwissenschaftlichen Fakultät

auf Antrag von

Prof. Dr. Henning Stahlberg, Prof. Dr. Markus Tolnay & Prof. Dr. Dominique Glauser

Basel, den 12. Dezember 2017

Prof. Dr. Martin Spiess, Dekan

Abstract

Tauopathies are a group of neurodegenerative diseases defined by the aggregation of abnormally phosphorylated protein tau. The cause for neurodegeneration observed in tauopathies is not known. The discovery of mutations in the gene encoding for tau in familial cases of FTDP-17, a hereditary tauopathy, emphasized the importance of tau in these diseases. This led to the creation of animal models expressing human tau containing mutations found in FTDP-17, recapitulating some of the aspects of the disease, including neurodegeneration and tau aggregation. Reports on the consequences of human tau expression in the neurons of *C. elegans* are partially contradictory, especially with regard to their locomotor phenotype. In this work, we replicated *C. elegans* models of tauopathies and performed immunohistochemical and locomotion assessments. We created 23 genomically integrated strains pan-neuronally expressing either wild type or mutated human tau. In agreement with published reports, immunohistochemistry revealed no difference between wild type or mutated human tau with regard to phosphorylation status. To obtain lifelong, longitudinal recordings of several hundred worms, we developed a novel worm tracking system which we termed Robot-Assisted Plate Imaging Device (RAPID). Using RAPID, we recorded the stimulated locomotor performance of human tau-expressing worms, exceeding the number of all reported observations combined by two orders of magnitude. Our data indicate no pronounced locomotor phenotype in those transgenic worms, arguing against the reported neurotoxic effect of tau in *C. elegans*.

Acknowledgements

My sincere thanks go out to Prof. Markus Tolnay who supported me throughout my work and for his encouragements during difficult phases of this project. His guidance enabled me to develop the necessary skills to accomplish this work. His patience for me and our project I do not take for granted. Dr. Jürgen Hench with whom I worked closely initiated this project. He was brave enough to accept me as a PhD student, although I was lacking all the required skills and had not seen a single *C. elegans* in my entire life. I thank him for teaching me all I needed to know about the work with the worms and a whole lot more. He managed to transfer some of his enthusiasm and wide interests to me and helped me to stay motivated and finish my thesis. I would also like to express my gratitude to Prof. Henning Stahlberg, who made me aware of this PhD position and insisted that I apply although I was initially not excited about the project reading the description. This changed, once I met Dr. Jürgen Hench and spent a day with him and the worms.

Dr. Roberta Diehl Rodriguez joined our group in 2014 and spent an entire year with us to perfect the worm block technique. I greatly appreciate her contributions. I was fortunate to work with Dr. Florence Clavaguera who taught me the work with mice and I thank her for sharing her expertise and stimulate my interest in current advancements in the tau field. I thank Prof. Stephan Frank for helpful discussions, PD Dr. Christian Ruiz for coordinating research resources and facilities, Silke Tolnay for taking care of administration tasks, Ralph Schoch for help with organizing equipment and their installation, and Dr. Lisa Restelli and Dr. David Müller for proofreading my thesis and helpful discussion on structure and presentation. Furthermore, I thank Prof. Anne Spang, Julia Stevens, Dr. Jachen Solinger and Dr. Ivana Bratic Hench, for sharing their injection microscope, plasmids and bacteria stocks and assistance in cloning of some of the constructs. Of great help with histology were Sabine Ipsen and all technicians of the neuropathology, as well as Petra Hirschmann.

I would like to thank all my colleagues at the Institute of Pathology, especially Dr. Sefika Ozcelik and Dr. Björn Oettinghaus for their help when I was getting started.

Prof. Markus Tolnay is funded by the Swiss National Science Foundation (Grants No. 135214 and 152846) and Jürgen Hench is supported by Research Fund Junior Researchers, University Basel and the Foundation Floshield, Neuchâtel.

Lastly, I would like to thank my family for fostering my curiosity in science during my childhood and for enabling my studies at the university.

List of Abbreviations

AA	amino acids
AB	antibody
AD	Alzheimer's disease
APP	amyloid precursor protein
Aβ	amyloid β
CAA	cerebral amyloid angiopathy
EC	entorhinal cortex
EM	electron microscope / microscopy
fAD	familial Alzheimer's disease
FFPE	formalin-fixed paraffin-embedded
FTDP-17	frontotemporal lobar degeneration with parkinsonism linked to chromosme 17
FUdR	2′-deoxy-5-fluorouridine
hTau	human tau
IHC	immunohistochemistry
MAPs	microtubule-associated proteins
MAPT	microtubule-associated protein tau (gene)
mTau	murine tau
MTs	microtubules
MWT	Multi-Worm Tracker
NFTs	neurofibrillary tangles
NGM	nematode growth medium
NTs	neuropil threads
PHFs	paired helical filaments
PTMs	post-translational modifications
RAPID	Robot-Assisted Plate Imaging Device
ROI	region of interest
sAD	sporadic Alzheimer's disease
unc	uncoordinated
wt	wild type

Table of Contents

1 Introduction

1.1 Alzheimer's Disease and Tauopathies

1.1.1 Alzheimer's Disease

Alzheimer's disease (AD) is characterized by a progressive, irreversible cognitive decline which ultimately results in severe dementia (Burns and Iliffe, 2009). The clinical symptoms are accompanied by prominent neuropathological hallmarks: brain atrophy, extracellular deposits of amyloid β (Aβ) in the form of amyloid plaques, neurofibrillary tangles (NFTs) and neuropil threads (NTs) made up of intraneuronal inclusions of tau protein, as well as synaptic and neuronal loss. Aβ deposits can also be found in walls of arteries and arterioles where they cause cerebral amyloid angiopathy (CAA). Other morphological changes associated with AD are an increased number of neurons with granulovacuolar degeneration, i.e. Hirano bodies, and increased accumulation of lipofuscin as well as a larger number of corpora amylacea (Ellison et al., 2012).
The biggest risk factor for developing AD is age (Kawas et al., 2000). The incidence rate of AD increases by 0.08 % per year in the age group of 60 - 65 and raises to 6.48 % increase in incidence rate per year in age group 85+. Even though most patients suffer from sporadic AD (sAD) with unclear cause, carriers of the type 4 allele of the apolipoprotein E (APOE-ε4) have a higher risk of developing AD and a decreased age of onset (Corder et al., 1993). A small proportion of AD cases are caused by mutations in either the amyloid precursor protein (APP) from which Aβ is cleaved, or mutations in presenilin 1 (PS1) or presenilin 2 (PS2) which are part of the secretases that process APP. These autosomal dominant mutations cause familial/hereditary forms of AD (fAD) and lead to early onset of the disease, usually before the age of 65 (Van Cauwenberghe et al., 2016). These findings have resulted in the formulation of the so-called amyloid cascade hypothesis, which will be outlined in the next section.

1.1.2 Amyloid Cascade Hypothesis

Most mutations in APP, PS1, and PS2 discovered in fAD correlates with overproduction of Aβ, amyloid plaques, and CAA. As patients suffering from fAD will develop all other pathological changes of sAD, including NFTs, Aβ was thought to be the initiator of these changes and much research was directed towards understanding the so-called amyloid cascade (Musiek and Holtzman, 2015). However, the occurrence and distribution of amyloid plaques neither correlates well with the progression of AD nor with neuronal loss. It has been observed that the distribution of NFTs and neuronal loss correlates with the severity of clinical AD symptoms. Hence, it was postulated that Aβ aggregation triggers the aggregation of tau into NFTs which are hypothesized to ultimately lead to neurodegeneration (Braak and Braak, 1991). Conversely, it is not understood whether tau exerts direct neurotoxicity nor how Aβ mediates a toxic effect. Ultimately, the amyloid cascade hypothesis has therefore not led to deeper insight into the pathomechanisms underlying AD. The link between Aβ overproduction and its accumulation in fAD and sAD remains enigmatic.
Amyloid plaques as well as NFTs can be found in young patients in absence of any clinical symptoms, therefore it has been speculated that there is a long-lasting "preclinical" phase of

AD (Braak and Braak, 1997). More recently, the development of PET tracers for Aβ (Klunk et al., 2004) have allowed longitudinal studies of amyloid plaques. The resulting data from human subjects support this hypothesis, since cognitively normal subjects with Aβ deposits are more likely to develop symptoms of AD later on (Morris et al., 2009) and higher amounts of Aβ deposits in healthy adults increase the risk of decline in episodic memory and language functions (Ellis et al., 2013).

1.1.3 Tauopathies

There are a number of neurodegenerative diseases, collectively termed tauopathies, that feature accumulation of insoluble tau protein. AD is the most frequent form among them. Other entities are parkinsonism-dementia complex of Guam, postencephalitic parkinsonism, dementia pugilistica, familial British dementia, progressive supranuclear palsy, corticobasal degeneration, argyrophilic grain disease, Pick's disease and frontotemporal lobar degeneration with parkinsonism linked to chromosome 17 (FTDP-17). Most of them occur in a sporadic manner (Ellison et al., 2012). The clinical symptoms vary depending on the affected brain regions, and the role of tau accumulation in these diseases is not understood (Williams, 2006). Similar to fAD, a number of mutations were found in the gene coding for tau (MAPT: microtubule-associated protein tau) which cause FTDP-17 (Rademakers et al., 2004).

1.2 Microtubule-Associated Protein Tau (*MAPT*)

1.2.1 *MAPT* Gene and Tau Isoforms

Human tau is encoded by the *MAPT* gene on chromosome 17q21 (Neve et al., 1986) and expressed in neurons, astrocytes and oligodendrocytes (Shin et al., 1991), as well as in neurons of the the peripheral nervous system and in skeletal and heart muscle (Trojanowski et al., 1989). In the adult human brain, six tau isoforms are primarily expressed which are generated through complex, tightly regulated alternative splicing reviewed in (Andreadis, 2012). The isoforms are generated by combinations of exon 2 and 3 with exon 10. Exon 3 only occurs in combination with exon 2, hence producing the six isoforms (Figure 1). The isoforms are differentially expressed with a higher expression of the shorter, 3R isoforms during development (Kosik et al., 1989). Furthermore, intron 9 of *MAPT* contains the gene for Saitohin (*STH*), which shares much of the expression pattern of tau and is of unknown function (Conrad and Vianna, 2002).

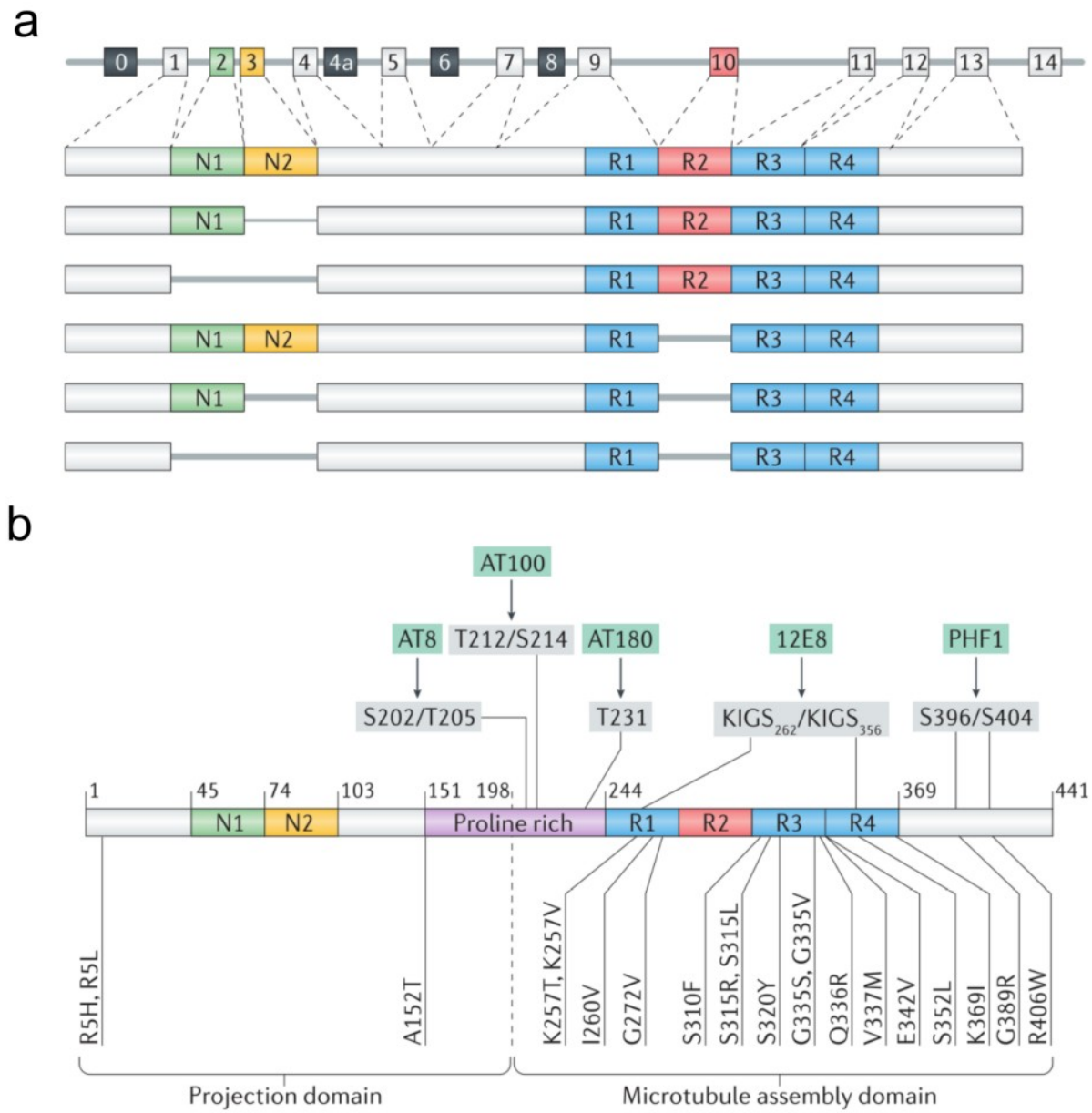

Figure 1: MAPT and Tau Isoforms

Splicing of the tau isoforms, domains, mutations and some phosphorylation sites. Human *MAPT* is spliced to generate the six tau isoforms of the adult brain (a). From top to bottom: 2N4R (441 AA), 1N4R (412 AA), 0N4R (383 AA), 2N3R (410 AA), 1N3R (381 AA), and 0N3R (352 AA). Tau is organized into different domains consisting of the N-terminal projection domain, the proline rich domain, MT assembly or MT binding domain containing the 3 or 4 MT binding repeats, and the C-terminal domain (b). The location of some of the exonic mutations found in FTDP-17 are shown as well as some anti-tau antibody epitopes (AT8, AT100, AT180, 12E8, and PHF1). Not shown are the intronic mutations following exon 10. Adapted from (Wang and Mandelkow, 2015).

1.2.2 Functions of Tau

The different domains of tau have multiple functions which are reviewed in (Guo et al., 2017), and summarized below. The N-terminal domain changes the spacing between microtubules (MTs), inhibits axonal transport, is involved in the subcellular localisation and binds to the plasma membrane as well as membrane proteins. It is thought to interact with the C-terminal domain and fold the protein into the so-called “paperclip” conformation in which tau is not bound to MTs (Jeganathan et al., 2006). The proline-rich domain is thought to be involved in signalling function, possibly through binding of several protein kinases; it might additionally interact with DNA and RNA. Tau is well known to bind to MTs through the microtubule binding repeats. In addition, these repeats can also interact with F-actin, thereby tethering MTs and actin together. Other proteins known to be bound by tau include α-synuclein, histone deacetylase 6, APOE, and PS1. Functions of the C-terminal region are not known. Tau is found in all compartments of neurons, however it is enriched in the axons (Schoenfeld and Obart, 1994).

Besides tau, there are a number of MT associated proteins or MAPs (Mandelkow and Mandelkow, 1995), with structural and functional similarities, such as MAP2 and MAP4 (Dehmelt et al., 2004). MAP1 family members share some functional similarities, but differ in the MT binding structures (Halpain and Dehmelt, 2006).

1.2.3 MAPT Mutations

So far, 44 mutations in *MAPT* are described to be clinically relevant in FTDP-17 (Cruts et al., 2012). The majority of mutations were found in the MT binding domain between exon 9 and exon 13, as well as in intron 10 (Rademakers et al., 2004). The effects of these mutations are diverse; mutations in the binding domain may change the affinity towards MTs or make it more prone to self-aggregate, while mutations in intron 10 as well as some mutations in exon 10 interfere with physiological splicing and thereby change the ratio between tau isoforms (i.e. 3R and 4R). Functional changes beyond MT binding are not yet understood, but are likely to play a role given the many functions and potential binding partners of tau.

1.2.4 Post-Translational Modifications of Tau

To orchestrate the many functions of tau, the protein can undergo a number of post-translational modifications (PTMs). The most prominent and extensively investigated is phosphorylation since aggregated tau in NFTs is found to be highly phosphorylated (Goedert et al., 1992). Therefore, phosphorylation is thought to play a role in aggregation and neurodegeneration. There are 85 potential phosphorylation sites of which 71 are found to be phosphorylated under physiological and/or pathological circumstances, summarized in (Sergeant et al., 2008). Phosphorylation is carried out by at least 20 different kinases belonging to four different groups: proline-dependent protein kinases (PDPK), non-PDPK, glycogen protein kinases and tyrosine protein kinases. Glycogen synthase kinase-3 (GSK-3), cyclin-dependent kinase-5 (cdk5), casein kinase 1 (CK1), and cyclic AMP-dependent protein kinase (PKA), were identified as major tau kinases and are intensively studied as potential drug targets in AD (Hanger et al., 2009). The physiological phosphorylation state of tau is kept in balance by the activity of kinases and phosphatases alike. The mechanism of tau hyperphosphorylation remains unclear. It has been suggested that hyperphosphorylation is

caused by downregulation of protein phosphatase 2 (PP2A), the major tau phosphatase (Liu et al., 2005).

Phosphorylation in the MT binding repeats is considered an important physiological mechanism to fine tune the MT affinity of tau. In addition, phosphorylation outside of the MT binding repeats can also alter the MT binding properties through intramolecular interactions (Goode et al., 1997). Aberrant phosphorylation is thought to release tau molecules from MTs which then may oligomerize and form aggregates.

Consequences of phosphorylation on functions of tau beyond MT binding are not well understood. Phosphorylation could lead to missorting, alter degradation, truncation, and change the interactions with many of its binding partners (Wang and Mandelkow, 2015). Furthermore, phosphorylation influences tau aggregation directly with some sites increasing the propensity (Haase et al., 2004), while others decrease the fibrillization propensity (Schneider et al., 1999).

Which sites are phosphorylated under physiological conditions and which are characteristic for aggregated tau remains a matter of debate. It was suggested that all sites phosphorylated in aggregated tau are also phosphorylated under physiological conditions (Matsuo et al., 1994), and that soluble tau would become rapidly dephosphorylated *post mortem* while aggregated tau was inaccessible to phosphatases, hence remaining phosphorylated. Nonetheless, tau molecules extracted from aggregates seem to contain more phosphate groups per molecule than soluble tau extracted from biopsies. Furthermore, a substantial amount of experimental evidence on the effect of tau phosphorylation was obtained in model systems overexpressing human tau (Götz et al., 2010). Tau phosphorylation and dephosphorylation in those models may not underlie the same carefully balanced control mechanisms as in human and therefore must be interpreted cautiously.

Apart from phosphorylation, many more PTMs were described (Martin et al., 2011), and include glycosylation, glycation, prolyl-isomerization, truncation, nitration, polyamination, ubiquitination, sumoylation, oxidation, and, more recently, acetylation (Min et al., 2010). Again, the relevance of those PTMs for tau aggregation or toxicity is not well understood.

1.2.5 Tau Aggregation

As discussed previously, intracellular inclusions of tau protein are the key pathological hallmark of tauopathies, including AD. The correlation between NFT distribution and progression of AD symptoms has lead to the hypothesis that tau aggregates are central to the disease and are the direct cause for neurodegeneration (Arriagada et al., 1992).
NFTs and NTs can be demonstrated histologically using various silver stains (Uchihara, 2007), most notably the Gallyas silver impregnation method (Gallyas, 1971). Apart from intracellular NFTs and NTs, Gallyas silver impregnation also stains extracellular tangles, which feature a less dense staining and yet outline the shapes of neurons which are themselves no longer recognizable. Hence, they are believed to be the remnants of a tangle-bearing neuron, which had died and thus left behind an extracellular “ghost tangle”. These ghost tangles are resistant to degradation, probably due to cross-linking of the proteins and are thought to remain for an extended period (Smith et al., 1994). Interestingly, the number of ghost tangles found in the hippocampus is far lower than the number of neurons that must

have died, and therefore NFTs may not be the sole reason for neuronal death (Kril et al., 2002). Furthermore, it was estimated that tangle-bearing neurons can survive up to 20 years in humans (Morsch et al., 1999). A more recent study in mice has shown that tangle-bearing neurons are able to process sensory inputs and are functional within neural circuits (Kuchibhotla et al., 2014).

Despite these findings, tau aggregates have been extensively studied biochemically and ultrastructurally, *in vivo* as well as *in vitro*. NFTs in AD were first described in 1963 as thick bundles of parallel filaments which appeared to be helical and were aptly termed paired helical filaments (PHFs) (Kidd, 1963). PHFs can be extracted from AD brains as well as assembled *in vitro* and have been studied in great detail. The core of the fibres are made up of cross-β-sheet structures (Barghorn et al., 2004) and the hexapeptide motifs (VQIXXK) of the MT binding repeats R2 and R3 are essential for the assembly into PHFs (Barghorn and Mandelkow, 2002). Recently, the structure of PHFs extracted from an AD patient was resolved with cryo-electron microscopy (Fitzpatrick et al., 2017). The core of the protofilaments are made up of the MT binding repeats 3 and 4 plus 10 amino acids following R4 (V_{306} - F_{378}) which form 8 β-sheets and arrange in a C-shaped manner. Nonetheless, the exact mechanism of how PHFs form *in vivo* is still to be elucidated.

It is thought that the assembly of PHFs *in vitro* follows a nucleated polymerization process where monomeric tau starts to form dimers, assembles into oligomers and eventually filaments which comprise the PHFs (Friedhoff et al., 1998). Tau aggregation can be induced *in vitro* and *in vivo* by “seeding” with preformed filaments.

Because of the filamentous character of NFTs in AD, Prusiner already speculated in 1984 that AD may be a prion disease with a very long incubation time (Prusiner, 1984). 30 years later, this hypothesis gained a lot of attention when the experiments outlined in the next section were performed.

1.3 Prion-Like Properties of Tau in Animal Models for Tauopathies

1.3.1 Induction of Tau Aggregation by Injection

The formation of NFTs in mice can be induced by intracerebrally injecting a host mouse expressing wild type (wt) human tau (hTau) with brain homogenates from mice expressing hTau carrying the P301S mutation (Clavaguera et al., 2009). Upon injection, the host mice progressively develop hyperphosphorylated hTau, Gallyas-positive inclusions, resembling NFTs, NTs, and coiled-bodies. Homogenates depleted of hTau did not induce such changes. The inclusions were not limited to the injection sites but also appeared in anatomically connected, yet remote brain regions in a time-dependent manner. Importantly, such injected wt hTau transgenic mice do not show any signs of additional neurodegeneration despite overt neuronal inclusions of hTau protein.
Many more aggregation inducing injection models have since been reported. Brain homogenates from mice expressing mutated hTau were injected into presymptomatic, 2 month old mice of the same genotype which then developed tangle pathology spreading from the injection sites to anatomically connected areas within 2 month, increasing in density

over time (Ahmed et al., 2014). Apart from mouse-derived inoculants, filaments generated *in vitro* from different recombinant hTau isoforms or fragments have also been successfully used to induce aggregation of tau in injected host mice (Guo et al., 2016; Iba et al., 2013; Peeraer et al., 2015).

Tau oligomers extracted from AD patients injected into wt mice caused widespread aggregation and hyperphosphorylation of endogenous murine tau (mTau) at the site of injection as well as in adjacent brain regions while PHFs did not lead to the same pathology (Lasagna-Reeves et al., 2012). However, Sarkosyl-insoluble extracts containing high molecular PHFs (Audouard et al., 2016) injected into the brain of wt and double mutant hTau-expressing mice induced Gallyas-positive inclusions. Furthermore, brain extracts from various sporadic tauopathies are able to cause Gallyas-positive deposits when injected intracerebrally in wt hTau-expressing mice, and to a lesser extent, in injected wt mice expressing only endogenous mTau (Clavaguera et al., 2013).

Lastly, we have shown that brain homogenates from symptomatic P301S mutant hTau expressing mice is able to increase Gallyas-positive deposits in the brainstem and neocortex 9 months after intraperitoneal injections into asymptomatic heterozygous mice of the same genotype, albeit to a lesser extent than injections into the hippocampus (Clavaguera et al., 2014). As with intracerebral injections, the mechanism of spreading remains to be elucidated.

1.3.2 Induction of Tau Aggregation by Expression of Mutated Tau

To study tau pathology, several mouse lines were generated expressing hTau carrying *MAPT* mutations that are associated with FTDP-17 such as G272V, P301L, P301S, V337M and R406W (Frank et al., 2008). In contrast to mice expressing wt hTau constructs, most of these mutant hTau-expressing lines spontaneously develop NFTs and NTs, and show neuronal cell loss which functionally manifests as motor and/or cognitive impairment. One mouse line that has been extensively studied in our group and was pivotal to the findings of Clavaguera et al. (Clavaguera et al., 2009) is the P301S hTau mouse model (Allen et al., 2002). These mice express the shortest 4R hTau isoform (0N4R, 383 aa) harboring the P301S mutation. The transgene expression is driven by the *thy-1.2* promoter which is particularly active in the neurons of the brainstem and spinal cord. Overexpressed P301S mutant hTau is hyperphosphorylated and localized in neuronal somata as well as in neurites. Silver-positive filamentous inclusions are found which ultrastructurally resemble PHFs of AD. Homozygous animals show a 49 % reduction of motor neurons in the spinal cord, leading to paraparesis, muscle weakness and tremor at 6 month of age.

To recapitulate the distribution and appearance of tau aggregates in AD, several mouse models were generated with mutated hTau expression restricted to the entorhinal cortex (EC) (de Calignon et al., 2012; Harris et al., 2012; Liu et al., 2012). The degree of tau pathology, spreading, and neurodegeneration observed was highly variable. Gallyas-positive inclusions, neuronal and synaptic loss was observed by de Calignon et al. in the EC as well as hTau in the hippocampus in the absence of hTau mRNA, indicating a transport of hTau between neurons (de Calignon et al., 2012). Liu et al. reported silver-positive inclusions in EC and hTau and silver-positive inclusions in the hippocampus of aged mice without neuronal loss (Liu et al., 2012). Harris et al. stated expression of mutated hTau caused

Gallyas-positive inclusions in neurons of the hippocampus, and loss of presynaptic markers in aged mice in absence of cognitive impairment (Harris et al., 2012). The differences have in part been attributed to different genetic backgrounds of the mouse strains used and spreading of hTau was ascribed to leaky expression in regions other than EC.

1.3.3 Templated Misfolding and Prion-like Properties of Tau

Human brain homogenate from various sporadic tauopathies including AD are also able to induce the aggregation of wt hTau expressed in mice (Clavaguera et al., 2013). The aggregates that are formed in the injected mice resemble the disease specific aggregates and hence the existence of tau “conformers” or tau “strains” has been proposed to give rise to the clinical phenotype. The same study showed that the aggregation inducing seeds are stably transmitted over two generations. Wild type hTau-expressing mice developed Gallyas-positive inclusions after injections with brain homogenates from either wt hTau-expressing mice injected with brain homogenates from P301S hTau-expressing mice, or brain homogenates from wt mice, injected with brain homogenates from sporadic tauopathies.

Different tau aggregation patterns or “conformations” were generated *in vitro.* HEK293 cells expressing hTau fragments consisting of the MT binding repeats develop aggregates after exposure to preformed fibrils. Distinct aggregation patterns can then be derived by clonal expansion (Sanders et al., 2014). Extracts from different clones were serially injected into the brain of mutant hTau-expressing mice for three generations and extracts from the last generation were incubated with naive cells. Remarkably, the biochemical and histological properties were conserved throughout all passages indicating these properties can be transmitted in a prion-like fashion. In addition, they used brain homogenates of human patients with various tauopathies and used them as seeds on naive cells. These seeds led to a variety of biochemical and morphological phenotypes that were distinct between the different tauopathies suggesting that each tauopathy harbours specific tau “strains” or “conformers”. Later, the same group generated even more distinct tau aggregating clones by seeding them with various preformed fibrils and used extracts from these distinct clones to inject them into the brain of mutant hTau-expressing mice (Kaufman et al., 2016). These mice developed distinct tau pathology and most notably, show different rates of progression and regions affected as defined by abnormal phosphorylation. However, no neurodegeneration nor *bona fide* NFTs were reported. Lastly, fibrils form recombinant hTau induced by AD extracts are more potent to cause abnormal tau phosphorylation when injected in wt mice, compared to fibrils generated using heparin to induce aggregation again, arguing for distinct properties of tau “strains” (Guo et al., 2016).

1.3.4 Murine Tau

Apart from a delayed maturation of neurons in primary cell culture, mTau knockout mice do not show an obvious phenotype, possibly due to compensatory mechanisms and upregulation of MAP1A expression (Dawson et al., 2001; Harada et al., 1994). There is considerable homology in the C-terminal half following exon 2 between mTau and hTau including the MT binding repeats which only differ by three amino acids. Murine tau is also able to form filaments *in vitro* (Kampers et al., 1999). Filament assembly is promoted by hyperphosphorylation and the filaments resemble filaments composed of hTau (Chohan et al., 2005). Nonetheless, mTau-expressing mice do not develop NFTs, not even under overexpression of endogenous mTau (Adams et al., 2009).

1.3.5 Surrogate Markers for Neurodegeneration

Since the discovery of hyperphosphorylated tau as major constituent of NFTs, many phosphorylation dependent anti-tau antibodies were developed to study tau phosphorylation *in situ*, some of which are summarized in Table 1 and shown in Figure 1.

Antibody	Epitope	Reference	Phosphorylation Dependent	Conformational
AT8	pSer202, pThr205	Goedert, 1995	yes	no
AT100	pThr212, pSer214	Zheng-Fischhoefer, 1998	yes	induced by heparin
AT180	pThr231	Goedert, 1994	yes	no
12E8	pSer262, pSer356	Seubert, 1995 & Litersky, 1996	yes	no
Alz50	AA 7-9, 312–342	Jicha, 1997	NA	yes
MC1	AA 7-9, 312–342	Jicha, 1997	NA	yes
PHF-1	pSer396, pSer404	Otvos, 1994	yes	no

Table 1: Anti-Tau Antibodies and Epitopes

Some anti-tau antibodies and their epitopes. Alz50 was raised against forebrain homogenate of human AD patients and MC1 was raised against PHFs immuno-affinity purified using Alz50. Epitopes are numbered according to the longest hTau isoform 2N4R, NA: not assessed.

Although tau in NFTs is hyperphosphorylated and recognized by phosphorylation-dependent antibodies, presence of phosphorylated tau is neither sufficient to assume tau aggregation nor neurodegeneration. Aggregation of tau protein can only be demonstrated by biophysical means such as sequential extraction, Gallyas silver impregnation, and electron microscopy.

Most tauopathy models expressing hTau lack essential regulatory elements which balance the phosphorylation/dephosphorylation in the human brain. In absence of significant neurodegeneration in the majority of wt hTau models, authors often use the term "tau pathology" which typically refers to a labelling with one or more of phosphorylation-dependent antibodies. The effect of NFTs on neuronal function is not well understood, but NFTs can at least be unambiguously demonstrated using various silver impregnation methods (Uchihara, 2007). There is currently no consensus on the definition of neurodegeneration: some authors describe synaptic loss, while others use the term when potentially reversible functional impairments are observed.

Instead of focusing on mimicking the biochemical or histological properties of tauopathies as surrogate markers for neurodegeneration, it may be more fertile to focus on the functional implications of tau expression in model systems.

1.4 *C. elegans* as Model System for Tauopathies

1.4.1 Protein with Tau-like Repeats

So far, only one gene of *C. elegans,* is known which is similar to mammalian *MAPT*, and thus was named protein with tau-like repeats 1 (*ptl-1*) (Goedert et al., 1996). This gene is spliced to generate two isoforms, PTL-1A and PTL-1B, containing either four or five repeats. The repeat domains of *ptl-1* roughly share 50 % sequence homology with the repeat domains of human *MAPT*, but regions outside the repeats are unrelated. Both *ptl-1* isoforms are expressed in five of the six touch neurons (ALML/R, AVM, PLML/R) and their neurites during larval stages as well as in adults. Null-mutants and deletion of the binding repeats of *ptl-1* show an accelerated appearance of structural abnormalities in the touch neurons, decreased drug sensitivity and a reduced lifespan (Chew et al., 2013). Re-expression of wt hTau in these *ptl-1* mutants does not rescue these phenotypes, suggesting hTau does not compensate for PTL-1's functions in worms. The overall MT structure in touch neurons is not disturbed in *ptl-1* knock-out worms (Gordon et al., 2008), furthermore, touch response and habituation are similar to wt worms (Swierczek et al., 2011). PTL-1 was implicated in axonal transport through an interaction with UNC-104 since *ptl-1* knock-outs show a more pronounced retrograde movement of UNC-104 (Tien et al., 2011). In summary, despite some similarities, *ptl-1* and hTau may be considered distantly related proteins only.

1.4.2 *C. elegans* Models of Tauopathies

C. elegans does not express a protein with close homology to mammalian tau. Together with the relative simplicity of the worm's nervous system, consisting of only 302 neurons in adult hermaphrodites (White et al., 1986), compensatory effects are less likely than in mouse models. This makes the nematode an ideal model to study potential toxic effects of tau and its mutant forms independently of its function in the nervous system.
This section reviews a number of hTau-expressing *C. elegans* strains with regard to the reported locomotion phenotype, structural appearance of hTau-expressing neurons, as well as biochemical properties. These aspects, summarized in Table 2, have been addressed independently of the particular aims of the respective studies, facilitating comparison.

Publication	Isoform	Mutations	Expression	Unc	Thrashing	Neuronal loss	Gaps	Morphological Analysis	Det. Insoluble Tau	Genetic Background	Selection Marker
Kraemer, 2003	1N4R	wt, V337M, P301L	pan (*aex-3p*)	yes	decreased	yes	yes	*unc-25p::gfp*, live imaging	old worms	N2, *glp-4 (bn2)*	*myo-2p::gfp*
Miyasaka, 2005	0N3R, 0N4R	wt, P301L, R406W	touch (*mec-7p*)	NA	NA	no	no	IHC	NA	N2	*rol-6 (su1006)*
Brandt, 2009	0N3R	wt, PHP, NP	pan (*rgef-1p*)	yes	decreased	no	yes	*unc-47p::gfp*, live imaging	no	*pha-1 (e2123ts)*	*pha-1* rescue
Fatouros, 2012	F3, 1N4R	F3: wt, ΔK280, I277P + I308P 1N4R: V337M	pan (F3, *rab-3p*), (1N4R, *aex-3p*)	yes	NA	no	yes	*unc-25p::gfp*, *unc-129p::mCherry*, live imaging	yes	N2	*myo-2p::mCherry*, *myo-2p::gfp*
Xie, 2014	0N3R, 0N4R, Fragments: 0N, 3R and 4R	wt	pan (*unc-119p*)	0N4R: yes, others: no	NA	no	no	*unc-119p::dsRed*, NA	NA	N2	*ges-1p::egfp*
Miyasaka, 2016	0N3R, 0N4R	0N3R: wt, 0N4R: wt, R406W, P301L	pan (*unc-119p*)	0N4R: yes, others: weak	decreased	no	no	*unc-119p::dsRed*, live imaging	no	N2	*ges-1p::egfp*
Pir, 2016	2N4R	wt, A152T	pan (*snb-1p*)	wt: weak, A152T: severe	decreased	no	yes	*unc-25p::gfp*, live imaging	no	N2	*myo-2p::gfp*, *myo-2p::mCherry*

Table 2: Summary of C. elegans Models of Tauopathies

The phenotypes are summarized with regard to locomotion, structural alterations and biochemical properties. Pan = pan-neuronal expression, Unc = uncoordinated locomotion, Gaps = discontinuities in neurites, PHP: pseudo hyperphosphorylated tau (Ser/Thr > Glu), NP: non-phosphorylated tau (Ser/Thr > Ala).

The first *C. elegans* model expressing hTau constructs was reported by Kraemer et al. in 2003 (Kraemer et al., 2003). Three hTau constructs with different isoforms were generated: hTau (1N4R, wt), hTau (1N4R, P301L) and hTau (1N4R, V337M), all driven by the pan-neuronal promoter of *aex-3*. Pharyngeal GFP expression, driven by *myo-2p*, was used as a selection marker and transgenes were genomically integrated. All strains were reported to exhibit uncoordinated locomotion (unc), which increased over time until worms were almost paralyzed by day 9. These observations were made on small cohorts by manual scoring of a thrashing assay, counting the number of body bends in liquid over a defined period of time. The data demonstrate a lower performance of all transgenic worms relative to non-transgenic wt controls. The thrashing rates for strains expressing hTau (1N4R, V337M) and hTau (1N4R, P301L) were lower than hTau (1N4R, wt). Sequential extraction (Ishihara et al., 1999) of homogenized worms leads to high salt soluble, detergent soluble and detergent insoluble fractions. In 1-day old worms, hTau was only detectable in the high salt soluble fraction but high levels of detergent soluble and detergent insoluble hTau were detected in mixed age populations, indicating an increase of insoluble hTau over time. Furthermore, hTau was phosphorylated on seven probed sites, including AT8, 12E8, and PHF-1, most of which were found in high salt soluble and detergent soluble fractions. Using fluorescence microscopy, GABAergic neurons and their processes were examined and found to display gaps in the ventral and dorsal nerve cord as well as neuronal loss, both increasing with age. Axonal degeneration was also visible ultrastructurally and non-filamentous, tau-positive accumulations were observed.

In 2005, Miyasaka et al. (Miyasaka et al., 2005) reported findings on a set of hTau lines with expression restricted to the touch neurons, driven by the promoter of *mec-7*. The isoforms used were: hTau (0N3R, wt), hTau (0N4R, wt), hTau (0N4R, P301L), and hTau (0N4R, R406W). A dominant behavioral marker, *rol-6(su1006)* (Mello et al., 1991), was used as a selection marker leading to helically twisted bodies which precludes the study of locomotion. Despite this impairment, animals were scored for touch response and touch sensitivity was reported to be progressively declining in all hTau lines, with hTau (0N4R, P301L) and hTau (0N4R, R406W) lines performing worst: 20 - 40 % of all assessed worms showed no response on day 5 after hatching. Immunohistochemistry (IHC) on freeze-cracked worms revealed loss of acetylated α-tubulin in PLMs with fewer tubulin positive PLMs detected with increasing age in hTau (0N4R, P301L) and hTau (0N4R, R406W), but not in hTau (0N4R, wt) expressing line. These neurons additionally displayed abnormal morphologies in all hTau lines, such as multiple processes emerging from a cell bodies as well as curvy and branched processes, again mutated hTau-expressing lines being more severely affected than wt hTau lines. Tau accumulation was reported based on IHC in freeze-cracked worms, and abnormal processes were also observed in absence of hTau labelling. Ultrastructurally, hTau-expressing worms showed thinner or missing MTs in PLMs but no sign of filamentous tau. Solubility was not assessed, as the amount of hTau that is expressed by the touch neurons would probably lie below the detection level in whole worm protein extracts.

Brandt et al. generated hTau constructs based on an N-terminally FLAG-tagged 0N3R isoform with the wt sequence or as pseudo hyperphosphorylated tau (PHP) in which some of the Ser/Thr residues (S198, S199, S202, T231, S235, S396, S404, S409, and S413) are substituted with Glu to reflect the charge distribution that would be carried by the phosphate groups (Brandt et al., 2009). These constructs were pan-neuronally expressed under the *rgef-1* promoter. Transgenes were expressed in *pha-1(e2123)* mutants, along with a wt copy of PHA-1 to rescue the otherwise embryonic lethal mutation at 25 °C. Hence, the hTau expression in individual worms of the same genotype can vary due to non-mendelian inheritance of the extrachromosomal transgene. A cohort of worms was scored daily for the unc phenotype. Locomotion became increasingly uncoordinated with 50 % of the non-transgenic population becoming uncoordinated by adult day 10 with day 0 defined as larval stage L4, while both hTau (0N3R, PHP) and hTau (0N3R, wt) expressing lines became unc on day 8. In a thrashing assay, worms performed progressively worse, with the hTau-expressing lines showing a decreased thrashing rate compared to non-transgenic worms. Furthermore, inhibitory motoneurons of living, anaesthetized animals were analysed using GFP expression driven by the *unc-47* promoter. The number of motoneurons on day 1, 3, and 6 of old worms did not differ between hTau and non-transgenic worms but the number of worms with at least one gap in the dorsal nerve cord was between 60-80 % in hTau (0N3R, PHP) expressing worms whereas less than 20 % of the hTau (0N3R, wt) and non-transgenic worms showed any gaps. Similarly, broadening of axons of motoneurons was more frequent in the hTau (0N3R, PHP) line compared to hTau (0N3R, wt) or non-transgenic worms. With age, hTau (0N3R, PHP) expressing worms accumulated more hTau in the detergent soluble fraction compared to hTau (0N3R, wt) line as demonstrated by sequential extraction and western blotting. Lastly, they repeated their experiments with a another hTau construct where the same Ser/Thr residues as in hTau (0N3R, PHP) are replaced with Ala, mimicking a non-phosphorylated (NP) hTau protein. This line performed worse than hTau (0N3R, wt) and hTau (0N3R, PHP) expressing worms in the thrashing assay, but showed fewer morphological neuronal alterations. There was no detergent insoluble nor Sarkosyl insoluble hTau detectable in any of the lines.

Fatouros et al. (Fatouros et al., 2012) expressed a fragment of hTau containing the four MT binding repeats (fragment F3, AA 258-360) and incorporated the deletion mutation ΔK280, yielding the F3(ΔK280) pro-aggregating construct. A second construct was created with the F3 fragment containing two additional mutations (I277P, I308P) which results in the F3(ΔK280, 277P, I308P) anti-aggregating construct. Both constructs were genomically integrated and are pan-neuronally expressed under the *rab-3* promoter. Since pro- and anti-aggregating lines were similar in their locomotion phenotype, all lines were crossed with CK10, a strain previously created (Kraemer et al., 2003), pan-neuronally expressing hTau (1N4R, V337M). The crossed pro-aggregating lines exhibit a strong unc phenotype and a more reduced locomotion speed while the anti-aggregating lines showed no unc phenotype and a less reduced locomotion speed on adult day 1. The morphology of GABAergic neurons was followed throughout development and adulthood and the number of gaps counted in analogy to earlier reports (Kraemer et al., 2003). For each line, the number of gaps decreased during larval development and increased during adulthood. The pro-aggregating line shows significantly more gaps than the control and the anti-aggregating lines. Three times more worms of the pro-aggregating lines showed gaps in cholinergic neurites compared to the reporter and anti-aggregating line. Thioflavin-S-positive speckles

were observed around the nerve ring in pro-aggregating, but not in the anti-aggregating lines. In 1 day old adults, only the pro-aggregating lines showed detergent soluble and detergent insoluble hTau in sequential extracts, whereas CK10 and anti-aggregating lines only showed hTau bands in the high salt soluble fractions. In 7 day old adults, all lines showed detergent soluble and insoluble hTau, but the amount was increased in the pro-aggregating lines by 4- and 8-fold compared to CK10.

Xie et al. (Xie et al., 2014) published work on lines expressing full length hTau (0N4R, wt), hTau (0N3R, wt) and fragments consisting of the N-terminal half without MT binding repeats hTau (0N AA 1-192, wt) and the carboxyl terminally half containing 3 or 4 MT binding repeats, hTau (3R AA 193-352 , wt) and hTau (4R AA 193-383, wt), all of which were N-terminally tagged with a fragment of UNC-119 and pan-neuronally expressed under the *unc-119* promoter. Day 1 adults of each lines were scored for unc phenotype. High expression of hTau (0N4R, wt) leads to ~76 % of the worm population being unc, but low expression only cause ~6 % unc worms. Furthermore, hTau (0N3R, wt) expression did not cause unc although expression levels were comparable to hTau (0N4R, wt). Almost all worms expressing hTau (4R, wt) fragments at low levels were unc, while hTau (0N, wt) and hTau (3R, wt) fragment expression did not lead to an unc phenotype. Morphologically, hTau (0N3R, wt) and hTau (0N4R, wt) expressing worms did not show any gaps but their processes appeared kinked. The number of kinks per unit length increased with age and was always higher in hTau (0N4R, wt) worms. The hTau expressed in the worms was phosphorylated as detected by size difference on western blots after phosphatase treatment.

In 2016, Miyasaka et al. (Miyasaka et al., 2016) used the strains listed above (Xie et al., 2014), namely N-terminally UNC-119-tagged hTau (0N4R, wt), hTau (0N3R, wt), and the carboxyl terminal fragment containing 4 MT binding repeats hTau (4R AA 193-383, wt). In addition, they generated lines with FTDP-17 mutations, hTau (0N4R, R406W) and hTau (0N4R, P301L). All constructs were expressed pan-neuronally under the *unc-119* promoter. Again, these worm lines were subjected to a behavioral analysis by scoring them for unc phenotype according to the motion pattern by an observer and more quantitatively by a thrashing assay. The lines with high expression of hTau (0N4R, wt) and hTau (0N4R, P301L) were most affected while the appearance of unc phenotype was moderate in hTau (0N3R, wt) and hTau (0N4R, R406W) on day 2 after hatching. The number of worms affected by the unc phenotype increased on day 5 after hatching, and remained most severe in the high expressing hTau (0N4R, wt) line. The thrashing assay was performed two and five days after hatching and the performance significantly decreased between the two timepoints in high expressing hTau (0N4R, wt), hTau (0N4R, R406W) and hTau (0N4R, P301L) lines. Neuritic abnormalities were observed in all hTau-expressing lines with neurites showing kinks and protrusions. The number of worms affected by abnormalities increased with age from 80 % to almost 100 % in the hTau (0N4R, wt) high expressing line, and it increased in all lines between day 5 and day 10 after hatching and further increased in all lines except in hTau (0N4R, R406W), where the number of worms affected by kinks decreased between day 10 and day 20. The authors report that kinking and protrusions increase in individual worms leading to fragmentation. Unfortunately, this data is not shown in the publication. IHC on paraffin sections revealed more intense labelling for hTau at the bends of the kinks but no NFTs and a loss of microtubules in the kinked neurites. All phosphorylation dependent antibodies (including AT8 and AT100) were positive in all hTau-expressing lines and an

improved protocol of sequential extraction revealed high salt soluble and traces of detergent soluble, but no detergent insoluble hTau 18 days after hatching.

Lastly in 2016, Pir et al. (Pir et al., 2016) published findings on constructs hTau (2N4R, wt) and hTau (2N4R, A152T), pan-neuronally expressed under the *snb-1* promoter. While the expression of hTau (2N4R, wt) led to a mild, dose-dependent unc phenotype, day 1 adults of hTau (2N4R, A152T) expressing lines were strongly paralytic and were not able to propel their bodies. This was reflected in a thrashing assay, were day 1 adults of hTau (2N4R, wt) lines showed 30 and 20 thrashes in 30s, while the hTau (2N4R, A152T) lines only showed 2 thrashes in the same period of time.
GFP expression in the GABAergic neurons of day 1 adults revealed gaps in the ventral nerve cord of hTau (2N4R, wt) lines, which were more severe in the high expressing line. hTau (2N4R, A152T) lines showed more severe gaps in the ventral and dorsal nerve cord, with longer stretches of either cord missing. More gross morphological abnormalities were reported in touch neurons. Branching and bending of the neural processes was prevalent in hTau (2N4R, A152T) expressing lines and less frequent in hTau (2N4R, wt) expressing lines, the proportion of animals affected by these aberrations increases between 1 day and 5 day old adults. Interestingly, the most severely affected line was the low expressing hTau (2N4R, A152T) line. High salt soluble, and detergent soluble, but no detergent insoluble hTau could be detected by sequential extraction and western blotting in all lines except the control line CK10 by Kraemer et al. which also showed a detergent insoluble hTau band on a population of mixed stage animals. Additional experiments were performed with non-integrated constructs of full-length hTau harbouring A152T mutation as well as the “anti-aggregation” mutations I277P and I308P used by Fatouros et al. and described above. These worms showed the same unc phenotype and a poor performance in the thrashing assay, comparable with the non-integrated worms solely harbouring the A152T mutation and significantly worse than the wt hTau-expressing worms. Tau fragments of the N-terminal half without the MT binding repeats (AA 1-243) harbouring the A152T or as wt construct did not cause an obvious phenotype and performed equally well.

1.4.3 Quantifying Locomotion

Since the phenotype “uncoordinated locomotion” is not well defined, observer independent methods of locomotion quantification should be employed. While thrashing assays (Keith et al., 2014) are more objective, they are nonetheless carried out by an experimenter. This makes observations on a large number of worms tedious and error prone. To overcome observer bias, automated systems were developed to analyse thrashing assays using computer-vision based approaches (Buckingham and Sattelle, 2009; Restif and Metaxas, 2008; Tsechpenakis et al., 2008) or using spectroscopic systems (Simonetta and Golombek, 2007).

To study the locomotion on solid media, many (semi-)automated systems were developed, known as worm trackers (Husson, 2012). Worm trackers can be grouped into three categories: (1) differentiation of worm behaviour and measuring the duration of each behaviour, such as crawling, egg laying or resting, (2) analysis of a specific behaviour such as locomotion and e.g. measuring velocity, bending angles, and reversals or (3) a combination of (1) and (2) to parametrize the entire worm behaviour (Buckingham and Sattelle, 2008). To measure the locomotor performance of an individual worm over time,

some requirements have to be met: worms need to be identifiable throughout the assay and the method should allow for a reasonable number of worms to be assessed per experiment. The first requirement excludes all methods which gain their throughput by having multiple worms per plate, since the individual worms can not be labelled. The need for a reasonable throughput implies no manual interventions between measurements. Hence, worms need to be kept and imaged on seeded plates, and the tracking algorithm is required to work robustly under variable imaging conditions. Since more advanced worm trackers analyse worm behaviour by segmenting the worm from the background, these algorithms can not be employed using seeded plates, where illumination changes with the location of the worm, such as within and outside the of bacterial lawn, or, at its edge. To fit all those needs, we developed a novel type of worm tracker. This system, termed RAPID, is discussed in the next sectionManuscript: RAPID - High-throughput standardized health modelling in C. elegans.

1.5 Summary

Much effort has been put into research of tau and tauopathies, since tau was discovered to be the main constituent of paired helical filaments of Alzheimer's disease more than 30 years ago. A clear link between tau and neurodegeneration was established with the discovery of *MAPT* mutations in FTDP-17. This has enabled the creation of model systems recapitulating some of the histological hallmarks of tauopathies including NFTs and neurodegeneration. Yet the fundamental questions remain: How does tau form aggregates? How does tau mediate neurodegeneration and are these two processes causally linked? Moreover, is neurodegeneration caused by a loss of function of tau or does tau exert a direct toxic effect? If so, what is the neurotoxic species and how does it arise? All these questions are a matter of debate and no pathomechanism for tau-mediated neurodegeneration has been established. *C. elegans* has been used to study the effects of wild type and mutated hTau expression in neurons by several groups. The reported phenotypes vary regarding locomotion, structural aberrations and biochemical properties of tau. Some of the discrepancies may be attributed to the different hTau isoforms, promoters and expression levels. Unfortunately, most of the locomotion phenotypes and the classification of unc were based on arbitrary definitions and scored by an observer.

1.6 Aim of this Work

In this work, we intended to replicate a reported model of tauopathy and assess the immunohistochemical and functional changes induced by expression of wild type and mutated hTau in neurons of *C. elegans* using histology and worm-tracking.

1.7 References

Adams, S.J., Crook, R.J.P., Deture, M., Randle, S.J., Innes, A.E., Yu, X.Z., Lin, W.-L., Dugger, B.N., McBride, M., Hutton, M., Dickson, D.W., McGowan, E., 2009. Overexpression of wild-type murine tau results in progressive tauopathy and neurodegeneration. Am. J. Pathol. 175, 1598–1609. doi:10.2353/ajpath.2009.090462

Ahmed, Z., Cooper, J., Murray, T.K., Garn, K., McNaughton, E., Clarke, H., Parhizkar, S., Ward, M.A., Cavallini, A., Jackson, S., Bose, S., Clavaguera, F., Tolnay, M., Lavenir, I., Goedert, M., Hutton, M.L., O'Neill, M.J., 2014. A novel in vivo model of tau propagation with rapid and progressive neurofibrillary tangle pathology: The pattern of spread is determined by connectivity, not proximity. Acta Neuropathol. 127, 667–683. doi:10.1007/s00401-014-1254-6

Allen, B., Ingram, E., Takao, M., Smith, M.J., Jakes, R., Virdee, K., Yoshida, H., Holzer, M., Craxton, M., Emson, P.C., Atzori, C., Migheli, A., Crowther, R.A., Ghetti, B., Spillantini, M.G., Goedert, M., 2002. Abundant tau filaments and nonapoptotic neurodegeneration in transgenic mice expressing human P301S tau protein. J. Neurosci. 22, 9340–51.

Andreadis, A., 2012. Tau splicing and the intricacies of dementia. J. Cell. Physiol. 227, 1220–1225. doi:10.1002/jcp.22842

Arriagada, P. V, Growdon, J.H., Hedleywhyte, E.T., Hyman, B.T., 1992. Neurofibrillary Tangles But Not Senile Plaques Parallel Duration and Severity of Alzheimers-Disease. Neurology 42, 631–639. doi:10.1212/WNL.42.3.631

Audouard, E., Houben, S., Masaracchia, C., Yilmaz, Z., Suain, V., Authelet, M., De Decker, R., Buée, L., Boom, A., Leroy, K., Ando, K., Brion, J.P., 2016. High–Molecular-Weight Paired Helical Filaments from Alzheimer Brain Induces Seeding of Wild-Type Mouse Tau into an Argyrophilic 4R Tau Pathology in Vivo. Am. J. Pathol. 186, 2709–2722. doi:10.1016/j.ajpath.2016.06.008

Barghorn, S., Davies, P., Mandelkow, E., 2004. Tau paired helical filaments from Alzheimer's disease brain and assembled in vitro are based on beta-structure in the core domain. Biochemistry 43, 1694–1703. doi:10.1021/bi0357006

Barghorn, S., Mandelkow, E., 2002. Toward a unified scheme for the aggregation of tau into Alzheimer paired helical filaments. Biochemistry 41, 14885–14896. doi:10.1021/bi026469j

Braak, H., Braak, E., 1991. Neuropathological stageing of Alzheimer-related changes. Acta Neuropathol. 82, 239–259. doi:10.1007/BF00308809

Braak and Braak, 1997. Frequency of stages of Alzheimer-related lesions in different age categories. Neurobiol. Aging 18, 377-9-92.

Brandt, R., Gergou, A., Wacker, I., Fath, T., Hutter, H., 2009. A Caenorhabditis elegans model of tau hyperphosphorylation: induction of developmental defects by transgenic overexpression of Alzheimer's disease-like modified tau. Neurobiol. Aging 30, 22–33. doi:10.1016/j.neurobiolaging.2007.05.011

Buckingham, S.D., Sattelle, D.B., 2009. Fast, automated measurement of nematode swimming (thrashing) without morphometry. BMC Neurosci. 10, 84. doi:10.1186/1471-2202-10-84

Buckingham, S.D., Sattelle, D.B., 2008. Strategies for automated analysis of C. elegans locomotion. Invertebr. Neurosci. 8, 121–131. doi:10.1007/s10158-008-0077-3

Burns, A., Iliffe, S., 2009. Alzheimer's disease. BMJ 158, 1–13. doi:10.1038/461895a

Chew, Y.L., Fan, X., Götz, J., Nicholas, H.R., 2013. PTL-1 regulates neuronal integrity and lifespan in C. elegans. J. Cell Sci. 126, 2079–91. doi:10.1242/jcs.jcs124404

Chohan, M.O., Haque, N., Alonso, A., El-Akkad, E., Grundke-Iqbal, I., Grover, A., Iqbal, K., 2005. Hyperphosphorylation-induced self assembly of murine tau: A comparison with human tau. J. Neural Transm. 112, 1035–1047. doi:10.1007/s00702-004-0241-9

Clavaguera, F., Akatsu, H., Fraser, G., Crowther, R.A., Frank, S., Hench, J., Probst, A., Winkler, D.T., Reichwald, J., Staufenbiel, M., Ghetti, B., Goedert, M., Tolnay, M., 2013. Brain homogenates from human tauopathies induce tau inclusions in mouse brain. Proc. Natl. Acad. Sci. U. S. A. 110, 9535–40. doi:10.1073/pnas.1301175110

Clavaguera, F., Bolmont, T., Crowther, R.A., Abramowski, D., Frank, S., Probst, A., Fraser, G., Stalder, A.K., Beibel, M., Staufenbiel, M., Jucker, M., Goedert, M., Tolnay, M., 2009. Transmission and spreading of tauopathy in transgenic mouse brain. Nat. Cell Biol. 11, 909–13. doi:10.1038/ncb1901

Clavaguera, F., Hench, J., Lavenir, I., Schweighauser, G., Frank, S., Goedert, M., Tolnay, M., 2014. Peripheral administration of tau aggregates triggers intracerebral tauopathy in transgenic mice. Acta Neuropathol. 127, 299–301. doi:10.1007/s00401-013-1231-5

Conrad, C., Vianna, C., 2002. A polymorphic gene nested within an intron of the tau gene: implications for Alzheimer's disease. Proc. … 99, 7751–7756. doi:10.1073/pnas.112194599

Corder, E., Saunders, A., Strittmatter, W., Schmechel, D., Gaskell, P., Small, G., Roses, A., Haines, J., Pericak-Vance, M., 1993. Gene dose of apolipoprotein E type 4 allele and the risk of Alzheimer's disease in late onset families. Science (80-.). 261, 921–923. doi:10.1126/science.8346443

Cruts, M., Theuns, J., Broeckhoven, C. Van, 2012. Locus-Specific Mutation Databases for Neurodegenerative Brain Diseases 2–6. doi:10.1002/humu.22117

Dawson, H.N., Ferreira, A., Eyster, M. V, Ghoshal, N., Binder, L.I., Vitek, M.P., 2001. Inhibition of neuronal maturation in primary hippocampal neurons from tau deficient mice.

de Calignon, A., Polydoro, M., Suárez-Calvet, M., William, C., Adamowicz, D.H., Kopeikina, K.J., Pitstick, R., Sahara, N., Ashe, K.H., Carlson, G.A., Spires-Jones, T.L., Hyman, B.T., 2012. Propagation of Tau Pathology in a Model of Early Alzheimer's Disease. Neuron 73, 685–697. doi:10.1016/j.neuron.2011.11.033

Dehmelt, L., Halpain, S., Hale, C., Boer, P. de, et al., 2004. The MAP2/Tau family of microtubule-associated proteins. Genome Biol. 6, 204. doi:10.1186/gb-2004-6-1-204

Ellis, K.A., Lim, Y.Y., Harrington, K., Ames, D., Bush, A.I., Darby, D., Martins, R.N., Masters, C.L., Rowe, C.C., Savage, G., Szoeke, C., Villemagne, V.L., Maruff, P., 2013. Decline in cognitive function over 18 months in healthy older adults with high amyloid-β. J. Alzheimer's Dis. 34, 861–871. doi:10.3233/JAD-122170

Ellison, D., Love, S., Cardao Chimelli, L.M., Harding, B., Lowe, J., Vinters, H. V., Brandner, S., Yong, W., 2012. Neuropathology, 3rd ed.

Fatouros, C., Pir, G.J., Biernat, J., Koushika, S.P., Mandelkow, E., Mandelkow, E.-M., Schmidt, E., Baumeister, R., 2012. Inhibition of tau aggregation in a novel Caenorhabditis elegans model of tauopathy mitigates proteotoxicity. Hum. Mol. Genet. 21, 3587–603. doi:10.1093/hmg/dds190

Fitzpatrick, A.W.P., Falcon, B., He, S., Murzin, A.G., Murshudov, G., Garringer, H.J., Crowther, R.A., Ghetti, B., Goedert, M., Scheres, S.H.W., 2017. Cryo-EM structures of tau filaments from Alzheimer's disease. Nature. doi:10.1038/nature23002

Frank, S., Clavaguera, F., Tolnay, M., 2008. Tauopathy models and human neuropathology: similarities and differences. Acta Neuropathol. 115, 39–53. doi:10.1007/s00401-007-0291-9

Friedhoff, P., von Bergen, M., Mandelkow, E.M., Davies, P., Mandelkow, E., 1998. A nucleated assembly mechanism of Alzheimer paired helical filaments. Proc. Natl. Acad. Sci. U. S. A. 95, 15712–15717. doi:10.1073/pnas.95.26.15712

Gallyas, F., 1971. Silver staining of Alzheimer's neurofibrillary changes by means of physical development. Acta Morphol. Acad. Sci. Hung. 19, 1–8.

Goedert, M., Baur, C.P., Ahringer, J., Jakes, R., Hasegawa, M., Spillantini, M.G., Smith, M.J., Hill, F., 1996. PTL-1, a microtubule-associated protein with tau-like repeats from the nematode Caenorhabditis elegans. J. Cell Sci. 109 (Pt 1, 2661–72.

Goedert, M., Spillantini, M.G., Cairns, N.J., Crowther, R.A., 1992. Tau proteins of alzheimer paired helical filaments: Abnormal phosphorylation of all six brain isoforms. Neuron 8, 159–168. doi:10.1016/0896-6273(92)90117-V

Goedert, M., Jakes, R., Crowther, R.A., Cohen, P., Vanmechelen, E., Vandermeeren, M., Cras, P., 1994. Epitope mapping of monoclonal antibodies to the paired helical filaments of Alzheimer's disease: identification of phosphorylation sites in tau protein. Biochem. J. 301 (Pt 3, 871–877. doi:10.1042/bj3010871

Goedert, M., Jakes, R., Vanmechelen, E., 1995. Monoclonal antibody AT8 recognises tau protein phosphorylated at both serine 202 and threonine 205. Neurosci. Lett. 189, 167–170. doi:10.1016/0304-3940(95)11484-E

Goode, B.L., Denis, P.E., Panda, D., Radeke, M.J., Miller, H.P., Wilson, L., Feinstein, S.C., 1997. Functional interactions between the proline-rich and repeat regions of tau enhance microtubule binding and assembly. Mol. Biol. Cell 8, 353–65.

Gordon, P., Hingula, L., Krasny, M.L., Swienckowski, J.L., Pokrywka, N.J., Raley-Susman, K.M., 2008. The invertebrate microtubule-associated protein PTL-1 functions in mechanosensation and development in Caenorhabditis elegans. Dev. Genes Evol. 218, 541–551. doi:10.1007/s00427-008-0250-z

Götz, J., Gladbach, A., Pennanen, L., van Eersel, J., Schild, A., David, D., Ittner, L.M., 2010. Animal models reveal role for tau phosphorylation in human disease. Biochim. Biophys. Acta - Mol. Basis Dis. 1802, 860–871. doi:10.1016/j.bbadis.2009.09.008

Guo, J.L., Narasimhan, S., Changolkar, L., He, Z., Stieber, A., Zhang, B., Gathagan, R.J., Iba, M., McBride, J.D., Trojanowski, J.Q., Lee, V.M.Y., 2016. Unique pathological tau conformers from Alzheimer's brains transmit tau pathology in nontransgenic mice. J. Exp. Med. 213, 2635–2654. doi:10.1084/jem.20160833

Guo, T., Noble, W., Hanger, D.P., 2017. Roles of tau protein in health and disease. Acta Neuropathol. 133, 665–704. doi:10.1007/s00401-017-1707-9

Haase, C., Stieler, J.T., Arendt, T., Holzer, M., 2004. Pseudophosphorylation of tau protein alters its ability for self-aggregation. J. Neurochem. 88, 1509–1520. doi:10.1046/j.1471-4159.2003.02287.x

Halpain, S., Dehmelt, L., 2006. The MAP1 family of microtubule-associated proteins. Genome Biol. 7, 224. doi:10.1186/gb-2006-7-6-224

Hanger, D.P., Anderton, B.H., Noble, W., 2009. Tau phosphorylation: the therapeutic challenge for neurodegenerative disease. Trends Mol. Med. 15, 112–119. doi:10.1016/j.molmed.2009.01.003

Harada, A., Oguchi, K., Okabe, S., Kuno, J., Terada, S., Ohshima, T., Sato-Yoshitake, R., Takei, Y., Noda, T., Hirokawa, N., 1994. Altered microtubule organization in small-calibre axons of mice lacking tau protein. Nature 369, 488–491. doi:10.1038/369488a0

Harris, J.A., Koyama, A., Maeda, S., Ho, K., Devidze, N., Dubal, D.B., Yu, G.Q., Masliah, E., Mucke, L., 2012. Human P301L-Mutant Tau Expression in Mouse Entorhinal-Hippocampal Network Causes Tau Aggregation and Presynaptic Pathology but No Cognitive Deficits. PLoS One 7. doi:10.1371/journal.pone.0045881

Husson, S.J., 2012. Keeping track of worm trackers. WormBook 1–17. doi:10.1895/wormbook.1.156.1

Iba, M., Guo, J.L., McBride, J.D., Zhang, B., Trojanowski, J.Q., Lee, V.M.-Y., 2013. Synthetic Tau Fibrils Mediate Transmission of Neurofibrillary Tangles in a Transgenic Mouse Model of Alzheimer's-Like Tauopathy. J. Neurosci. 33, 1024–1037. doi:10.1523/JNEUROSCI.2642-12.2013

Ishihara, T., Hong, M., Zhang, B., Nakagawa, Y., Lee, M.K., Trojanowski, J.Q., Lee, V.M., 1999. Age-dependent emergence and progression of a tauopathy in transgenic mice overexpressing the shortest human tau isoform. Neuron 24, 751–62.

Jeganathan, S., von Bergen, M., Brutlach, H., Steinhoff, H.-J., Mandelkow, E., 2006. Global Hairpin Folding of Tau in Solution. Biochemistry 45, 2283–2293. doi:10.1021/bi0521543

Jicha, G.A., Bowser, R., Kazam, I.G., Davies, P., 1997. Alz-50 and MC-1, a new monoclonal antibody raised to paired helical filaments, recognize conformational epitopes on recombinant tau. J. Neurosci. Res. 48, 128–132.

Kampers, T., Pangalos, M., Geerts, H., Wiech, H., Mandelkow, E., 1999. Assembly of paired helical filaments from mouse tau : implications for the neurofibrillary pathology in transgenic mouse models for Alzheimer's disease 451.

Kaufman, S.K., Sanders, D.W., Thomas, T.L., Ruchinskas, A.J., Vaquer-Alicea, J., Sharma, A.M., Miller, T.M., Diamond, M.I., 2016. Tau Prion Strains Dictate Patterns of Cell Pathology, Progression Rate, and Regional Vulnerability In Vivo. Neuron 92, 796–812. doi:10.1016/j.neuron.2016.09.055

Kawas, C., Gray, S., Brookmeyer, R., Fozard, J., Zonderman, A., 2000. Age-specific incidence rates of Alzheimer's disease: The Baltimore Longitudinal Study of Aging. Am. Acad. Neurol. 54, 2072–2077. doi:10.1212/WNL.54.11.2072

Keith, S.A., Amrit, F.R.G., Ratnappan, R., Ghazi, A., 2014. The C. elegans healthspan and stress-resistance assay toolkit. Methods 68, 476–486. doi:10.1016/j.ymeth.2014.04.003

Kidd, M., 1963. Paired helical filaments in electron microscopy of Alzheimer's disease. Nature 197, 192–193. doi:10.1038/197192b0

Klunk, W.E., Engler, H., Nordberg, A., Wang, Y., Blomqvist, G., Holt, D.P., Bergström, M., Savitcheva, I., Huang, G.F., Estrada, S., Ausén, B., Debnath, M.L., Barletta, J., Price, J.C., Sandell, J., Lopresti, B.J., Wall, A., Koivisto, P., Antoni, G., Mathis, C.A., Långström, B., 2004. Imaging Brain Amyloid in Alzheimer's Disease with Pittsburgh Compound-B. Ann. Neurol. 55, 306–319. doi:10.1002/ana.20009

Kosik, K.S., Orecchio, L.D., Bakalis, S., Neve, R.L., 1989. Developmentally regulated expression of specific tau sequences. Neuron 2, 1389–97.

Kraemer, B.C., Zhang, B., Leverenz, J.B., Thomas, J.H., Trojanowski, J.Q., Schellenberg, G.D., 2003. Neurodegeneration and defective neurotransmission in a Caenorhabditis elegans model of tauopathy. Proc. Natl. Acad. Sci. U. S. A. 100, 9980–5. doi:10.1073/pnas.1533448100

Kril, J.J., Patel, S., Harding, A.J., Halliday, G.M., 2002. Neuron loss from the hippocampus of Alzheimer's disease exceeds extracellular neurofibrillary tangle formation. Acta Neuropathol. 103, 370–376. doi:10.1007/s00401-001-0477-5

Kuchibhotla, K. V, Wegmann, S., Kopeikina, K.J., Hawkes, J., Rudinskiy, N., Andermann, M.L., Spires-Jones, T.L., Bacskai, B.J., Hyman, B.T., 2014. Neurofibrillary tangle-bearing neurons are functionally integrated in cortical circuits in vivo. Proc. Natl. Acad. Sci. U. S. A. 111, 510–4. doi:10.1073/pnas.1318807111

Lasagna-Reeves, C.A., Castillo-Carranza, D.L., Sengupta, U., Guerrero-Munoz, M.J., Kiritoshi, T., Neugebauer, V., Jackson, G.R., Kayed, R., 2012. Alzheimer brain-derived tau oligomers propagate pathology from endogenous tau. Sci. Rep. 2, 700. doi:10.1038/srep00700

Litersky, J.M., Johnson, G. V, Jakes, R., Goedert, M., Lee, M., Seubert, P., 1996. Tau protein is phosphorylated by cyclic AMP-dependent protein kinase and calcium/calmodulin-dependent protein kinase II within its microtubule-binding domains at Ser-262 and Ser-356. Biochem. J. 316 (Pt 2, 655–60. doi:10.1042/bj3160655

Liu, F., Grundke-Iqbal, I., Iqbal, K., Gong, C.X., 2005. Contributions of protein phosphatases PP1, PP2A, PP2B and PP5 to the regulation of tau phosphorylation. Eur. J. Neurosci. 22, 1942–1950. doi:10.1111/j.1460-9568.2005.04391.x

Liu, L., Drouet, V., Wu, J.W., Witter, M.P., Small, S.A., Clelland, C., Duff, K., 2012. Trans-synaptic spread of tau pathology in vivo. PLoS One 7, 1–9. doi:10.1371/journal.pone.0031302

Mandelkow, E., Mandelkow, E.M., 1995. Microtubules and microtubule-associated proteins. Curr. Opin. Cell Biol. 7, 72–81. doi:10.1016/0955-0674(95)80047-6

Martin, L., Latypova, X., Terro, F., 2011. Post-translational modifications of tau protein: Implications for Alzheimer's disease. Neurochem. Int. 58, 458–471. doi:10.1016/j.neuint.2010.12.023

Matsuo, E.S., Shin, R.W., Billingsley, M.L., Van deVoorde, A., O'Connor, M., Trojanowski, J.Q., Lee, V.M.Y., 1994. Biopsy-derived adult human brain tau is phosphorylated at many of the same sites as Alzheimer's disease paired helical filament tau. Neuron 13, 989–1002. doi:10.1016/0896-6273(94)90264-X

Mello, C.C., Kramer, J.M., Stinchcomb, D., Ambros, V., 1991. Efficient gene transfer in C.elegans: extrachromosomal maintenance and integration of transforming sequences. EMBO J. 10, 3959–70. doi:10.1016/0168-9525(92)90342-2

Min, S.-W., Cho, S.-H., Zhou, Y., Schroeder, S., Haroutunian, V., Seeley, W.W., Huang, E.J., Shen, Y., Masliah, E., Mukherjee, C., Meyers, D., Cole, P. a, Ott, M., Gan, L., 2010. Acetylation of tau inhibits its degradation and contributes to tauopathy. Neuron 67, 953–66. doi:10.1016/j.neuron.2010.08.044

Miyasaka, T., Ding, Z., Gengyo-Ando, K., Oue, M., Yamaguchi, H., Mitani, S., Ihara, Y., 2005. Progressive neurodegeneration in C. elegans model of tauopathy. Neurobiol. Dis. 20, 372–383. doi:10.1016/j.nbd.2005.03.017

Miyasaka, T., Xie, C., Yoshimura, S., Shinzaki, Y., Yoshina, S., Kage-Nakadai, E., Mitani, S., Ihara, Y., 2016. Curcumin improves tau-induced neuronal dysfunction of nematodes. Neurobiol. Aging 39, 69–81. doi:10.1016/j.neurobiolaging.2015.11.004

Morris, J.C., Roe, C.M., Grant, E.A., Head, D., Storandt, M., Goate, A.M., Fagan, A.M., Holtzman, D.M., Mintun, M.A., 2009. Pittsburgh Compound B Imaging and Prediction of Progression From Cognitive Normality to Symptomatic Alzheimer Disease. Arch. Neurol. 66, 1469–1475. doi:10.1001/archneurol.2009.269

Morsch, R., Simon, W., Coleman, P.D., 1999. Neurons may live for decades with neurofibrillary tangles. J. Neuropathol. Exp. Neurol. 58, 188–97.

Musiek, E.S., Holtzman, D.M., 2015. Three dimensions of the amyloid hypothesis: time, space and “wingmen.” Nat. Neurosci. 18, 800–806. doi:10.1038/nn.4018

Neve, R.L., Harris, P., Kosik, K.S., Kurnit, D.M., Donlon, T.A., 1986. Identification of cDNA clones for the human microtubule-associated protein tau and chromosomal localization of the genes for tau and microtubule-associated protein 2. Brain Res. 387, 271–80.

Otvos, L., Feiner, L., Lang, E., Szendrei, G.I., Goedert, M., Lee, V.M., 1994. Monoclonal antibody PHF-1 recognizes tau protein phosphorylated at serine residues 396 and 404. J. Neurosci. Res. 39, 669–673. doi:10.1002/jnr.490390607

Peeraer, E., Bottelbergs, A., Van Kolen, K., Stancu, I.-C., Vasconcelos, B., Mahieu, M., Duytschaever, H., Ver Donck, L., Torremans, A., Sluydts, E., Van Acker, N., Kemp, J.A., Mercken, M., Brunden, K.R., Trojanowski, J.Q., Dewachter, I., Lee, V.M.Y., Moechars, D., 2015. Intracerebral injection of preformed synthetic tau fibrils initiates widespread tauopathy and neuronal loss in the brains of tau transgenic mice. Neurobiol. Dis. 73, 83–95. doi:10.1016/j.nbd.2014.08.032

Pir, G.J., Choudhary, B., Mandelkow, E., Mandelkow, E.-M., 2016. Tau mutant A152T, a risk factor for FTD/PSP, induces neuronal dysfunction and reduced lifespan independently of aggregation in a C. elegans Tauopathy model. Mol. Neurodegener. 11, 33. doi:10.1186/s13024-016-0096-1

Prusiner, S.B., 1984. Some Speculations about Prions, Amyloid, and Alzheimer’s Disease. N. Engl. J. Med. 310, 661–663. doi:10.1056/NEJM198403083101021

Rademakers, R., Cruts, M., van Broeckhoven, C., 2004. The role of tau (MAPT) in frontotemporal dementia and related tauopathies. Hum. Mutat. 24, 277–95. doi:10.1002/humu.20086

Restif, C., Metaxas, D., 2008. Tracking the swimming motions of C. elegans worms with applications in aging studies. Med. Image Comput. Comput. Assist. Interv. 11, 35–42.

Sanders, D.W., Kaufman, S.K., DeVos, S.L., Sharma, A.M., Mirbaha, H., Li, A., Barker, S.J., Foley, A.C., Thorpe, J.R., Serpell, L.C., Miller, T.M., Grinberg, L.T., Seeley, W.W., Diamond, M.I., 2014. Distinct Tau Prion Strains Propagate in Cells and Mice and Define Different Tauopathies. Neuron 1–18. doi:10.1016/j.neuron.2014.04.047

Schneider, A., Biernat, J., Bergen, M. Von, Mandelkow, E., Mandelkow, E.M., 1999. Phosphorylation that detaches tau from microtubules S262 and S214 protects it against aggregation into Alzheimer paired helical filaments. J. Neurochem. 73, S26–S26.

Schoenfeld, T.A., Obart, R.A., 1994. Diverse Distribution and Function of Fibrous Microtubule-Associated Proteins in the Nervous System. Int. Rev. Cytol. 151.

Seubert, P., Mawal-Dewan, M., Barbour, R., Jakes, R., Goedert, M., Johnson, G.V.W., Litersky, J.M., Schenk, D., Lieberburg, I., Trojanowski, J.Q., Lee, V.M.Y., 1995. Detection of phosphorylated Ser262 in fetal tau, adult tau, and paired helical filament tau. J. Biol. Chem. doi:10.1074/jbc.270.32.18917

Sergeant, N., Bretteville, A., Hamdane, M., Caillet-Boudin, M.-L., Grognet, P., Bombois, S., Blum, D., Delacourte, A., Pasquier, F., Vanmechelen, E., Schraen-Maschke, S., Buée, L., 2008. Biochemistry of Tau in Alzheimer's disease and related neurological disorders. Expert Rev. Proteomics 5, 207–224. doi:10.1586/14789450.5.2.207

Shin, R.W., Iwaki, T., Kitamoto, T., Tateishi, J., 1991. Hydrated autoclave pretreatment enhances tau immunoreactivity in formalin-fixed normal and Alzheimer's disease brain tissues. Lab. Invest. 64, 693–702.

Simonetta, S.H., Golombek, D.A., 2007. An automated tracking system for Caenorhabditis elegans locomotor behavior and circadian studies application. J. Neurosci. Methods 161, 273–280. doi:10.1016/j.jneumeth.2006.11.015

Smith, M.A., Taneda, S., Richey, P.L., Miyata, S., Yant, S.-D., Sternt, D., Sayre, L.M., Monnier, V.M., Perry, G., 1994. Advanced Maillard reaction end products are associated with Alzheimer disease pathology. Neurobiology 91, 5710–5714. doi:10.1073/pnas.92.5.1794e

Swierczek, N.A., Giles, A.C., Rankin, C.H., Kerr, R.A., 2011. High-throughput behavioral analysis in C. elegans. Nat. Methods 8, 592–598.

Tien, N.-W., Wu, G.-H., Hsu, C.-C., Chang, C.-Y., Wagner, O.I., 2011. Tau/PTL-1 associates with kinesin-3 KIF1A/UNC-104 and affects the motor's motility characteristics in C. elegans neurons. Neurobiol. Dis. 43, 495–506. doi:10.1016/j.nbd.2011.04.023

Trojanowski, J.Q., Schuck, T., Schmidt, M.L., Lee, V.M., 1989. Distribution of tau proteins in the normal human central and peripheral nervous system. J. Histochem. Cytochem. 37, 209–15.

Tsechpenakis, G., Bianchi, L., Metaxas, D., Driscoll, M., 2008. A novel computational approach for simultaneous tracking and feature extraction of C. elegans populations in fluid environments. IEEE Trans. Biomed. Eng. 55, 1539–49. doi:10.1109/TBME.2008.918582

Uchihara, T., 2007. Silver diagnosis in neuropathology: principles, practice and revised interpretation. Acta Neuropathol. 113, 483–99. doi:10.1007/s00401-007-0200-2

Van Cauwenberghe, C., Van Broeckhoven, C., Sleegers, K., 2016. The genetic landscape of Alzheimer disease: clinical implications and perspectives. Genet. Med. 18, 421–430. doi:10.1038/gim.2015.117

Wang, Y., Mandelkow, E., 2015. Tau in physiology and pathology. Nat. Rev. Neurosci. 17, 22–35. doi:10.1038/nrn.2015.1

White, J.G., Southgate, E., Thomson, J.N., Brenner, S., 1986. The structure of the nervous system of the nematode Caenorhabditis elegans. Philos. Trans. R. Soc. Lond. B. Biol. Sci. 314, 1–340.

Williams, D.R., 2006. Tauopathies: Classification and clinical update on neurodegenerative diseases associated with microtubule-associated protein tau. Intern. Med. J. 36, 652–660. doi:10.1111/j.1445-5994.2006.01153.x

Xie, C., Miyasaka, T., Yoshimura, S., Hatsuta, H., Yoshina, S., Kage-Nakadai, E., Mitani, S., Murayama, S., Ihara, Y., 2014. The homologous carboxyl-terminal domains of microtubule-associated protein 2 and Tau induce neuronal dysfunction and have differential fates in the evolution of neurofibrillary tangles. PLoS One 9. doi:10.1371/journal.pone.0089796

Zheng-Fischhöfer, Q. (1998). Sequential phosphorylation of Tau by glycogen synthase kinase-3β and protein kinase A at Thr212 and Ser214 generates the Alzheimer-specific epitope of antibody. *European Journal of Biochemistry*, *552*, 542–552. Retrieved from http://onlinelibrary.wiley.com/doi/10.1046/j.1432-1327.1998.2520542.x/full

2 Material and Methods

2.1 Plasmid Construction and Generation of Transgenic Worm Lines

Constructs were created by fusion PCR (Hobert, 2002), all primers (Microsynth AG, Balgach, Switzerland) and primer pairs used are listed in Table 22 and Table 23. Genomic *C. elegans* DNA was extracted by single worm lysis using proteinase K digestion as described in (Ahringer, 2006). Genomic DNA from N2 was used as template to amplify 1.3 kb upstream of *aex-3*, 0.7 kb upstream of *mec-7* and 2.2 kb downstream of *unc-86*. Genomic DNA from OH4134 was used to amplify *gfp* and *dsRed2*. cDNA of wild type hTau (isoform 1N4R) was amplified from pRK172 1N4R plasmid (generous gift from M. Goedert, MRC Cambridge, UK). Tau harbouring the V337M mutation was generated from the same plasmid using two sets of primers containing the mutated sequence. All fragments were amplified using a taq polymerase (PCR Extender System, 5 Prime GmbH, Hilden, Germany) according to the manufacturer's protocol. After each amplification, PCR fragments were separated on an 0.8 % (w/v) agarose gel, corresponding band excised and extracted (QIAquick Gel Extraction Kit, QIAGEN Inc., CA, USA). Once the individual fragments were combined into full transgenes, the PCR products were ligated into the pCR 2.1-TOPO TA vector (TOPO® TA Cloning® Kit, Thermo Fisher Scientific Schweiz AG, Reinach, Switzerland) and plasmids transformed into chemically competent *E. coli* (One Shot® Mach1™-T1, Thermo Fisher Scientific Schweiz AG, Reinach, Switzerland).

aex-3p::hTau(1N4R, V337)::unc-86UTR and *aex-3p::hTau(1N4R, P301S)::unc-86UTR* were created by mutation PCR from *aex-3p::hTau(1N4R, wt)::unc-86UTR* by site-directed mutagenesis following the Stratagene's Quick-Change™ protocol (http://sevierlab.vet.cornell.edu/resources/Stratagene-QuikchangeManual.pdf) using a Phusion DNA polymerase (Phusion High-Fidelity PCR Kit, Thermo Fisher Scientific Schweiz AG, Reinach, Switzerland) and *Dpn I* (Thermo Fisher Scientific Schweiz AG, Reinach, Switzerland). Plasmids were transformed in chemically competetent *E. coli* Dh5α (generous gift from Johannes Thoma, D-BSSE ETH Zürich, Switzerland).

Transformed *E. coli* were plated onto LB agar plates containing 50 µg/ml (w/v) ampicillin, as well as IPTG and X-Gal and grown at 37 °C overnight. The next day, 10-15 white colonies were picked from each transformed construct and PCR reactions were performed to check for the presence of the desired construct. Several clones were selected, grown in 10 ml LB, plasmids extracted using alkaline lysis as described here: https://msu.edu/course/css/451/LabProtocols/Plasmid%20Isolation%20Using%20Alkaline%20Lysis%20%28Exp%203,%20CSS451%29.pdf. All plasmids were sanger sequenced and checked for unintended alterations before they were injected.

Plasmids were co-injected into N2 young adults as described in (Evans, 2006) in the following combinations *mec-7p::hTau(1N4R, V337)::unc-86UTR + mec-7p::dsRed2::unc-86UTR* and *aex-3p::hTau(1N4R, wt)::unc-86UTR + aex-3p::gfp::unc-86UTR* at concentrations of 80-100 ng/µl in dH_2O each. DsRed2/GFP served as injection marker and

positive F1 were isolated, cultivated and kept once transmission of injection marker to F2 was observed. Non-integrated transgenic lines were synchronized by hypochlorite treatment as described in section “Paraffin Embedding and Histology” and then subjected to 40 Gy irradiation from a Cs 137 gamma ray source (IBL 437C, Cisbio Bioassays, Codolet, France) once the majority has reached the L4 stage. 5 irradiated L4 were picked on each of 20 100 mm NGM plates seeded with OP50 and grown at 20 °C for 14 days. A small chunk of each plate was then transferred to a 60 mm seeded NGM plate and grown another 5 days. 20 worms of each of the 20 60 mm plates were then picked and put on individual 35 mm seeded NGM plates resulting in 400 individual worms. After 1 week, the plates were screened for fluorescent protein expression, in case of 100 % penetrance in progeny, the transgene has integrated into the genome. Stable lines were crossed 5 x with N2 males.

Outcrossed lines were then crossed with SS104 males at 15 °C. Heterozygous F1 hermaphrodites were singled, and homozygous F2 were then singles once again. After singled F2 started to lay eggs, the plate was cut in two parts and one part was shifted to 25 °C while the remaining part was kept at 15 °C. In case of 100 % sterile F3 on the plates at 25 °C, the cross was complete and the line was continued from the corresponding plate kept at 15 °C.

2.2 Worm Line Maintenance and Preparation for RAPID Assay

2.2.1 Worm Line Maintenance

The following worm strains were provided by the Caenorhabditis Genetics Center (CGC, funded by NIH Office of Research Infrastructure Programs P40 OD010440):
N2, OH4134, SS104, and the *E. coli* strain OP50.

Worms were cultivated as described in (Stiernagle, 2006) with the following exceptions: M9 buffer was prepared using 2 g instead of 6 g Na_2HPO_4 and worms were frozen in M9 containing 15 % (v/v) of 87 % glycerol which was sterilized by autoclaving.

Worms were grown on 35 mm NGM agar plates filled with 3.5 ml NGM agar without additives and seeded the next day with 150 µl overnight culture of OP50 grown in LB without antibiotics. Furthermore, OP50 cultures were grown in 1 L LB overnight at room temperature by adding 200 µl starter culture from an overnight culture grown in LB containing 50 µg/ml ampicillin. OP50 were then pelleted by centrifugation at 2’500 rcf for 30 min and kept at -20 °C until use. To add additional OP50 to worm cultures, pellets were thawed, resuspended in equal amounts M9 and distributed in drops of 200 µl onto the plates. All chemicals were obtained from Sigma-Aldrich (Sigma-Aldrich Chemie GmbH Buchs, Switzerland).

Lines harbouring the *glp-4(bn2)* allele were kept in temperature controlled incubators at 15 °C for cultivation or at room temperature to induce sterility. Other lines were grown at 20 °C in temperature controlled incubators.

2.2.2 Preparation of Worms for RAPID Assay

Before an assay was run, worm strains were grown as described above at 15 °C on 35 mm NGM plates seeded with OP50. To synchronize worms, 10 - 15 gravid hermaphrodites were

picked on seeded NGM plates and allowed to lay eggs for 4 - 8 h at RT, after which the adults were removed. The next day, hatched larvae (L1/L2) were singled on individual 35 mm NGM agar plates, seeded with 15 µL overnight culture of OP50 seeded the day before. Then the plates were labelled, sealed and put on the RAPID assay as described in Worm strain maintenance and preparation for RAPID assay. The time of the egg lay plus half the time of the egg lay duration was defined as date of birth for a given strain. Usually, four strains were prepared in parallel with 70 worms per strain and a total of 280 worms per run.

2.3 Paraffin Embedding and Histology

2.3.1 Generation of Worm Blocks

A large number of synchronized worms was obtained by hypochlorite treatment, modified from http://groups.molbiosci.northwestern.edu/morimoto/research/Protocols/IX.%20C.%20elegans/A.%20General/3.%20Bleaching%20Protocol.pdf.

A starter culture of worms were washed off of a single plate with ~0.5 ml M9 using a plastic pasteur pipette and distributed on 14 35 mm NGM plates seeded with OP50. The worms were grown either at 20 °C or in case of *glp-4(bn2)* carrying strains at 15 °C. If the bacteria were depleted before the majority of worms contained eggs, concentrated OP50 was added. Once the majority of worms developed into gravid hermaphrodites, worms were collected in a 15 ml conical tube by washing off the plates with M9.

Worms were pelleted for 5 min at 1.5 rcf and supernatant discarded. The pellet was resuspended in 7.5 ml of hypochlorite solution (8.25 ml dH_2O, 3.75 ml 1M NaOH, 3 ml sodium hypochlorite 6-14 % active chlorine, Sigma-Aldrich Chemie GmbH Buchs, Switzerland) through vortexing. As soon as most of the worms dissolved or cracked open, the suspension was gravity filtered through a 100 µm mesh (CELLSTAR EASYstrainer, Greiner Bio-One GmbH, Frickenhausen, Germany) into a 50 ml conical tube filled with 35 ml M9. The tube was topped up with M9 and spun down 5 min at 1.5 rcf. The pellet was then resuspended in M9 and transferred to a 15 ml conical tube and spun down 5 min at 1.5 rcf, this step was repeated 2 more times. The embryos were incubated for 24 h on a rotating wheel in the dark at room temperature. Afterwards, the hatched worms were centrifuged 5 min at 1.5 rcf and supernatant was removed leaving 0.5 ml M9 and the worms in the tube. The worms were resuspended in the remaining liquid and evenly dispensed on 21 35mm OP50 seeded NGM plates. 72 h after transfer, the worms were collected in a 15 ml conical tube in M9 and pelleted 5 min at 1.5 rcf. The pellet was resuspended in 10 ml 10 % (v/v) histological grade formaldehyde in phosphate buffer pH 7.4 (Spitalpharmazie, University Hospital Basel), transferred to 15 ml glass centrifuge tubes and fixed for 1h at 60 °C. The fixed worms were spun down 3 min at 3 rcf and resuspended in M9, 3 times to wash off any formaldehyde. If the pellet was larger than 300 µl in volume, the pellet was resuspended and half of it was put in a second tube, then spun down 3 min at 3 rcf. 200 µl of human blood plasma (donor plasma after expiration date from the Blutspendezentrum Basel, also available from Sigma-Aldrich Chemie GmbH Buchs, Switzerland). 50 µm of thrombin from bovine plasma (T4648, Sigma-Aldrich Chemie GmbH Buchs, Switzerland) was added using a cut off pipette tip to decrease shearing and well mixed by pipetting up and down. After 30 s, when the coagulation was complete, 10 ml of 10 % (v/v) histological grade formaldehyde in phosphate buffer pH 7.4 (Spitalpharmazie, University Hospital Basel) was added and

incubated for 1h at 60 °C. Fixed thrombi were then placed in histology cassettes (Tissue-Loc™ HistoScreen™ Cassettes, Thermo Fisher Scientific Schweiz AG, Reinach, Switzerland), dehydrated in an ascending series of EtOH/water solutions, followed by xylene and paraffin (Surgipath Paraplast®, Leica Biosystems Nussloch GmbH, Nussloch, Germany) embedded in an automated tissue processor (TPC 15 Duo, Medite Service AG, Dietikon, Switzerland) according to surgical pathology procedures. Finally, the worm block was taken from the molten paraffin, transferred to an embedding mold and embedded in paraffin. 4 µm sections of these worm blocks were cut using a microtome (Leica SM2000R, Leica Biosystems Nussloch GmbH, Nussloch, Germany), stretched on a hot water bath (Tissue Flotation Bath TFB 45, Medite Service AG, Dietikon, Switzerland) mounted on positively charged microscopy glass slides (SuperFrost® Plus, Thermo Fisher Scientific Schweiz AG, Reinach, Switzerland) and dried overnight at 37 °C and stored for later use in immunohistochemistry.

2.3.2 Hematoxylin and Eosin Staining

Paraffin sections were deparaffinized in xylene and rehydrated through a series of EtOH/water solutions from 100 %, 96 %, 80 %, and 70 % (v/v), followed by dH_2O, submerging the sections for 5 min each step. Rehydrated sections are stained with Harris' hematoxylin (J.T. Baker, Biosystems Switzerland AG, Muttenz, Switzerland), for 5 min, washed twice in dH_2O and differentiated in 0.2 % HCl in (v/v) diluted in 70 % ethanol (v/v). Sections are stained in 1 % (w/v) Erythrosin B (RAL DIAGNOSTICS, Biosystems Switzerland AG, Muttenz, Switzerland), a stain closely resembling eosin Y, washed in dH_2O and dehydrated through an ascending series of EtOH water solutions, form 70 %, 80 %, 100 % (v/v), followed by xylene. Sections are mounted using Pertex (Histolab Products AB, Biosystems Switzerland AG, Muttenz, Switzerland).

2.3.3 Gallyas Silver Impregnation

Sections are deparaffinized and rehydrated as described above. Sections are incubated in 3 % periodic acid (w/v) for 30 min, rinsed in dH_2O, followed by alkaline silver solution (1 M NaOH, 0.6 M KI, 2 mM $AgNO_3$) for 10 min. Sections are developed by mixing developer solution 1 (0.5 M Na_2CO_3), solution 2 (24 mM NH_4NO_3, 12 mM $AgNO_3$, 3.5 mM $H_4[Si(W_3O_{10})_4]$), and solution 3 (24 mM NH_4NO_3, 12 mM $AgNO_3$, 3.5 mM $H_4[Si(W_3O_{10})_4]$, 3 % formaldehyde) in a ratio of 30:9:21 immediately before use, for 5-10 min (depending on desired staining intensity). Developing is stopped using 0.5 % acetic acid (v/v) for 30 min and fixed using 5 % $Na_2S_2O_3$ (w/v) for 3 min. The sections are rinsed in dH_2O, counterstained using hematoxylin, differentiated, dehydrated, and embedded as described above. The Gallyas silver impregnation was automated using a modified rotary autostainer (Shandon Varistain 24-3, discontinued) equipped with three bottles and three pumps to mix the developer solutions right before use, see Figure 2.

Figure 2: Modified Autostainer for Gallyas Silver Impregnation

Modified autostainer used to perform Gallyas silver impregnation for optimal reproducibility. A basket holding the slides is attached to the lid, which can be raised and rotated to transfer the slides from one container to the next. The developer solutions are stored separately and pumped in one of the containers to mix them right before immersion of the slides (bottles on the left).

2.3.4 Immunohistochemistry

All immunohistochemical labellings were performed using an automated IHC slide staining system (Ventana, BenchMark XT, Ventana Medical Systems, USA) using the manufacturer's protocol and reagents. Antibodies, dilutions and pretreatments used are listed in Table 3.

Antibody	Clone	Source	Retrieval	Dilution
HT7	MN1000	Invitrogen	CC1 24	1:500
AT8	MN1020	Invitrogen	CC1 24	1:4'000
AT100	MN1060	Invitrogen	CC1 24	1:800
anti-GFP	ab290 (polyclonal)	Abcam	CC1 24	1:16'000

Table 3: Antibodies and Protocols

Antibodies and dilutions used throughout this work. Heat-mediated antigen retrieval was performed according to the manufacturer’s protocol for 24 min using “Cell Conditioning 1” solution (Ventana, Ventana Medical Systems, USA).

All labellings were carried out in duplicate, each time using appropriate positive and negative controls. IHC labelling were assessed by two researchers in a blinded fashion to genotype and strain. Tau expression was compared to the positive control which served as a reference for labelling intensities. Images were recorded using a digital camera mounted to an upright microscope (Olympus DP73 + Olympus BX43, Olympus Schweiz AG, Volketswil, Switzerland) using fixed exposure and fixed illumination settings for images that are shown in the same panel.

2.3.5 Resin Embedding

1 mm^3 cubes of tissue or a pellet of worms were fixed in 3 % glutaraldehyde in PBS (v/v) for 2 h at 4 °C, rinsed two time in PBS and postfixed in 1 % OsO_4 in PBS (w/v) for 2 h at 4 °C. OsO_4 was removed and the tissue was dehydrated in an ascending series of EtOH of 70 %, 80 %, 96 % and 100 % for two times 15 min each and finally 100 % acetone two times for 30 min. The acetone was removed and the tissue was incubated in a 1:1 mix of acetone and Durcupan™ (44610-1EA, Sigma-Aldrich Chemie GmbH Buchs, Switzerland) for 3 h followed by a 1:3 mix of acetone and Durcupan™ overnight. The next day, the tissue was embedded in Durcupan™ and cured at 60 °C for two days. The blocks were trimmed to size and sectioned on an ultramicrotome (Reichert Ultracut S, Leica Wien, Austria) using a glass knife for sections between 0.5 - 1 µm or using a diamond knife for ultrathin sections between 100 - 200 nm. Ultrathin sections were negatively stained in 4 % uranyl acetate (w/v) in 50 % EtOH (v/v). The resin of semithin sections can be removed by immersion of sections in a saturated solution of KOH in EtOH for 15 min washed in absolute EtOH, hydrated in a descending series of EtOH and processed the same way as paraffin sections.

2.3.6 Statistical Evaluation of RAPID Data

RAPID data was evaluated as described in Modelling and statistical tests including model selection. Data from 8 runs were combined and compared against the reference (SS104 pooled from run 2 and 9). The follwing formulae were used in R to fit the models with the *lme* function of the *nlme* package:

```
model1 <- lme(afterArea ~ days*genotype + I(days^2) + temperatureTable,
random=~days|setID/groupID/sampleID, data = trackDataCollector_day3,
corCAR1(form = ~days|setID/groupID/sampleID), method = "REML", na.action =
na.omit)

model2 <- lme(afterArea ~ days*HT7 + I(days^2) + genotype + temperatureTable,
random=~days|setID/groupID/sampleID, data = trackDataCollector_day3,
correlation = corCAR1(form = ~days|setID/groupID/sampleID), method = "REML",
na.action = na.omit)
```

The structure of the R data frame `trackDataCollector_day3` is shown in Table 25.

2.4 References

Ahringer, J., 2006. Reverse genetics. WormBook. doi:10.1895/wormbook.1.47.1

Evans, T., 2006. Transformation and microinjection. WormBook. doi:10.1895/wormbook.1.108.1

Hobert, O., 2002. PCR Fusion-Based Approach to Create Reporter Gene Constructs for Expression Analysis in Transgenic C. elegans. Biotechniques 32, 728–730.

Stiernagle, T., 2006. Maintenance of C. elegans. WormBook. doi:10.1895/wormbook.1.101.1

3 Results

As discussed in section “C. elegans Models of Tauopathies“, the phenotypes of hTau expression in *C. elegans* neurons were often qualitatively described as uncoordinated locomotion and only a small number of animals were assessed by conducting thrashing assays. To study the progression rate of a phenotype, longitudinal measurements would be preferable over cross-sectional measurements. Since existing worm-tracking solutions do not pair high throughput with longitudinal data acquisition, we developed the Robot-Assisted Plate Imaging Device (RAPID). As a proof of principle experiment for the capabilities of RAPID, we assessed the stimulated locomotor performance of 10 different *C. elegans* strains, some of which were reported to have locomotor phenotypes. Since RAPID is not limited to the study of neurodegeneration, we evaluated our novel method with focus on quantitative and qualitative assessment of physiological and pathological ageing, a topic of particular impact when studying effects of life-prolonging interventions in *C. elegans*. The results from this set of experiments and a detailed description of the hard- and software components of RAPID were compiled in a manuscript which was submitted to *Neurobiology of Aging* on 17.07.2017 and a request for revisions was received on 21.10.2017. Hence, the manuscript is included in this work in its originally submitted form and the major points to be revised are discussed in section “Reviewer Comments on RAPID Manuscript“.

3.1 Manuscript: RAPID - High-throughput standardized health modelling in *C. elegans*

3.1.1 Authors and affiliations

Jürgen Hench [*1], Gabriel Schweighauser [*1], Ivana Bratic Hench [1], Roberta Diehl-Rodriguez [1,2], Stephan Frank [1], and Markus Tolnay [1]

*) equal contribution

1) Institute of Medical Genetics and Pathology, University of Basel, Basel University Hospital, Division of Neuropathology, Schoenbeinstrasse 40, CH-4031 Basel, Switzerland

2) Behavioral and Cognitive Neurology Unit, Department of Neurology, and LIM-22, University of São Paulo, São Paulo, Brazil

3.1.2 Keywords

worm tracker, longitudinal examination, lifespan, healthspan, gerospan, physiological ageing

3.1.3 Abstract

As one of the most widely used animal models of ageing, the nematode *C. elegans* is increasingly employed to differentiate “healthy ageing” from chronological lifespan extension. However, most worm tracker-based ageing assays are unsuited to assess health. Here, we report on the development of RAPID, an automated high-throughput platform for lifelong individual worm recordings, which allows to assay responses to standardized, non-destructive vibratory stimuli as health readout. Significantly, a comparative analysis of wild type and nine genetically modified *C. elegans* strains revealed superior overall health of wild type worms, even when compared to long-lived strains. Thus, implying that lifespan extension may not be of advantage when occurring at the expense of decreased overall health, our observation is highly relevant to animal model-based gerontology research.

3.1.4 Introduction

C. elegans lifespan has long been known to be influenced by environmental factors such as temperature and food availability (Klass, 1977). In addition, single gene mutations in *age-1* (Friedman and Johnson, 1988) and *daf-2* (Kenyon et al., 1993) drastically extend lifespan under laboratory conditions. With the realisation that lifespan can be actively modulated, *C. elegans* has become an important model system to dissect the genetics of longevity (Kenyon, 2010). However, the parameter “lifespan” does not qualitatively describe the ageing process. In particular, in many instances, extending lifespan does not increase healthspan, i.e. the amount of time spent in good health, prior to the onset of age-associated decline in bodily functions. Therefore, increasing lifespan *per se* is not necessarily useful if ultimately intended to extend healthspan in humans. Currently, there are no widely accepted healthspan-defining parameters in model systems, as it has been difficult to identify appropriate biomarkers which could translate to humans (Tatar, 2009). Decline in human gait speed is a robust predictor of human mortality (White et al., 2012). Likewise, *C. elegans* exhibits decreased motility with age (Croll et al., 1977; Bolanowski et al., 1981) possibly due to muscle frailty (Glenn et al., 2004) and functional decline in motoneuron activity (Liu et al., 2013). Whereas early work measuring motility to predict lifespan had led to inconclusive data (Bolanowski et al., 1981; Johnson et al., 1988), later studies showed a correlation between the number of days with fast movement, pharyngeal pumping rates (Huang et al., 2004), and lifespan, as well as a correlation between the rate of motor activity decline and lifespan (Hsu et al., 2009). Furthermore, motor activity has been used to define healthspan and to compare long-lived worm mutants with wild type in a cross-sectional study (Bansal et al., 2015): of note, long-lived mutants showed an increased healthspan, but when normalized to lifespan, their healthspan was shorter than in wild type. A similar study concluded that relative healthspan, normalized to lifespan, was comparable between short-lived *daf-16* mutants, long-lived *daf-2* mutants, and wild type (Hahm et al., 2015). Moreover, within isogenic *C. elegans* cultures, there seems to be not only variability regarding the ageing process itself but also within the healthspan of individual worms, whereby long-lived individuals do not have a longer healthspan if this parameter is normalized to lifespan (Zhang et al., 2016). In addition to these fundamental physiological insights, these studies emphasize the importance of automated, longitudinal recording systems to objectively determine the intra- and inter-individual variation of the ageing process.

To overcome observer bias and to increase throughput as well as detection sensitivity, many automated systems, generically termed worm trackers, have been developed (Husson, 2012). Whereas single worm trackers record the behavior of individual animals at high resolution, multi worm trackers simultaneously assay up to 120 nematodes at lower resolutions (Swierczek et al., 2011). Some trackers are able to extract a broad range of locomotion parameters such as velocity, bending angles and frequencies, and can detect complex patterns such as movement reversals or omega turns. As individual worms are typically not labelled, multi worm trackers are not suitable for longitudinal studies. Furthermore, most trackers observe a baseline activity over several minutes under different conditions such as genetic backgrounds or compounds, which allows for detailed quantitative and qualitative descriptions of locomotion at single timepoints only. Alternatively, microfluidic devices have been employed for lifelong longitudinal studies (Hulme et al., 2011; Cornaglia et al., 2016). In such devices, where a steady liquid flow delivers food and soluble compounds, and constantly removes waste and progeny, individual animals are confined to

micro-cultivation chambers to repeatedly assess swimming capability and gross morphology. Recently, a high-density vermiculture slide has been introduced in which individual worms are confined to a small patch of bacteria and sandwiched in between a hydrogel and polydimethylsiloxane (Zhang et al., 2016). While these sophisticated microfluidic approaches are appealing, their fabrication, setup, and readout are beyond the technical (and financial) capabilities of most *C. elegans* laboratories (Ng et al., 2002; Friend and Yeo, 2010).

In contrast to the above-mentioned options, scanner-based worm trackers replace microscopic lens systems and cameras with modified consumer-grade flatbed scanners to continuously record worm motions on NGM plates (Peliti et al., 2013; Stroustrup et al., 2013). Using an array of several scanners, these setups can achieve considerable throughput and offer the potential of studying single worms on smaller plates over extended periods of time. However, temporal resolutions achieved so far were 1 image / 20s and 1 image / 2h, respectively. As scanning time increases with spatial resolution, the latter can not be arbitrarily decreased since worms that leave their initial position during imaging will not be detected (Stroustrup et al., 2013). Likewise, the fixed focal length of flatbed scanners necessitates highly uniform agar plate thickness to avoid the animals leaving the optical focal plane; in addition, there is currently no option to deliver stimuli to single plates on a flatbed scanner. Whereas, in theory, a battery of lens-based single worm trackers could be used to record longitudinal data, such a space-consuming approach would (1) still provide only low throughput, (2) be hard to calibrate given the large number of individual imaging platforms, and (3) remain costly.

To overcome these limitations in obtaining high-throughput longitudinal, lifelong recordings of individual worms under standard laboratory conditions, we have developed RAPID (Robot-Assisted Plate Imaging Device). Here we report on the capabilities of our recording system using a set of well-characterized, genetically modified *C. elegans* strains. In addition to efficiently replicating previous findings in the field, our easy-to-standardize approach demonstrates that none of the examined long-lived or hyperactive mutant *C. elegans* strains has a healthspan or motility performance superior over wild type.

3.1.5 Materials and Methods

RAPID control software and robotic setup:

All software source code, circuit schematics, and 3D printable parts developed by us are made available on github (https://github.com/gabe0815/RAPID), a copy of which is part of the supplementary material. The assay is coordinated through an ImageJ (https://imagej.nih.gov/ij/) macro, where robot and cameras are operated through a series of BASH scripts on a x86_64 machine running GNU/Linux. The macro loops through a sample lookup table in which all plates are registered with a unique sample ID and the time of birth. Each stack of four is processed top down by putting each plate on its designated imaging platform, simultaneously starting the image acquisition/assay. As soon as the recording of the first plate has finished, the robot puts the plate back on its original position thereby reversing the order of plates in the stack. Images of each recording are downloaded to individual folders along with metadata (sample ID, time of birth, time of recording, camera serial number, imaging platform and temperature) as text files. After all plates have been moved back to storage, the next stack of plates is processed. The temperatures next to the plates and next to the imaging platforms are measured every 5 min using a digital thermometer (DS18S20B, Maxim Integrated, San Jose, USA) through a microcontroller board (Atmel ATMega328p, arduino nano, www.arduino.cc). The NGM plates are stored on a table in a laser cut cardboard grid with 10 x 7 slots. Four layers of NGM plates are stacked upside down on top of each other resulting in 280 plates in total. Each position in the grid is forming a stack which is processed in parallel on 4 imaging platforms. A 6-joint robotic arm (M-430iA 2PH + R-30iA, FANUC Switzerland GmbH, Biel, Switzerland) equipped with a 10 x 15 mm silicone vacuum cup (Amico No. a12122700ux0033, purchased through www.amazon.de), a diaphragm air pump (TOPSFLO TZ712/P12-15040, TOPS INDUSTRY & TECHNOLOGY CO. LTD., China) and a solenoid valve (Pneutronics 11-12-5-BV-12P77) to break the vacuum, is used to transfer plates between the imaging platform and the table. The vacuum pump is controlled via a relay connected to the robot controller (R-30iA). Robot motion programs were written in the FANUC TP language and are solely based on taught coordinates. Execution of robot subroutines is initiated via communication variables through an ethernet (TCP/IP, R-30iA built-in web server) connection.

Image acquisition and imaging platform

Images are recorded using Canon Digital IXUS 70 cameras (Canon Inc., Tokyo, Japan) equipped with CHDK v1.3 (http://chdk.wikia.com/wiki/CHDK, build 4296), an open source firmware addition, enabling camera control with lua scripts executed on the camera, and through ptpcam (http://chdk.wikia.com/wiki/PTP_EXTENSION). The cameras are operated using battery adapters and run off a 4.2V power supply which can be interrupted through the controller of the robotic arm. The power button of each camera is constantly pressed down using a 3D-printed (polylactic acid) clamp to allow for a hard reset by switching off the power. A phototransistor is mounted to the auto focus LED, triggering the vibration motor once the LED is turned on through a second transistor. The execution of lua scripts, downloading and deletion of images is performed through ptpcam with CHDK extensions added. Producing high quality images, unmodified consumer-grade cameras offer several advantages. In contrast to most scientific imaging sensors, they are equipped with fast algorithms to automatically adjust focus, exposure time, and gain. For RAPID, we chose a point-and-shoot

camera model that offers execution of user-written scripts directly on the camera, minimizing communication with the host computer and facilitating parallelization. Our analysis algorithm is independent of specific camera models since consumer-grade cameras generally deliver data in common image file formats (e.g. JPEG) through USB/PTP, eliminating the need of device-specific drivers or hardware extensions to the host PC (Figure 9). There is no restriction in resolution or number of images processed, as the analysis is performed *post hoc* and no active feedback to the imaging platform is required during data acquisition. Compressed raw image data including meta information are preserved so that additional parameters such as velocity, track wavelength, and body bending frequency could be extracted.

The imaging platform is set up as a simplified inverted microscope (Figure 8). The light source is a 12V 35W halogen spot (DECOSTAR 51 SST 4000, OSRAM GmbH, Munich, Germany) powered by a standard ATX PC power supply (2 spots/power supply), followed by a diffuser foil (salvaged from a computer LCD display). The uppermost part of the stage consists of a large glass slide with a 3D-printed (polylactic acid) conical plate holder and a motor holder, equipped with a small vibration motor (salvaged from cordless phones, 12 x 6mm, 3V DC) attached to the slide with epoxy resin. A set of magnifying lenses (PLFILDCCL55, Polaroid 55mm 4-Piece Close Up Camera Lens Filter Kit, purchased from www.amazon.de) projects an image of the plate onto the camera resting on the bottom of the assembly, facing upwards. The frame is made of medium-dense fibreboard, threaded iron rod, and screw nuts, allowing for tuning the alignment of camera, lens assembly, and plate holder. Each imaging platform forms an independent unit, which performs the vibration assay autonomously once the script on the camera has been started. Four of those imaging platforms are mounted on a wooden rack, with diffuser and light source mounted above each unit.

The lua script on the cameras performs the following actions: (1) setup of imaging parameters: setting a predefined optical zoom, automatically adjusting and locking exposure, signal gain, and focus; (2) imaging for 30 s, resulting in 27 images on average, depending on exposure time; (3) turning on autofocus LED for 5 s, triggering the vibrational stimulus; (4) imaging for further 30 s after re-adjustment/re-locking of focus and exposure time (Figure 8). After script execution, the plate is transferred back to its stack. Meanwhile, the images are copied from the camera to the PC and subsequently deleted on the camera. Then, image analysis is performed. After 10 rounds of recording, all cameras are rebooted to prevent random crashes due to memory leaks. If a camera is not responding, an error routine forces a reboot of all cameras and then deletes any images which have been left on their SD cards.

The optical zoom of the camera combined with the lens set results in a pixel length of 6.5 µm. The field of view is ranging from 230 - 250 mm^2 of 870 mm^2 total plate area. Due to chromatic aberration of the lens kit and varying agar thickness near the edge of the plate, the image quality is anisotropic with highest resolution at the center of the image. Worms moving close to the edge of the image tend to be slightly out of focus resulting in blurred tracks, which are detectable nonetheless. As the seeded OP50 spot is in the center of the plate, worms tend to stay closer to the middle of the image rather than the edge, allowing for better detection.

Image compression and analysis

The image download directory is scanned regularly for unprocessed images and compression/analysis is performed as needed. First, the image files (jpeg-compressed RGB, 8 bit/channel) from the camera are combined into a movie (libx264, AVI container) using avconv (Libav 9.18, Libav developers 2016) while the metadata of the images are extracted using exiv2 (Andreas Huggel, The Exiv2 Project) and saved in a text file. A second script finds the compressed videos and extracts motion from before and after the vibrational stimulus using python 2.7 (Python Software Foundation) and the python bindings for the open source computer vision library (openCV 2.4.8, Itseez). A minimum projection of sequential images is performed and the first frame of each series is subtracted from the final projection. The resulting image summarizes all changes in intensity during the recording series, i.e. the track of a moving worm and noise. This image is then smoothed, converted to a binary image using adaptive mean thresholding and the number of non-zero pixels is counted and saved to a file, reflecting the total area the worm has crawled over during the recording. The extraction of worm tracks is performed for the interval before and after the vibrational stimulus separately. The compression and analysis are run in parallel using GNU Parallel (https://www.gnu.org/software/parallel) allowing fast processing of the acquired data on a multiprocessor (x86_64, AMD Opteron, 16 cores, 75 GB RAM) computer.

The thresholded track, number of pixels and the first image of each data point are superimposed and all superimposed images of a given worm are compiled into one mosaic bitmap. This mosaic is then visually inspected for plate contamination, thresholding errors, and other artifacts. Specific time points are excluded from the analysis using an image browser macro written in ImageJ macro language.

Worm strain maintenance and preparation for RAPID assay

The following worm strains were provided by the *C. elegans* Genetics Center (CGC, funded by NIH Office of Research Infrastructure Programs P40 OD010440):
CB120 [*unc-4(e120)* II., *daf-2(sa875)* III.] (Brenner, 1974), CB246 [*unc-64(e246)* III.] (Brenner, 1974), CB306 [*unc-50(e306)* III.] (Brenner, 1974), CB1072 [*unc-29(e1072)* I.] (Brenner, 1974; Lewis et al., 1980), CL2355 [*smg-1(cc546)*, *dvIs50*[*pCL45 (snb-1::aβ(1-42)::3' UTR(long) + mtl-2::gfp*] I.] (Dosanjh et al., 2010), LS292 [*dys-1(cx18)* I.] (Gieseler et al., 1999), MT2426 [*goa-1(n1134)* I.] (Segalat et al., 1995; Van Swinderen et al., 2001), N2, TJ1052 [*age-1(hx546)* II.] (Friedman and Johnson, 1988), ZZ17 [*lev-10(x17)* I.] (Lewis et al., 1980). Worms were cultivated on 3.5 cm NGM plates seeded with *E. coli* OP50 (Stiernagle, 2006) at 20 °C. For the assay, worms were synchronized by picking 10-15 gravid adults in a 100 µl droplet of hypochlorite solution (8.25 ml dH_2O, 3.75 ml 1M NaOH, 3 ml Sodium hypochlorite 6-14% active chlorine, Sigma-Aldrich Chemie GmbH Buchs, Switzerland) on seeded NGM plates, which were kept at room temperature. Worms were singled on assay plates two days later, at L3/L4 stage. Plates were labelled with a unique identifier, time of birth, and array coordinates and sealed with a 10 x 1 cm strip of Parafilm M® (Bemis, USA). The sealed plates, in stacks of four, were placed upside down onto the storage grid (Figure 3 c). At the same time, each plate's position was entered into the sample lookup table file. Once all plates were placed onto the grid, the assay was started.
Assay plates: 3.5 ml of NGM agar containing 10 µg/ml 2′-Deoxy-5-fluorouridine (FUdR, Sigma-Aldrich Chemie GmbH Buchs, Switzerland) were poured in 3.5 cm Petri dishes. Plates were stored in closed containers for up to one week, prior seeding. Plates were

seeded the day before the assay was started with 15 µl OP50 cultured in LB broth overnight, carefully placing the drop in the center of the plate. Hands-on times are summarized in Table 9.

Modelling and statistical tests

We used the lme function of the nlme package (https://cran.r-project.org/web/package=nlme) in R (https://www.r-project.org, version 3.2.3) to fit linear mixed-effect models to our assay data. We predicted track area by genotype or condition, time, temperature, and the interaction of genotype with time. Slopes and intercepts were allowed to vary for a given subject as random effects. For linear versus quadratic comparisons, a fixed effect for $time^2$ was added to the model, without including additional higher-order interactions. Correlation of the data was modeled using the corCAR1 function. For model comparison, models were fit by maximizing the log-likelihood; final models were fit by maximizing the restricted log-likelihood. Model selection was performed in a bottom-up approach, sequentially adding fixed effects and interactions. If a fixed effect significantly improved the model, the fixed effect was included.
Intercept and slope parameters for each condition/genotype were compared to reference parameters (Table 4 and Table 5). p-values indicate the probability of observing these coefficients under the assumption of each condition/genotype having the same coefficients as the reference.
Normal distribution of residuals was checked using diagnostic plots (Figure 10, Figure 11). Population predictions were computed using the *predict* function with the mean temperature of each set as temperature level. Timepoints after day 3 were included in the analysis to ensure we only consider tracks from adults and worms have fully adjusted to the new environment after initial transfer. Lifespan data was extracted from the same data set, by determining the time point at which a worm produced at least two track areas > 0 within 3 recordings, to filter for noise. Lifespan analysis was performed using the *survfit* function from the survival package (https://cran.r-project.org/web/packages/survival/) and Kaplan-Meier plots were generated using the survminer package (https://cran.r-project.org/web/packages/survminer/).

3.1.6 Results

RAPID setup

RAPID consists of four individual optical imaging platforms, a storage array of NGM Petri dishes each containing a single worm, and a robotic arm (Figure 3). The robotic arm transfers the plates from the storage array to the imaging platforms and back, recording 280 worms over several weeks without experimenter intervention. The imaging platforms feed raw data into an automatic image processing pipeline (Figure 8, Figure 9).

The vibration stimulus applied during the assay causes the plates to slightly bounce, constantly tapping against the plate holder. In wild type worms, tapping usually results in reversal of direction, or accelerated forward movement (Wicks and Rankin, 1995). Tap and touch response have been studied in great detail, revealing the underlying neural circuits (Wicks and Rankin, 1995; Chalfie et al., 1985; Rose, 2001). As the plates move during the vibratory stimulus, the system does not detect the initial response to the first tap and therefore relies on the increased locomotor activity during 30 s after stimulus cessation (Figure 8 b). Unmodified consumer-grade cameras were used for image acquisition. In summary, RAPID performs repetitive, standardized, non-destructive neurological examinations of individual worms.

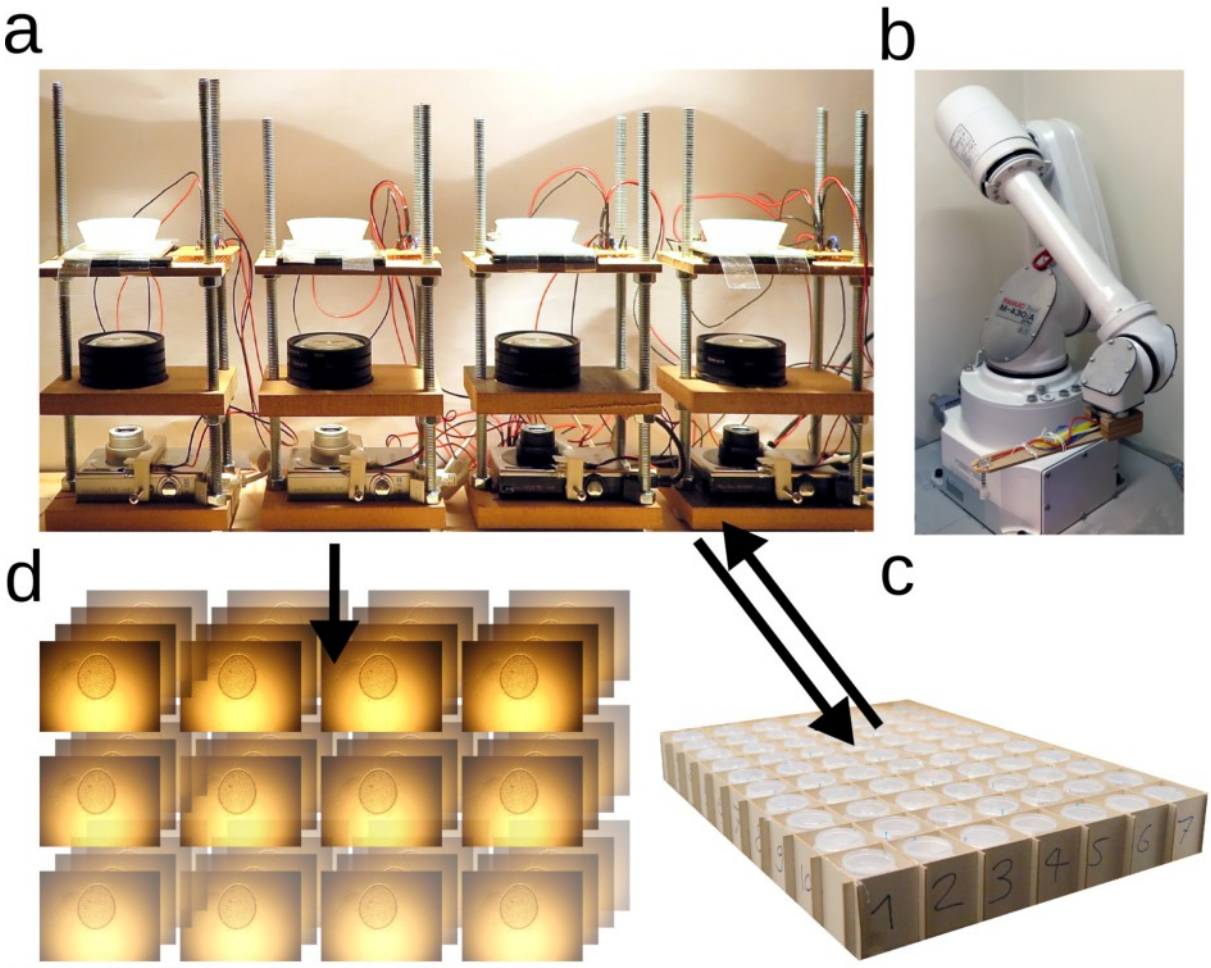

Figure 3: Working Principle of RAPID

Four individual imaging platforms **(a)**, see also Figure 8, are continuously loaded with plates containing single worms, using a robotic arm **(b)**. Up to 280 plates are stored in an array **(c)** which are sequentially cycled and imaged for 1 min every 6.2 h. A vibrational stimulus is applied during recording to provoke motion of the worms. After the imaging is complete, plates are put back to the array and the images are downloaded and processed **(d)**. Note: The camera model IXUS 70 comes in different exterior designs, hence the different chassis colours.

RAPID provides unbiased lifelong longitudinal data allowing modeling of functional decline during ageing

As a proof-of-principle experiment, we first performed lifelong recordings of 10 different *C. elegans* strains in a single run, to test whether standardized stimulus application and automated track quantification would allow the unbiased comparison of different worm strains. Tested strains included wild type (N2), four uncoordinated, one hyperactive, one progressively paralysed, one long-lived, and two levamisole-resistant strains. Worms were censored if they failed to produce a single track due to damage during their initial manual transfer to the plates, or due to crawling off the plate. The median number of worms included in the analysis were 23.5 from the initial 28 worms per strain or 239 out of 280 worms in total. All worms were associated with a unique identifier, enabling per worm motility vs. age plots. Worms of the same genotype or treatment were plotted in groups, revealing distinct decline patterns (Figure 4, Figure 11). The rate of decline was quantified by fitting a linear mixed-effect model to the raw data to compare the rate of decline in relation to a reference strain. The fitted parameters of the worm strains plotted in Figure 4 are summarized in Table 4. All strains tested had a lower intercept, i.e. theoretical track area at time 0 h, compared to wild type with the exception of the hyperactive strain LS292 [*dys-1(cx18)* I.]. Motility profiles were all significantly different from wild type (Table 4). The lowest intercept values were recorded for the uncoordinated strain CB306 [*unc-50(e306)* III.]. The rates of locomotor decline for all strains tested were lower than wild type except for the hyperactive strain LS292 [*dys-1(cx18)* I.]. With the exception of the levamisole-resistant strain ZZ17 [*lev-10(x17)* I.] in absence of levamisole, all examined parameters significantly differed from the respective wild type values. Thus, measuring the track area every 6.2 h directly quantified stimulus response and motility decline in the ageing worm.

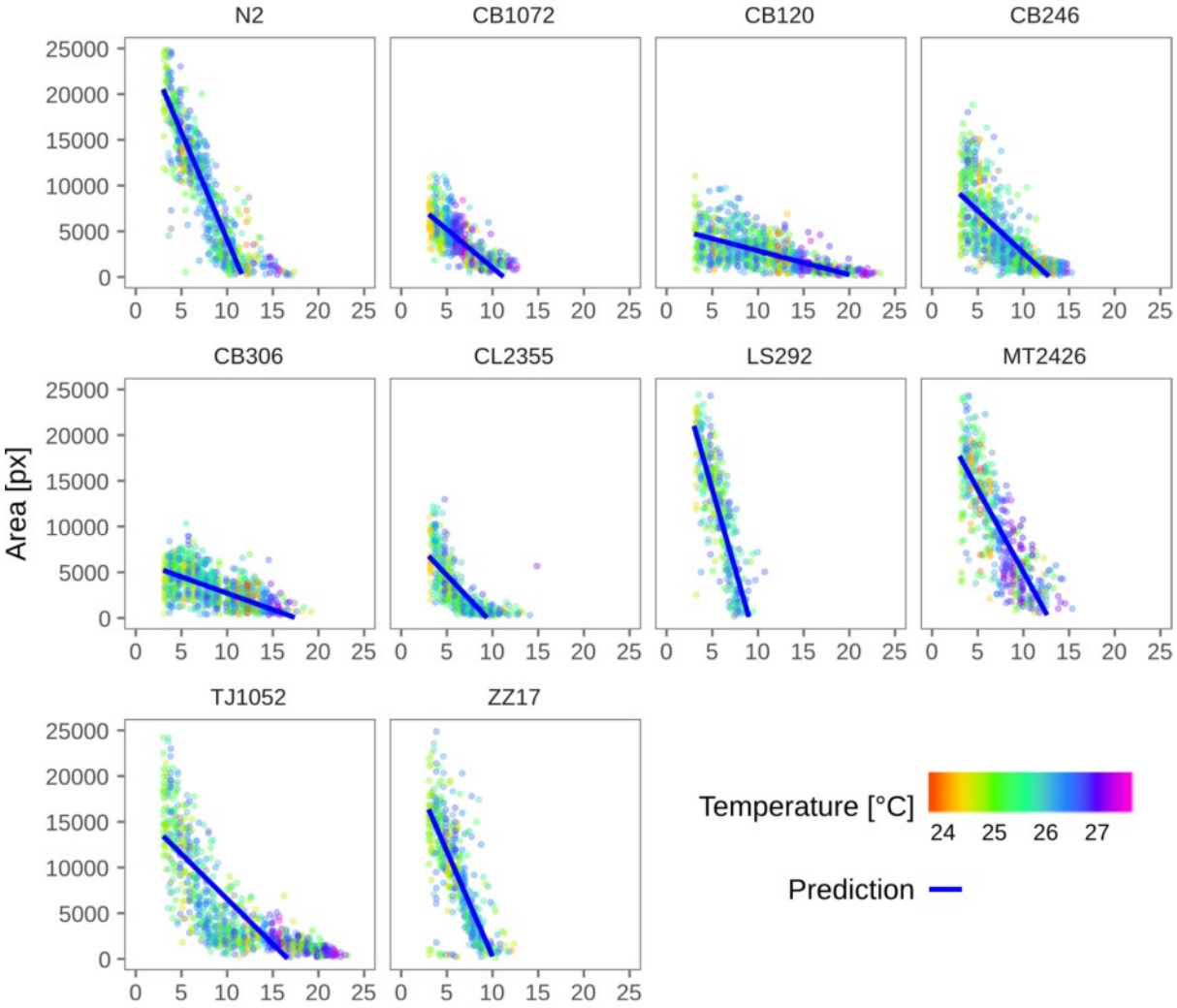

Figure 4: Motility Decline Profiles in Various Mutant Backgrounds

Track area vs. days in wild type (N2) and nine mutant strains as indicated below graphs. Day 0 indicates date of birth, the assay was started at day 3. Colour indicates temperature at the time the assay was performed, blue lines indicate the predicted values of the fitted model. Number of worms per group are indicated in Table 7.

	Value	Std Error	DF	t value	p value
N2 (Intercept)	23735.66	1259.40	6064	18.85	<0.001
days	-2348.94	93.36	6064	-25.16	<0.001
CB1072	-18191.13	1095.56	229	-16.60	<0.001
CB120	-22051.65	1168.54	229	-18.87	<0.001
CB246	-15689.26	1061.47	229	-14.78	<0.001
CB306	-21272.04	1094.93	229	-19.43	<0.001
CL2355	-17627.05	1131.97	229	-15.57	<0.001
LS292	3895.36	1218.70	229	3.20	<0.002
MT2426	-4439.58	1157.50	229	-3.84	<0.002
TJ1052	-11171.86	1072.66	229	-10.42	<0.001
ZZ17	-4296.05	1158.84	229	-3.71	<0.001
temperature	144.82	37.53	6064	3.86	<0.001
days:CB1072	1512.70	133.65	6064	11.32	<0.001
days:CB120	2084.91	133.07	6064	15.67	<0.001
days:CB246	1425.61	123.67	6064	11.53	<0.001
days:CB306	1989.59	126.80	6064	15.69	<0.001
days:CL2355	1294.03	140.06	6064	9.24	<0.001
days:LS292	-1134.61	160.22	6064	-7.08	<0.001
days:MT2426	538.20	137.04	6064	3.93	<0.001
days:TJ1052	1364.06	123.00	6064	11.09	<0.001
days:ZZ17	48.84	144.55	6064	0.34	0.74

Table 4: Fitted Coefficients of the Different C. elegans Mutants

Intercepts and slopes of strains are relative to the reference strain (N2), p-values indicate probability of observing these coefficients under the assumption, each strain having the same coefficients as N2.

Models for age-related motility decline

For wild type worms, a linear decline (Bolanowski et al., 1981; Johnson et al., 1988; Duhon and Johnson, 1995) (by measuring wave frequency while moving forward), an exponential decline (Liu et al., 2013; Hsu et al., 2009), and a quartic decline with higher order interactions (Bansal et al., 2015) have been proposed to model the rate of change in motility over time. We have tested these models on our data and find that wild type data is best represented by a quadratic function (Figure 12, Table 8). However, linear decline models fit to our data almost equally well (Figure 13), in particular if mutant and transgenic strains are considered as well.

Effects of 5-fluoro-2'-deoxyuridine on wild type motility

As NGM plates seeded with single fertile *C. elegans* hermaphrodites will become populated with hundreds of progeny, precluding any type of individual worm examination, some sort of sterility is required. To ensure high-throughput with assays like RAPID, absence of vital offspring is a prerequisite, as even larvae would be detected by the currently implemented image processing, causing erroneous track detection. 5-fluoro-2′-deoxyuridine (FUdR) is an inhibitor of thymidylate synthetase (Santi and Mchenry, 1972; Esposito and Holliday, 1964), widely used for its sterilizing effect on *C. elegans* (Hosono, 1978) by blocking DNA synthesis and decreasing germ cell proliferation. When provided to *C. elegans* larvae before most cells are postmitotic, FUdR leads to a decreased body size (Hosono, 1978). Therefore, FUdR is usually applied to later larval stages or adults.
When applied later in adult life, FUdR has been shown to dramatically increase the lifespan of some mutants, but not of wild type, in a dose-dependent manner (Hosono, 1978; Aitlhadj and Stürzenbaum, 2010; Van Raamsdonk and Hekimi, 2011; Gandhi et al., 1980). Furthermore, FUdR increases resistance to proteotoxic stress (Angeli et al., 2013; Feldman et al., 2014) and prolongs survival under osmotic stress (Anderson et al., 2016). There is evidence for deleterious effects on motility with FUdR use (Bolanowski et al., 1981; Glenn et al., 2004). As our assay does not allow to directly compare wild type worms with and without FUdR, we applied three different FUdR concentrations to wild type worms and compared their decline in motility against the lowest concentration (Figure 5, Table 5, Figure 10). The parameter for intercept and slope of 20 µg/ml and 40 µg/ml FUdR treated animals are not significantly different from 10 µg/ml FUdR, suggesting any effects FUdR might have on motility are not dose-dependent in wild type *C. elegan*s.

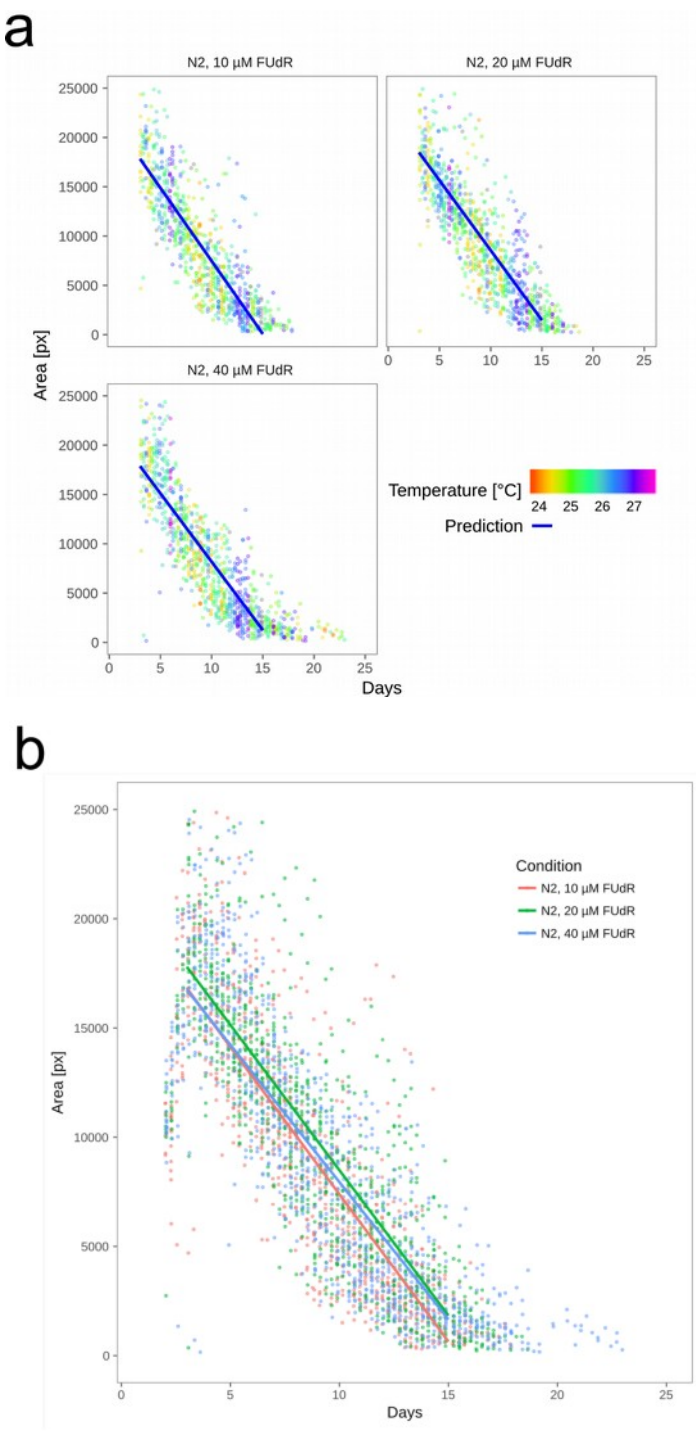

Figure 5: Effect of FUdR Concentration on N2

(a) Track area throughout life, day 0 indicates date of birth. The assay was started at day 3. Colour indicates temperature at the time each assay was performed. Three concentrations of FUdR were tested, 10 µg/ml (n = 21), 20 µg/ml (n = 24), and 40 µg/ml (n = 24). Blue lines indicate the predicted values of the fitted model. **(b)** Same datasets summarized in one plot. Dots represent individual measurements, lines are predicted values from the fitted model. Colours indicate different FUdR concentrations.

Lifespan determination from RAPID data

Since each RAPID examination starts with a cohort of young adult worms and is terminated after the last individual has died, high-resolution lifespan data can be extracted from our datasets. Traditionally, lifespan is assessed by inspecting worm cohorts on NGM plates every day or every other day (Wilkinson et al., 2012). Worms which do not move and which do not respond to prodding with a worm pick are defined as dead. Thus, except for the mechanical vibratory stimulus which replaces individual prodding, RAPID conditions are identical to the classical lifespan assay. We defined the time of death as the last time point at which a worm showed a response to the vibrational stimulus, and had at least one valid track in the previous two rounds, in order to filter out noise (as detailed in the methods section). Thus, given its imaging cycle, RAPID allowed lifespan determination with an accuracy of 6.2 hours. FUdR concentration does only have minimal effects on wild type lifespan (Figure 6 a, Table 6) which is in concordance with the overall motility decline that is only insignificantly influenced by FUdR concentration. Lifespan of certain mutants significantly differs from wild type (Figure 6 b, Table 7). To demonstrate age-related functional decline, we used individual lifespan to normalize the corresponding motility dataset and plotted these data in a group-wise manner (Figure 7). Our data show that none of the mutant/transgenic strains tested performs better than wild type.

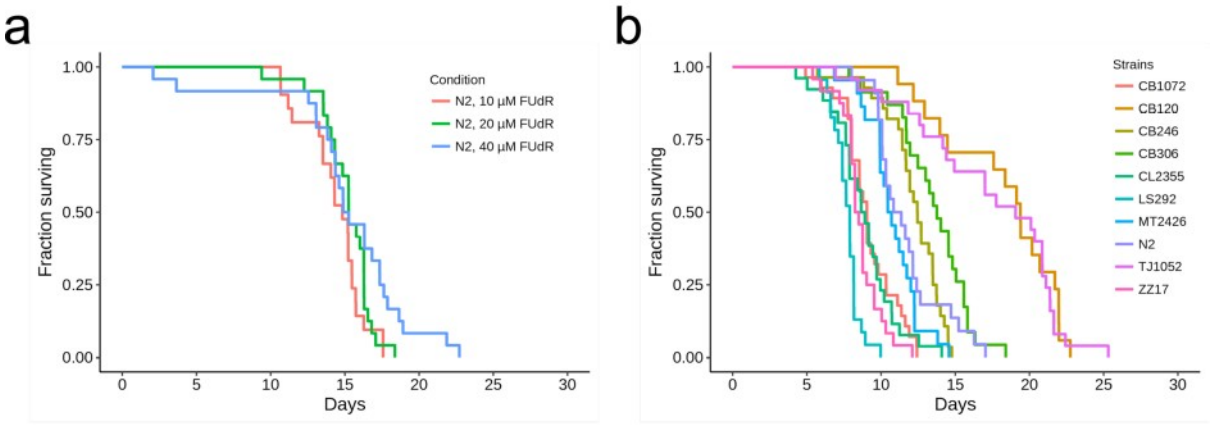

Figure 6: Survival Curves Based on RAPID Data

(a) Survival data from wild type at various FuDR concentrations: Kaplan-Meier survival curves generated from the FUdR data set (Figure 5). Day 0 indicates time of birth, the assay was started on day 2. Median survival and number of worms are indicated in Table 6. **(b)** Survival differences between wild type and mutants: Kaplan-Meier survival curves generated from the same data set as in Figure 4. Median survival and number of worms are indicated in Table 7.

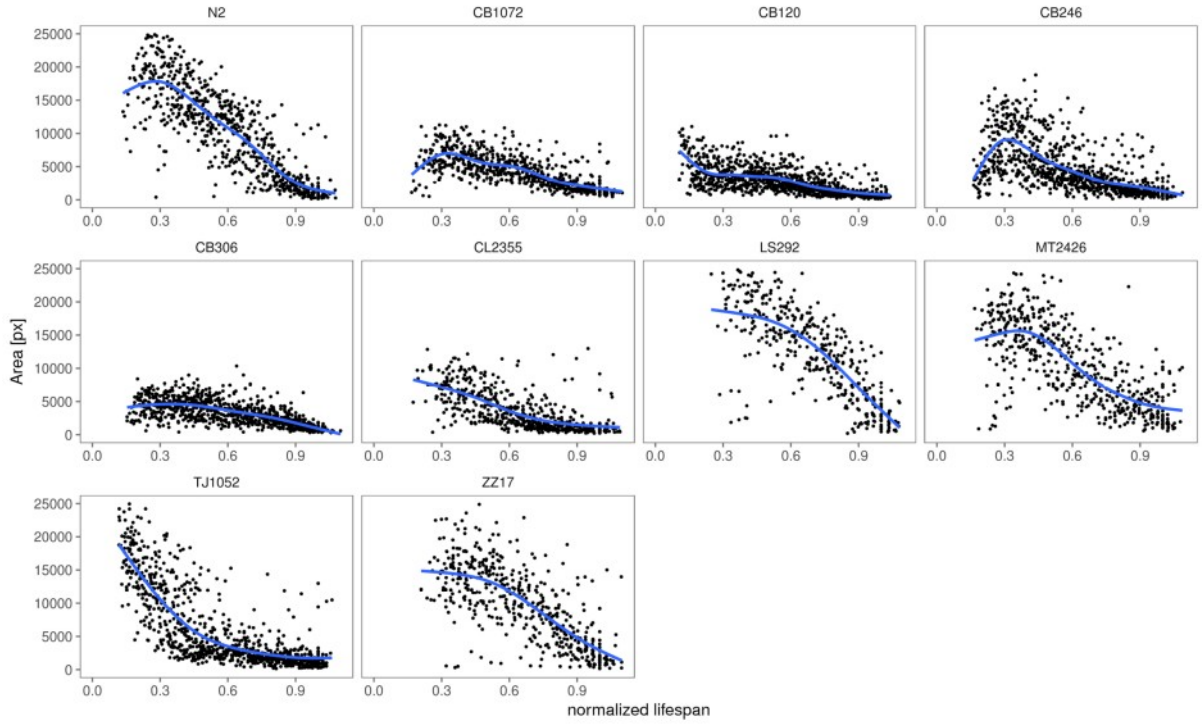

Figure 7: Track Area Over Normalized Lifespan in Various Worm Strains

Lifespan data (Figure 4, Figure 6 b) is normalized per worm. No mutant or transgenic strain in our series performs better than wild type. In contrast, the long-lived strains (TJ1052 [*age-1(hx546)* II.] and CB120 [*unc-4(e120)* II., *daf-2(sa875)* III.]) all perform worse than wild type.

3.1.7 Discussion

The need for inter-laboratory standardization of lifespan assessments has recently been addressed by the formation of the *Caenorhabditis* Intervention Testing Program (CITP) (Lucanic et al., 2017). The aim of CITP is to identify and test compounds which prolong lifespan and have a positive effect on health. We believe that RAPID complements the standardization efforts of CITP by contributing valuable quantitative health and lifespan data, allowing a more rigorous compound evaluation.

Combining longitudinal single worm tracking with an automated, high-throughput system offers many possibilities for future research, in particular to study health during the ageing process. Other appealing phenomena to be quantified include response to external physical and chemical conditions, potentially in combination with large numbers of well-characterized genetic mutants. In particular, long-term toxicity studies and drug discovery would be applications where effects are not expected to occur instantaneously. Since response to stimuli with motor output involves portions of the *C. elegans* nervous system responsible for sensing, signal processing, and muscle activity, our assay is furthermore suitable to quantitatively assess neurodegeneration. With RAPID, we developed such a screening system which enables simultaneous, lifelong longitudinal recordings of 280 single worms on standard NGM plates. A vibratory stimulus ensures the observation of worms in an active state, allowing full assessment of motion capabilities within 30 s. This decreases the time required for evaluation compared to worms that are in a dwelling state, and increases assay sensitivity. Due to the latency of several hours between the measurements, habituation and fatigue are unlikely, and repeated stimuli will provoke comparable responses (Beck and Rankin, 1997; Rankin and Broster, 1992). Compared to existing longitudinal recording assays (Zhang et al., 2016; Hulme et al., 2011; Cornaglia et al., 2016), RAPID uses NGM plates which do not require special fabrication techniques, and which are compatible with standard *C. elegans* laboratory culture conditions. Single plates enable the combination of motility assessment using RAPID with other non-invasive assays such as high-resolution microscopy.

If unperturbed and on NGM, seeded with the *E. coli* strain OP50, *C. elegans* spends about 78% in a state of dwelling with little displacement and low velocities, and 22% in a state of roaming (Ryan et al., 2014; Fujiwara et al., 2002; Ben Arous et al., 2009). The preferences for dwelling and roaming depend on food quality (Shtonda, 2006). We chose vibration as stimulus to provoke dwelling and roaming worms to move faster, as it can be applied repeatedly and reproducibly invokes a reaction. In theory, any other non-invasive stimulus that acts on a sealed plate could be used, such as single taps (Rankin, 1991), heat (Wittenburg and Baumeister, 1999), light of short wavelength (Edwards et al., 2008), or light in combination with optogenetics (Stirman et al., 2011). The only limitation in terms of longitudinal recording is restriction to non-permanent and non-destructive stimuli.

Identification of lifespan phenotypes induced by mutations, dietary restrictions, or other interventions has led to major insights into the physiology and genetics of ageing (Kenyon, 2010). It has been noted, that lifespan increase *per se* is not necessarily meaningful, especially if the ultimate goal is to translate findings from *C. elegans* research to life-extending interventions in humans (Bansal et al., 2015). The term "healthspan" has been

coined to describe the period of time an individual spends in good health, before the onset of age-related decline, whereas "gerospan" denotes the time spent in poor health until death. Consequently, the goal of any ageing-modifying intervention should be to increase healthspan without prolonging gerospan. As health is not a static condition but rather a continuum, dividing the life of a worm into healthspan and gerospan by a fixed threshold is arbitrary. Instead of measuring the number of days spent above a certain threshold, we propose to model the decline of motility over time using linear mixed-effect models. Such models allow any function to be fit to a given dataset. The selection of an appropriate function involves checking the goodness of fit with the observed values. By choosing a reference strain in a reference condition, the function of healthy ageing is defined. Strains or conditions are directly compared to the reference, and the relative capabilities are indicators for an improved or decreased overall health rather than healthspan. Through their high temporal resolution, RAPID data enable full use of the powerful linear-mixed effect models to accurately describe the decline in motility over time. When considering our dataset of nine mutant worm strains and wild type, a linear model of decline is preferable (Figure 13), as the data from the mutant strains CB120 [*unc-4(e120)* II., *daf-2(sa875)* III.] and CB306 [*unc-50(e306)* III.] are in disagreement with a quadratic function. By fitting our RAPID data with a linear function to compare all strains in an unbiased fashion, we find our system capable of differentiating physiological ageing, i.e. healthspan (Bansal et al., 2015), from simple extension of life, a phenomenon not necessarily aimed for in human medicine. Therefore, we propose to use RAPID as a platform to screen for ageing modifying compounds, mutations, or transgenes.

Higher performance than a reference strain would require to present with either a higher starting value, i.e. intercept β_0, or a slower motility decline rate β_1 (decline in area per day) with none of either parameter indicating worse performance than the reference:

$$\beta_0^{\text{strain}} \geq \beta_0^{\text{reference}} \wedge \beta_1^{\text{strain}} \leq \beta_1^{\text{reference}}$$

None of the tested strains matches these criteria (Table 4). Hence, we conclude, that wild type has the best motility capabilities, which is particularly highlighted upon normalization of motility decline over individual lifespan (Figure 7). The hyperactive strain LS292 [*dys-1(cx18)* I.] shows a normalized decline rate similar to wild type, but has a shorter lifespan, and hence worse capabilities. This normalization furthermore reveals that lifespan extension in the long-lived strains TJ1052 [*age-1(hx546)* II.] and CB120 [*unc-4(e120)* II., *daf-2(sa875)* III.] does not extend healthspan.

As shown in Figure 4, a linear model is in agreement with 9/10 strains tested in our assay, with the exception of the long-lived mutant TJ1052 [*age-1(hx546)* II.]. TJ1052 [*age-1(hx546)* II.] was previously assessed (Duhon and Johnson, 1995) by measuring the spontaneous wave frequency during swimming in liquid at 20 °C. The authors reported the decline of motility to decrease linearly over time. Our experiment shows a faster decline during the first 8 days, followed by a slower decrease rate until death. This two-phase decline is not a group-derived effect but is also observed in individual worms of this genotype (Figure 14). Hence, a linear function does not accurately describe the decline over time in TJ1052 [*age-1(hx546)* II.]. The negative deviation from the predicted linear decline indicates that the ageing process does not scale with lifespan, and that TJ1052 [*age-1(hx546)* II.] shows decreased motion capabilities later in life.

This suggests that the ageing process of TJ1052 [*age-1(hx546)* II.] functionally differs from wild type. The lifespan extension in TJ1052 [*age-1(hx546)* II.] does not increase overall health, and therefore does not increase any arbitrarily defined healthspan. Similar observations have been made on *daf-2* mutants: One study reported a shorter healthspan in *daf-2* mutants normalized for lifespan by measuring total distance covered during 5 min on seeded plates (Bansal et al., 2015) while another research team concluded that normalized healthspan was equal to wild type based on measuring the maximum velocity crawled in 30 s on unseeded plates (Hahm et al., 2015). Interestingly, the uncoordinated strain CB120 [*unc-4(e120)* II., *daf-2(sa875)* III.] showed a dramatically increased lifespan, even longer than the lifespan of TJ1052 [*age-1[hx546)* II]. The median lifespan fo*r unc-4(e120)* carrying hermaphrodites was previously reported to be 12.4 ± 2 days at 20 °C (Gems and Riddle, 2000). As CB120 [*unc-4(e120)* II., *daf-2(sa875)* III.], was reported to contain the additional *daf-2(sa875)* mutation (Ailion and Thomas, 2003), this might explain the overall decreased motility, inferred by *unc-4(e120)* combined with longevity due to *daf-2(sa875)* in CB120.

In summary, RAPID is a high-throughput, fully automated *C. elegans* recording system that employs standard vermiculture conditions. By utilizing linear mixed-effect models that reflect the age-dependent decline in motor performance (rather than arbitrary thresholds that divide adult life into healthspan and gerospan), RAPID enables objective quantification of the health impact of genetic and environmental factors throughout worm life. Thus, our system, which is easy to implement on a comparably small budget, should allow for robust inter-laboratory reproducibility of worm experiments. Finally, we propose that the standardized RAPID assays will be instrumental for ageing research on *C. elegans*, being particularly useful for health assessment and modelling of physiological ageing.

3.1.8 Disclosure statement

The authors declare no competing financial interests.

3.1.9 Acknowledgments

M.T. is supported by the Swiss National Science Foundation (31003A_152846). R.D.-R. was supported by PhD fellowship CAPES 99999.012331/2013-09. We thank Drs. Gilles Dutilh and Deborah Vogt of the Clinical Trial Unit for reviewing our statistical evaluation and helpful suggestions, and Ralph Schoch, Institute of Medical Genetics and Pathology (all Basel University Hospital), for technical support.

Material and equipment were supported by Forschungsfonds der Universität Basel; Fondation Floshield, Neuchâtel; and Fanuc, Biel (all Switzerland). Some *C. elegans strains* were provided by the CGC, which is funded by NIH Office of Research Infrastructure Programs (P40 OD010440).

Author Contributions: J.H. and G.S. conceived the project, designed, developed, and constructed the RAPID system including software and analyzed all data. G.S., I.B.H., and R.D-R. carried out *C. elegans* maintenance and preparation. J.H., G.S., and F.S. wrote the manuscript. All authors provided comments and contributions. F.S. and M.T. supervised the project.

3.1.10 References

Ailion, M., and J.H. Thomas. 2003. Isolation and characterization of high-temperature-induced dauer formation mutants in Caenorhabditis elegans. *Genetics*. 165:127–144.

Aitlhadj, L., and S.R. Stürzenbaum. 2010. The use of FUdR can cause prolonged longevity in mutant nematodes. *Mech. Ageing Dev.* 131:364–365. doi:10.1016/j.mad.2010.03.002.

Anderson, E.N., M.E. Corkins, J.C. Li, et al., 2016. C. elegans lifespan extension by osmotic stress requires FUdR, base excision repair, FOXO, and sirtuins. *Mech. Ageing Dev.* 154:30–42. doi:10.1016/j.mad.2016.01.004.

Angeli, S., I. Klang, R. Sivapatham, K. Mark, D. Zucker, D. Bhaumik, G.J. Lithgow, and J.K. Andersen. 2013. A DNA synthesis inhibitor is protective against proteotoxic stressors via modulation of fertility pathways in Caenorhabditis elegans. 5:759–769.

Ben Arous, J., S. Laffont, and D. Chatenay. 2009. Molecular and sensory basis of a food related two-state behavior in C. elegans. *PLoS One*. 4:1–8. doi:10.1371/journal.pone.0007584.

Bansal, A., L.J. Zhu, K. Yen, and H.A. Tissenbaum. 2015. Uncoupling lifespan and healthspan in Caenorhabditis elegans longevity mutants. *Proc. Natl. Acad. Sci.* 112:E277–E286. doi:10.1073/pnas.1412192112.

Beck, C.D.O., and C.H. Rankin. 1997. Long-term habituation is produced by distributed training at long ISIs and not by massed training or short ISIs inCaenorhabditis elegans. *Anim. Learn. Behav.* 25:446–457. doi:10.3758/BF03209851.

Bolanowski, M.A., R.L. Russell, and L.A. Jacobson. 1981. Quantitative measures of aging in the nematode Caenorhabditis elegans. I. Population and longitudinal studies of two behavioral parameters. *Mech. Ageing Dev.* 15:279–295. doi:10.1016/0047-6374(81)90136-6.

Brenner, S. 1974. The genetics of Caenorhabditis elegans. *Genetics*. 77:71–94. doi:10.1002/cbic.200300625.

Chalfie, M., J.E. Sulston, J.G. White, E. Southgate, J.N. Thomson, and S. Brenner. 1985. The neural circuit for touch sensitivity in Caenorhabditis elegans. *J. Neurosci.* 5:956–64. doi:3981252.

Cornaglia, M., G. Krishnamani, L. Mouchiroud, V. Sorrentino, T. Lehnert, J. Auwerx, and M.A.M. Gijs. 2016. Automated longitudinal monitoring of in vivo protein aggregation in neurodegenerative disease C. elegans models. *Mol. Neurodegener.* 11:17. doi:10.1186/s13024-016-0083-6.

Croll, N. a, J.M. Smith, and B.M. Zuckerman. 1977. The aging process of the nematode Caenorhabditis elegans in bacterial and axenic culture. *Exp. Aging Res.* 3:175–189. doi:10.1080/03610737708257101.

Dosanjh, L.E., M.K. Brown, G. Rao, C.D. Link, and Y. Luo. 2010. Behavioral phenotyping of a transgenic caenorhabditis elegans expressing neuronal amyloid-?? *J. Alzheimer's Dis.* 19:681–690. doi:10.3233/JAD-2010-1267.

Duhon, S.A., and T.E. Johnson. 1995. Movement As an Index of Vitality - Comparing Wild-Type and the age-1 Mutant of Caenorhabditis elegans. *Journals Gerontol. Ser. a-Biological Sci. Med. Sci.* 50:B254–B261.

Edwards, S.L., N.K. Charlie, M.C. Milfort, B.S. Brown, C.N. Gravlin, J.E. Knecht, and K.G. Miller. 2008. A novel molecular solution for ultraviolet light detection in Caenorhabditis elegans. *PLoS Biol.* 6:1715–1729. doi:10.1371/journal.pbio.0060198.

Esposito, R.E., and R. Holliday. 1964. The Effect of 5-Fluorodeoxyuridine on Genetic Replication and Mitotic Crossing over in Synchronized Cultures of Ustilago Maydis. *Genetics*. 50:1009–1017.

Feldman, N., L. Kosolapov, and A. Ben-Zvi. 2014. Fluorodeoxyuridine improves Caenorhabditis elegans proteostasis independent of reproduction onset. *PLoS One*. 9:1–9. doi:10.1371/journal.pone.0085964.

Friedman, D.B., and T.E. Johnson. 1988. A mutation in the age-1 gene in Caenorhabditis elegans lengthens life and reduces hermaphrodite fertility. *Genetics*. 118:75–86.

Friend, J., and L. Yeo. 2010. Fabrication of microfluidic devices using polydimethylsiloxane. *Biomicrofluidics*. 4:1–5. doi:10.1063/1.3259624.

Fujiwara, M., P. Sengupta, and S.L. McIntire. 2002. Regulation of body size and behavioral state of C. elegans by sensory perception and the egl-4 cGMP-dependent protein kinase. *Neuron*. 36:1091–1102. doi:10.1016/S0896-6273(02)01093-0.

Gandhi, S., J. Santelli, D.H. Mitchell, J. Wesley Stiles, and D. Rao Sanadi. 1980. A simple method for maintaining large, aging populations of Caenorhabditis elegans. *Mech. Ageing Dev.* 12:137–150. doi:10.1016/0047-6374(80)90090-1.

Gems, D., and D.L. Riddle. 2000. Genetic, behavioral and environmental determinants of male longevity in Caenorhabditis elegans. *Genetics*. 154:1597–1610. doi:10.1093/gerona/gls088.

Gieseler, K., C. Bessou, and L. Ségalat. 1999. Dystrobrevin- and dystrophin-like mutants display similar phenotypes in the nematode Caenorhabditis elegans. *Neurogenetics*. 2:87–90. doi:10.1007/s100480050057.

Glenn, C.F., D.K. Chow, L. David, C.A. Cooke, M.S. Gami, W.B. Iser, K.B. Hanselman, I.G. Goldberg, and C.A. Wolkow. 2004. Behavioral deficits during early stages of aging in Caenorhabditis elegans result from locomotory deficits possibly linked to muscle frailty. *J. Gerontol. A. Biol. Sci. Med. Sci.* 59:1251–60. doi:10.1116/1.2998754.A.

Hahm, J.-H., S. Kim, R. DiLoreto, C. Shi, S.-J. V Lee, C.T. Murphy, and H.G. Nam. 2015. C. elegans maximum velocity correlates with healthspan and is maintained in worms with an insulin receptor mutation. *Nat. Commun.* 6:8919. doi:10.1038/ncomms9919.

Hosono, R. 1978. Sterilization and growth inhibition of Caenorhabditis elegans by 5-fluorodeoxyuridine. *Exp. Gerontol.* 13:369–373. doi:10.1016/0531-5565(78)90047-5.

Hsu, A.-L., Z. Feng, M.-Y. Hsieh, and X.Z.S. Xu. 2009. Identification by machine vision of the rate of motor activity decline as a lifespan predictor in C. elegans. *Neurobiol. Aging*. 30:1498–1503. doi:10.1016/j.neurobiolaging.2007.12.007.

Huang, C., C. Xiong, K. Kornfeld, and J.I. Gordon. 2004. Measurements of Age-Related Changes of Physiological Processes That Predict Lifespan of Caenorhabditis elegans. *Source Proc. Natl. Acad. Sci. United States Am.* 101:8084–8089. doi:10.1073/pnas.0400848101.

Hulme, S.E., S.S. Shevkoplyas, A.P. McGuigan, J. Apfeld, W. Fontana, and G.M. Whitesides. 2011. Lifespan-on-a-chip: microfluid chambers for performing lifelong observations of C. elegans. *Lab Chip*. 10:589–597. doi:10.1039/b919265d.Lifespan-on-a-chip.

Husson, S.J. 2012. Keeping track of worm trackers. *WormBook*. 7:1–17. doi:10.1895/wormbook.1.156.1.

Johnson, T.E., W.L. Conley, and M.L. Keller. 1988. Long-lived lines of Caenorhabditis elegans can be used to establish predictive biomarkers of aging. *Exp. Gerontol.* 23:281–295. doi:10.1016/0531-5565(88)90031-9.

Kenyon, C., J. Chang, E. Gensch, A. Rudner, and R. Tabtiang. 1993. A C. elegans mutant that lives twice as long as wild type. *Nature*. 366:461–464. doi:10.1038/366461a0.

Kenyon, C.J. 2010. The genetics of ageing. *Nature*. 464:504–512. doi:10.1038/nature09047.

Klass, M.R. 1977. Aging in the nematode Caenorhabditis elegans: Major biological and environmental factors influencing life span. *Mech. Ageing Dev.* 6:413–429. doi:10.1016/0047-6374(77)90043-4.

Lewis, J.A., C.H. Wu, H. Berg, and J.H. Levine. 1980. The genetics of levamisole resistance in the nematode Caenorhabditis elegans. *Genetics*. 95:905–928.

Liu, J., B. Zhang, H. Lei, Z. Feng, J. Liu, A.L. Hsu, and X.Z.S. Xu. 2013. Functional aging in the nervous system contributes to age-dependent motor activity decline in C. elegans. *Cell Metab.* 18:392–402. doi:10.1016/j.cmet.2013.08.007.

Lucanic, M., W.T. Plummer, E. Chen, et al.. 2017. Impact of genetic background and experimental reproducibility on identifying chemical compounds with robust longevity effects. *Nat. Commun.* 8:14256. doi:10.1038/ncomms14256.

Ng, J.M.K., I. Gitlin, A.D. Stroock, and G.M. Whitesides. 2002. Components for integrated poly(dimethylsiloxane) microfluidic systems. *Electrophoresis*. 23:3461–3473. doi:10.1002/1522-2683(200210)23:20<3461::AID-ELPS3461>3.0.CO;2-8.

Peliti, M., J.S. Chuang, and S. Shaham. 2013. Directional locomotion of C. elegans in the absence of external stimuli. *PLoS One*. 8:1–11. doi:10.1371/journal.pone.0078535.

Van Raamsdonk, J.M., and S. Hekimi. 2011. FUdR causes a twofold increase in the lifespan of the mitochondrial mutant gas-1. *Mech. Ageing Dev.* 132:519–521. doi:10.1016/j.mad.2011.08.006.

Rankin, C.H. 1991. Interactions between two antagonistic reflexes in the nematode Caenorhabditis elegans. *J. Comp. Physiol. A*. 169:59–67. doi:10.1007/BF00198173.

Rankin, C.H., and B.S. Broster. 1992. Factors affecting habituation and recovery from habituation in the nematode Caenorhabditis elegans. *Behav. Neurosci.* 106:239–49. doi:10.1037/0735-7044.106.2.239.

Rose, J.K. 2001. Analyses of Habituation in Caenorhabditis elegans. *Learn. Mem.* 8:63–69. doi:10.1101/lm.37801.

Ryan, D.A., R.M. Miller, K. Lee, S.J. Neal, K.A. Fagan, P. Sengupta, and D.S. Portman. 2014. Sex, Age, and Hunger Regulate Behavioral Prioritization through Dynamic Modulation of Chemoreceptor Expression. *Curr. Biol.* 24:2509–2517. doi:10.1016/j.cub.2014.09.032.

Santi, D. V, and C.S. Mchenry. 1972. 5-Fluoro-2'-Deoxyuridylate: covalent complex with thymidylate synthetase. *Pnas Usa*. 69:1855–1857.

Segalat, L., D.A. Elkes, and J.M. Kaplan. 1995. Modulation of serotonin-controlled behaviors by G o in Caenorhabditis elegans. *Science (80-.).* 267:1648–1651.

Shtonda, B.B. 2006. Dietary choice behavior in Caenorhabditis elegans. *J. Exp. Biol.* 209:89–102. doi:10.1242/jeb.01955.

Stiernagle, T. 2006. Maintenance of C. elegans. *WormBook*. 1–11. doi:10.1895/wormbook.1.101.1.

Stirman, J.N., M.M. Crane, S.J. Husson, et al., 2011. Real-time multimodal optical control of neurons and muscles in freely behaving Caenorhabditis elegans. *Nat. Methods*. 8:153–8. doi:10.1038/nmeth.1555.

Stroustrup, N., B.E. Ulmschneider, Z.M. Nash, I.F. López-Moyado, J. Apfeld, and W. Fontana. 2013. The Caenorhabditis elegans Lifespan Machine. *Nat. Methods*. 10:665–70. doi:10.1038/nmeth.2475.

Swierczek, N.A., A.C. Giles, C.H. Rankin, and R.A. Kerr. 2011. High-throughput behavioral analysis in C. elegans. *Nat. Methods*. 8:592–598.

Van Swinderen, B., L.B. Metz, L.D. Shebester, J.E. Mendel, P.W. Sternberg, and C.M. Crowder. 2001. Go?? regulates volatile anesthetic action in Caenorhabditis elegans. *Genetics*. 158:643–655.

Tatar, M. 2009. Can we develop genetically tractable models to assess healthspan (rather than life span) in animal models? *Journals Gerontol. - Ser. A Biol. Sci. Med. Sci.* 64:161–163. doi:10.1093/gerona/gln067.

White, D.K., T. Neogi, M.C. Nevitt, C.E. et al., 2012. Trajectories of Gait Speed Predict Mortality in Well-Functioning Older Adults: The Health, Aging and Body Composition Study. *J. Gerontol. A. Biol. Sci. Med. Sci.* 68:1–9. doi:10.1093/gerona/gls197.

Wicks, S.R., and C.H. Rankin. 1995. Integration of mechanosensory stimuli in Caenorhabditis elegans. *J. Neurosci.* 15:2434–2444.

Wilkinson, D.S., R.C. Taylor, and A. Dillin. 2012. Analysis of Aging in Caenorhabditis elegans. 107. Second Edi. Elsevier Inc. 353-381 pp.

Wittenburg, N., and R. Baumeister. 1999. Thermal avoidance in Caenorhabditis elegans: an approach to the study of nociception. *Proc. Natl. Acad. Sci. U. S. A.* 96:10477–10482. doi:10.1073/pnas.96.18.10477.

Zhang, W.B., D.B. Sinha, W.E. Pittman, E. Hvatum, N. Stroustrup, and Z. Pincus. 2016. Extended Twilight among Isogenic C. elegans Causes a Disproportionate Scaling between Lifespan and Health. *Cell Syst.* 3:333–345.e4. doi:10.1016/j.cels.2016.09.003.

3.1.11 Supplementary Material

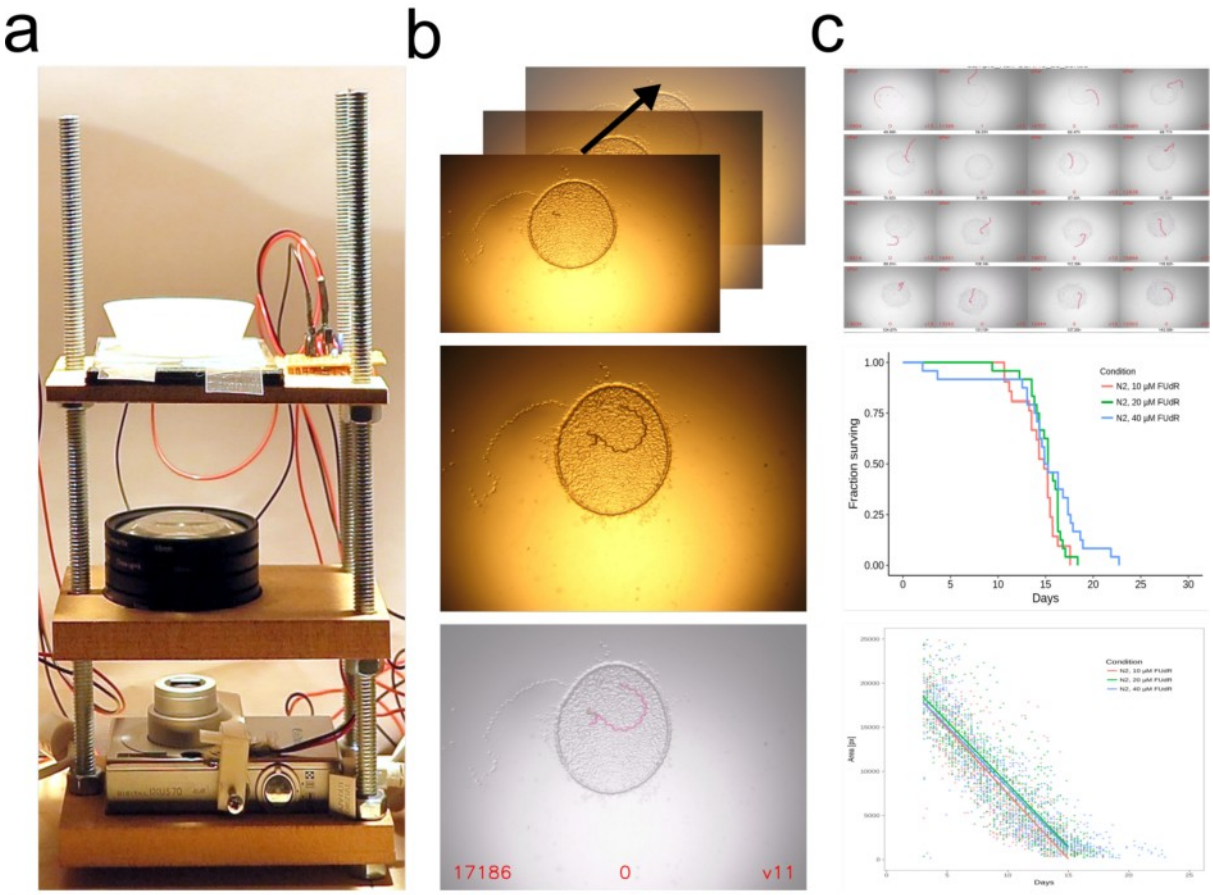

Figure 8: Imaging Platform and Image Processing

Each worm is imaged for 1 min every 6.2 h. Pixel size is 6.5 µm with an effective field of view ranging from 230 to 250 mm^2. Imaging frequency is ~1 s^{-1}. As the robotic plate transfer to the imaging platform variably excites the worms due to an ambient light change and slight vibration, we added a vibration motor to the plate holder to apply a more vigorous stimulus for 5 s. **(a)** The imaging platform consists of the following components: plate holder with vibration motor (top), lens assembly (middle), and a consumer-grade camera (bottom). A diffusor and incandescent halogen light bulb are used for illumination (not shown). **(b)** After image transfer to the host computer, the worm track is extracted: A minimum intensity projection is calculated (top). Adaptive thresholding binarizes the track (middle) which is superimposed onto a grey copy of the first image (bottom). The number of track pixels is counted and written to a file along with other assay parameters. **(c)** Manual inspection and statistical analysis. All track overlays of a single worm are compiled into a mosaic (top), used for identification of falsely thresholded tracks and other artifacts, which are manually annotated to be excluded from statistical analysis. Annotated data is used to extract lifespan data (middle) and to model the decline of motility during ageing using linear-mixed effect models (bottom).

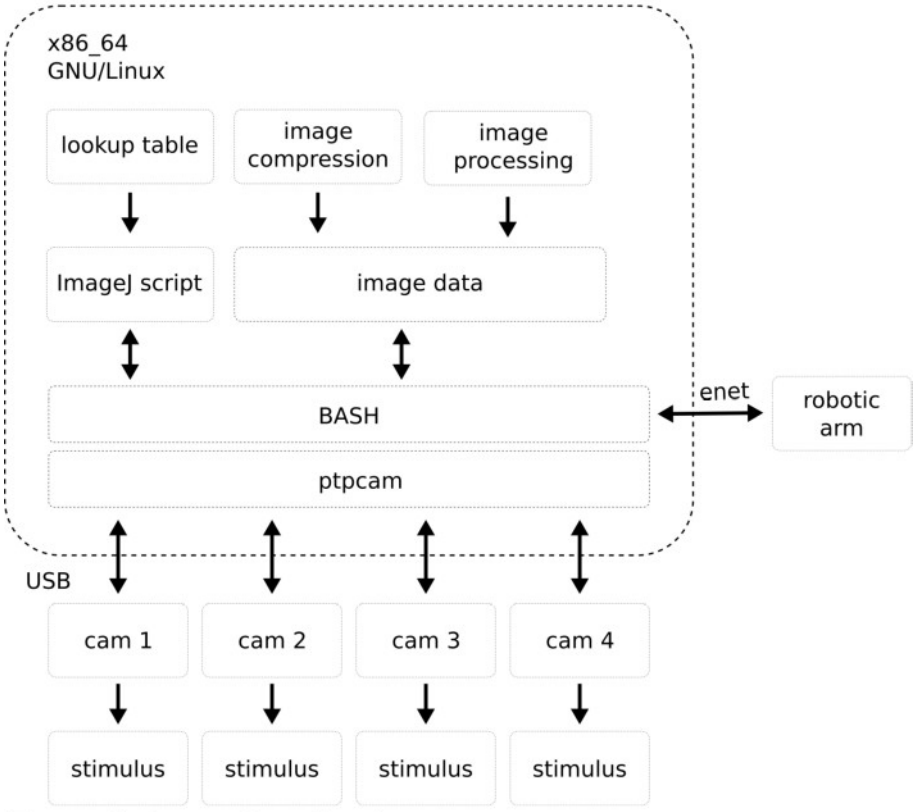

Figure 9: Assay Coordination

A PC is used to control and coordinate the entire assay through an ImageJ script. The script cycles through a sample lookup table in which all plates are entered before the assay is started containing a unique identifier and the date of birth of the given worm. Plates are processed in stacks of four. The ImageJ script initiates macros on the robot controller to pick up a plate from a specified array position and put it on one of the four imaging platforms. A script on the camera is initiated which sets up the imaging parameters, starts taking pictures and switches the vibrational motor at a specific time to deliver a stimulus. After the assay is completed, the images are transferred from camera storage to the host PC to be stored in a directory together with text files containing worm id, date of birth, current time stamp, ambient temperature, and additional parameters of hard- and software. Meanwhile, the robotic arm takes the plate off the imaging platform and puts it back onto the array. Once all four imaging platforms have been cleared, the next stack of plates is processed. A script continuously runs in the background, converting downloaded image series to more compressed movies, while preserving image metadata provided by the camera. Another script extracts track information from compressed movies (Figure 8).

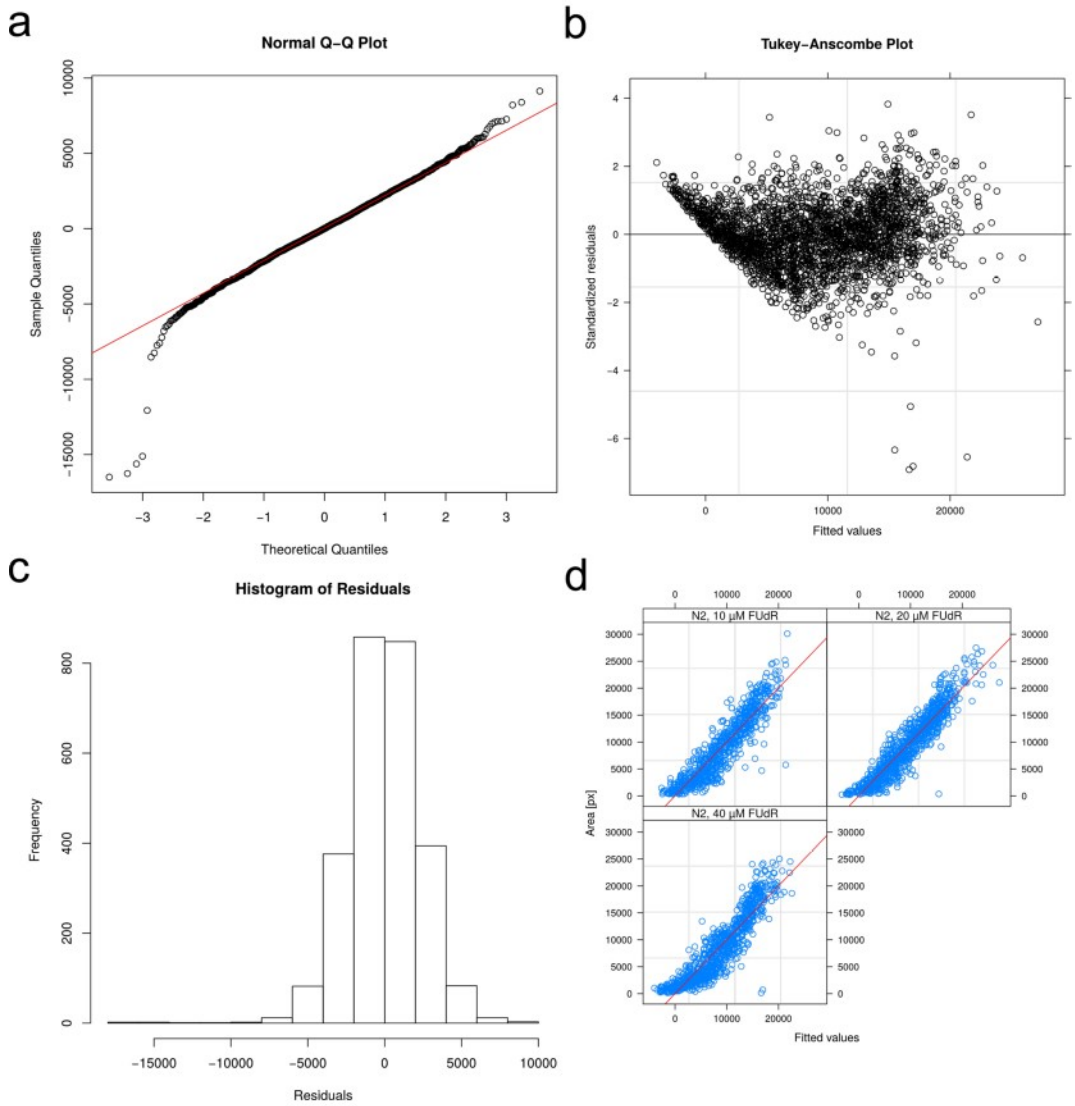

Figure 10: Diagnostic Plots to Validate Wild Type RAPID Data at Various FUdR Concentrations

Wild type worms at different FUdR concentrations. **(a)** Normal Q-Q plot of residuals. **(b)** Tukey-Anscombe plot. **(c)** Histogram of residuals. **(d)** Fitted vs measured.

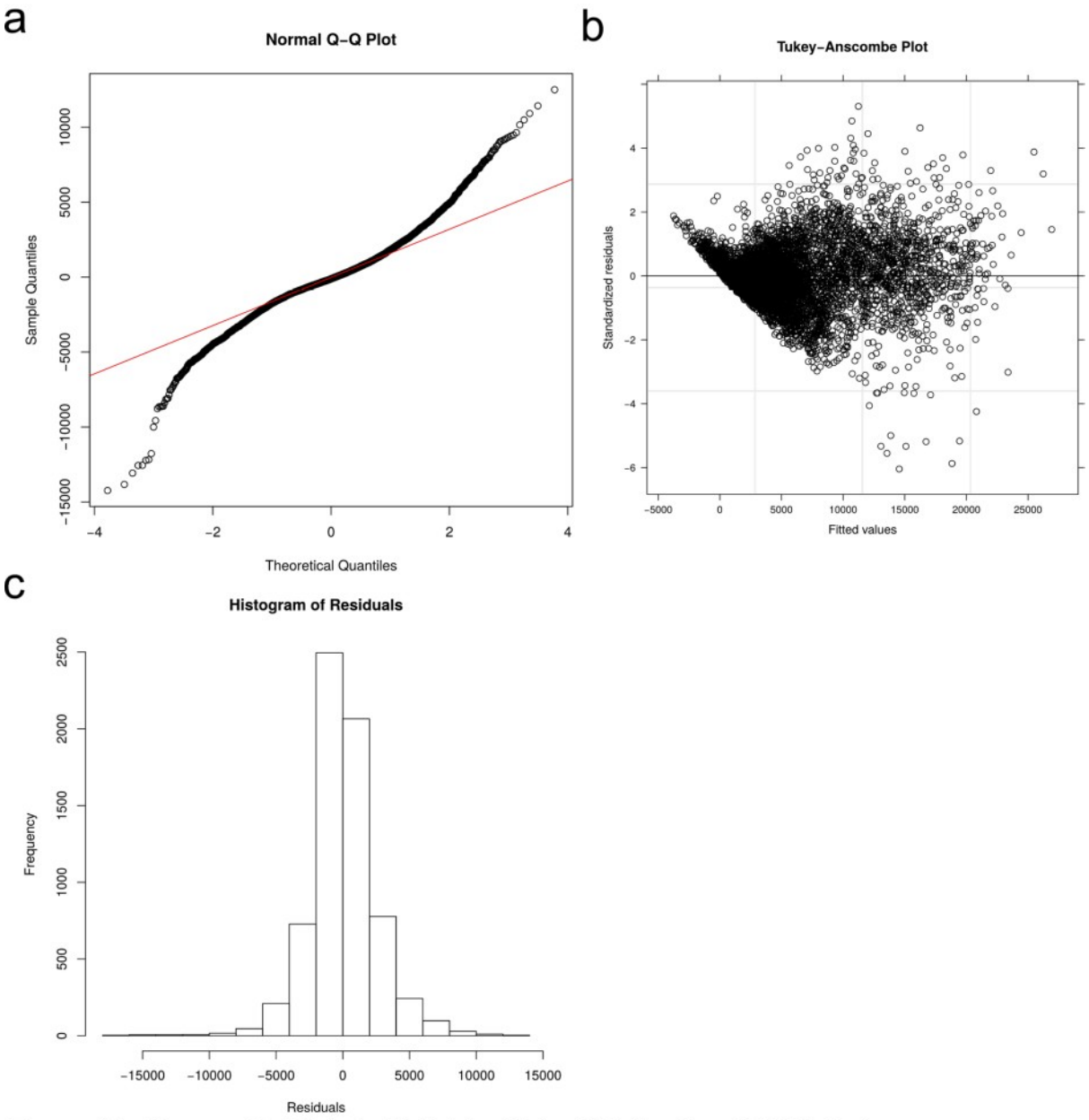

Figure 11: Diagnostic Plots to Validate Mutant Collection RAPID Data

Wild type worms at different FUdR concentrations. **(a)** Normal Q-Q plot of residuals. **(b)** Tukey-Anscombe plot. **(c)** Histogram of residuals. **(d)** Fitted vs measured.

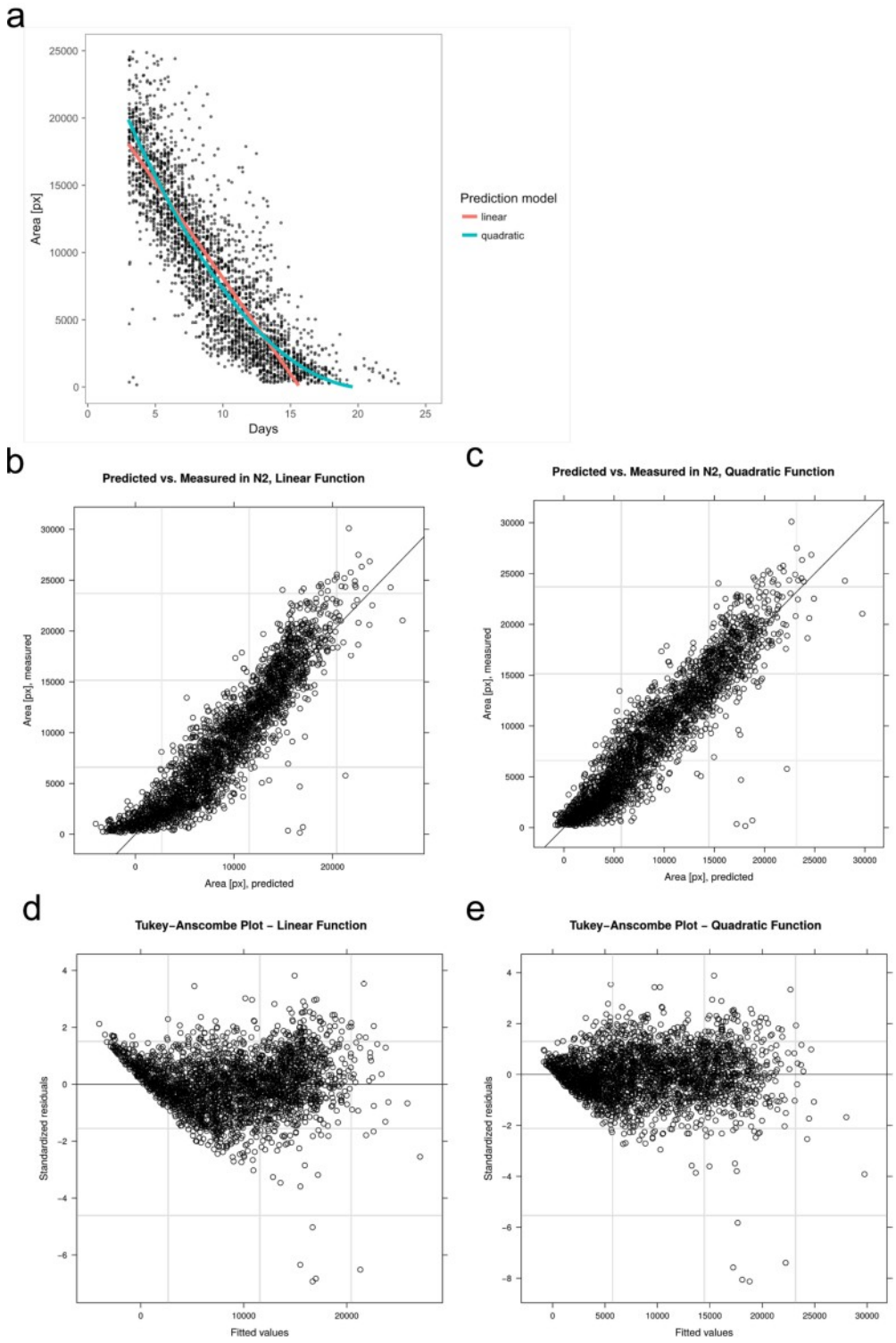

Figure 12: Linear vs. Quadratic Models for Wild Type RAPID Data

Pooled area vs. days data from Figure 5. **(a)** A linear and a quadratic function have been used in a linear-mixed effect model to fit the data. **(b-e)** Diagnostic plots indicate that a quadratic function **(a,d)** fits the data better than a linear function **(c,e)**.

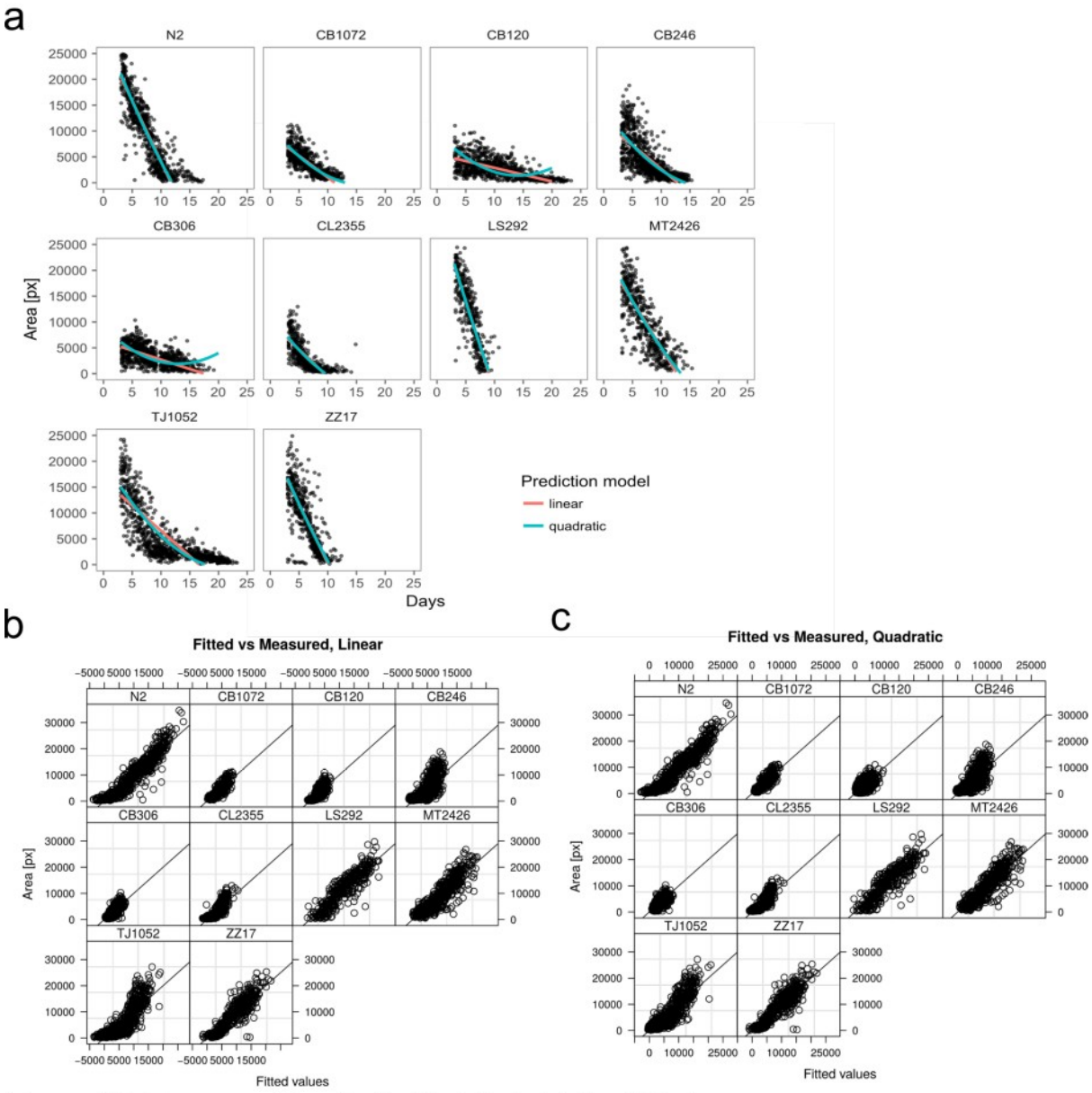

Figure 13: Linear vs. Quadratic Models in Mutant Strains

(a) RAPID data fit with a linear-mixed effect model with a linear (red line) and a quadratic term for time without higher-order interactions (blue line). Quadratic terms appear to be in discordance for the strains CB120 [unc-4(e120) II.] and CB306 [unc-50(e306) III.]. Hence, we fitted a linear function to all strains. **(b,c)** Diagnostic plots for the linear and quadratic functions.

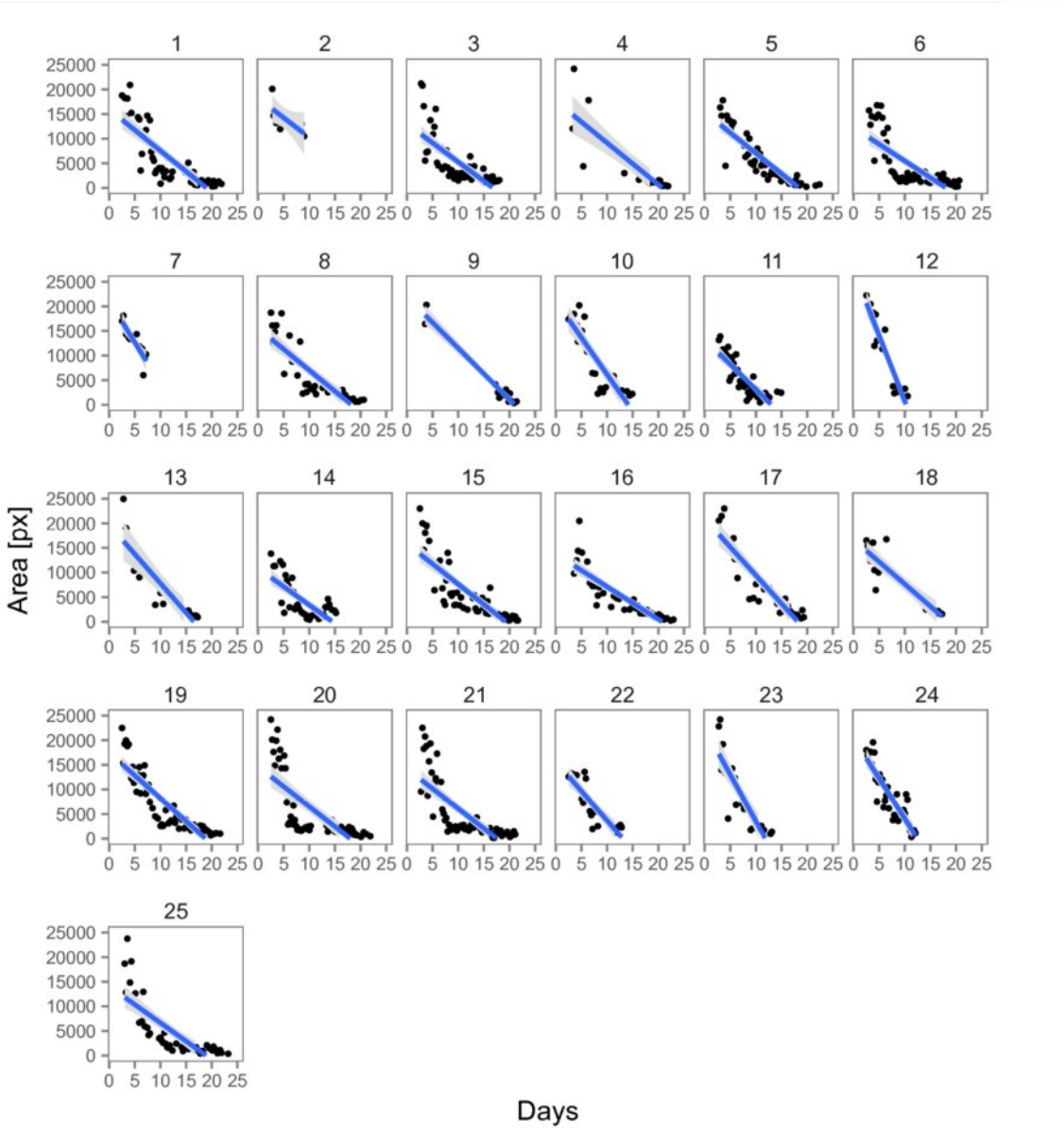

Figure 14: Biphasic Motility Descline in TJ1052 [age-1(hx546) II.]

A rapid decline between day 2 and day 8 is followed by a slow decline in the remaining lifetime.

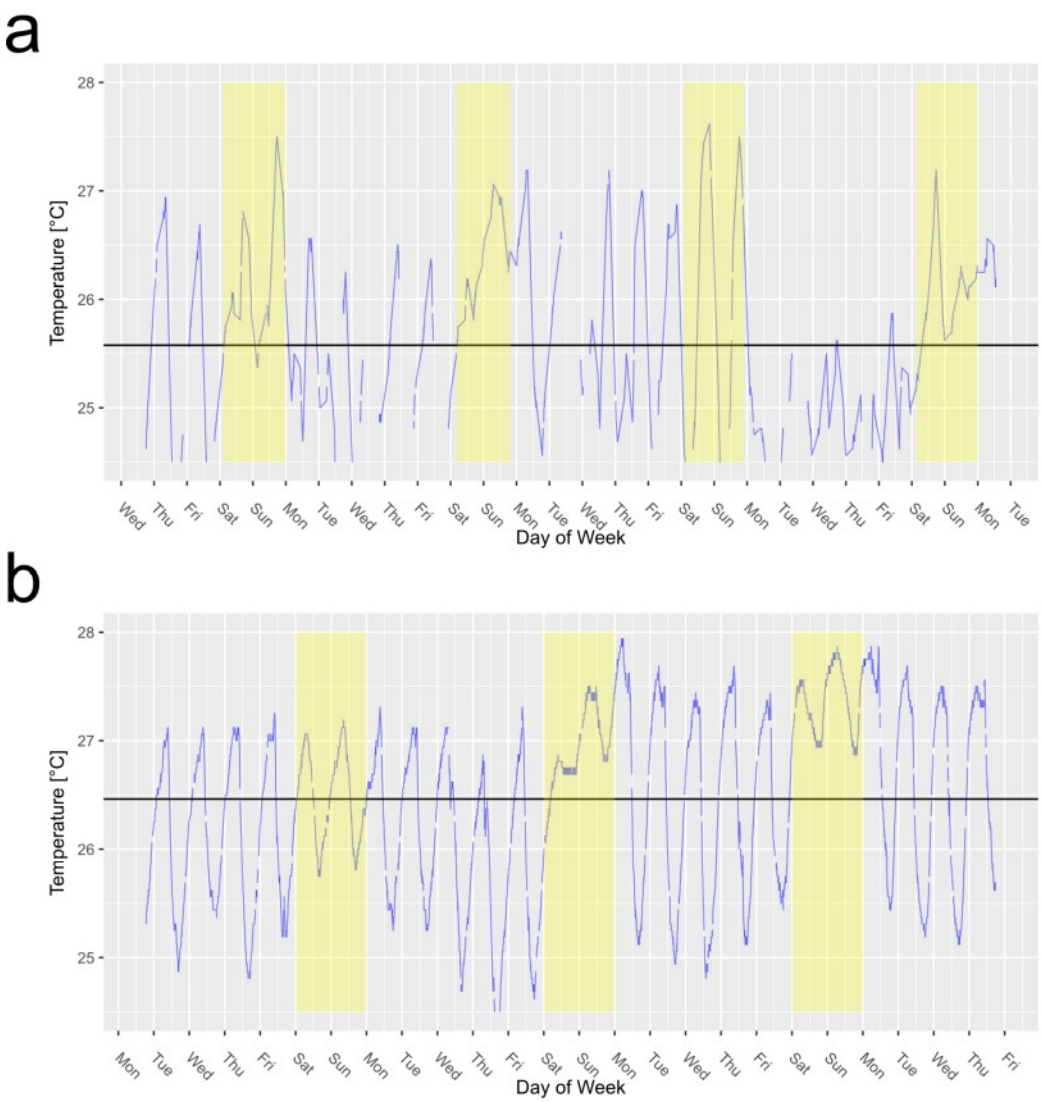

Figure 15: Tempeature Logs During RAPID Assay

Temperature is continuously recorded during the assay (blue dots). **(a)** FUdR in wild type experiment. **(b)** Various worm strains experiment. The plots show fluctuations due to reduced ventilation/air conditioning at night and on weekends (yellow overlay). Mean temperature during the assay was 26.46 °C (black horizontal line).

	Value	Std Error	DF	t value	p value
N2, 10 µM FUdR (Intercept)	12470.38	1621.59	2545	7.69	<0.001
days	-1480.67	63.97	2545	-23.15	<0.002
N2, 20 µM FUdR	451.27	1057.88	65	0.43	0.67
N2, 40 µM FUdR	-242.71	1068.10	65	-0.23	0.82
temperature	383.43	56.11	2545	6.83	<0.001
days:N2, 20 µM FUdR	62.93	86.96	2545	0.72	0.47
days:N2, 40 µM FUdR	94.37	87.73	2545	1.08	0.28

Table 5: Linear Mixed-Effect Model Describes FUdR Effect on Motility

A linear mixed-effect model has been fitted. Pair-wise comparison of 20/40 µg/ml to 10 µg/ml FUdR. The interaction term is not significant, indicating no effect of FUdR concentration on motility over time.

Condition	animals	*rmean	*se(rmean)	median	0.95LCL	0.95UCL
10 µg/ml	21	14.34	0.43	**14.83**	13.52	15.73
20 µg/ml	24	15.13	0.37	**15.25**	14.85	16.28
40 µg/ml	24	14.74	0.82	**15.07**	14.36	17.35

Table 6: Statistical Analysis of Wild Type Survival Data at Different FUdR Concentrations

Median survival is altered by less than a day by different FUdR concentrations. Compare with Kaplan-Meier plots (Fig. 3 a).

strain	animals	*rmean	*se(rmean)	median	0.95LCL	0.95UCL
N2	22	11.47	0.39	**11.10**	10.32	12.40
CB1072	28	9.14	0.34	**9.04**	8.53	10.34
CB120	17	14.16	0.25	**19.39**	17.59	21.97
CB246	28	12.19	0.37	**12.45**	11.69	13.49
CB306	23	13.05	0.41	**13.76**	12.48	15.58
CL2355	26	8.81	0.42	**8.78**	7.87	9.96
LS292	23	7.69	0.18	**7.89**	7.39	8.16
MT2426	22	10.77	0.37	**10.58**	9.94	12.00
TJ1052	25	13.63	0.42	**19.06**	14.94	21.12
ZZ17	24	8.57	0.29	**8.37**	8.23	9.03

Table 7: Summary Statistics of Strain-Specific Lifespan Data

TJ1052 [*age-1(hx546)* II.] and CB120 [*unc-4(e120)* II., *daf-2(sa875)* III.] show an increased lifespan. This is unexpected for *unc-4(e120)* II., see discussion. The mutants CB1072 [*unc-29(e1072)* I.], CL2355 [*smg-1(cc546) dvIs50* I.], LS292 [*dys-1(cx18)* I.], MT2426 [*goa-1(n1134)* I.] and the transgenic strain ZZ17 [*lev-10(x17)* I.] are short-lived.

a

	Value	Std Error	DF	t value	p value
N2, 10 µM FUdR (Intercept)	12470.38	1621.59	2545	7.69	<0.001
days	-1480.67	63.97	2545	-23.15	<0.002
N2, 20 µM FUdR	451.27	1057.88	65	0.43	0.67
N2, 40 µM FUdR	-242.71	1068.09	65	-0.23	0.82
temperature	383.43	56.11	2545	6.83	<0.001
days:N2, 20 µM FUdR	62.93	86.96	2545	0.72	0.47
days:N2, 40 µM FUdR	94.37	87.72	2545	1.08	0.28

b

	Value	Std Error	DF	t value	p value
N2, 10 µM FUdR (Intercept)	18670.61	1563.18	2544	11.94	<0.001
days	-2612.58	77.47	2544	-33.72	<0.001
N2, 20 µM FUdR	704.26	1044.71	65	0.67	0.5
N2, 40 µM FUdR	575.97	1055.48	65	0.55	0.59
days^2	62.52	3.09	2544	20.25	<0.001
temperature	314.22	52.45	2544	5.99	<0.001
days:N2, 20 µM FUdR	24.47	72.40	2544	0.34	0.74
days:N2, 40 µM FUdR	-18.05	73.07	2544	-0.25	0.8

Table 8: Statistical Comparison Between Linear and Quadratic Functions for RAPID Wild Type Data

(a) Linear mixed-effect model fitted with linear function. **(b)** Linear mixed-effect model fitted with quadratic function without higher order interactions. Both models show no significant difference in pair-wise comparison of 20/40 µg/ml with 10 µg/ml FUdR, indicating no effect of FUdR concentration on motility over time.

Task	Est'd. Time	Comment
synchronize worms with drop bleach, depends on number of different strains	5 min	per strain
pour plates	20 min	
seed plates	30 min	drop has to be placed carefully in the centre
single worms	1 h	
label and seal plates	1 h	
setup RAPID	10 min	upload sample table, check cameras, robot, and analysis daemons
place plates on assay table	30 min	
inspect data sets for thresholding artifacts	5 h	

Table 9: Time Required For RAPID Experiment

This table illustrates the "hands on" time for a single lab worker performing a RAPID assay with 280 individual worms.

3.2 Establishing Histology for *C. elegans*

Histology and immunohistological examination has a long-standing and successful history in many fields of biomedical science and most notably in contemporary routine histopathological diagnostics. IHC visualizes epitopes of gene products *in situ,* thereby allowing to detect the presence of a particular epitope in the context of cellular compartments and surrounding tissue.

The use of conventional histopathological procedures on *C. elegans* is hampered by the small size of the organism. Nonetheless, our laboratory introduced robust protocols for *C. elegans* histology on cryostat sections (Hench et al., 2011). To further standardize and facilitate histology and IHC for *C. elegans*, we now successfully adapted a cytological cell block technique (Jain et al., 2014) to worm embedding. Using blood plasma and recombinant thrombin to enmesh the animals in an artificial clot, we create a pseudo-tissue containing 1000s of animals which can subsequently be formalin-fixed and paraffin-embedded (FFPE) using standard procedures, creating so-called worm blocks (Figure 16). Such embedded specimens allow storage at room temperature for years without significant loss of antigenicity (Kokkat et al., 2013), enabling retrospective histochemical comparative evaluation, most prominently by IHC. Morphological details are better preserved in FFPE compared to cryostat sections. Since the worms in a worm block form a pseudo-tissue, they can be handled in the same way as e.g. biopsy tissue, making use of highly automated and standardized histopathology infrastructure.

The use of conventional light absorbing chromogens as well as a permanent mounting medium furthermore allows re-evaluation of archived stained slides. Worms within a worm block are randomly oriented yielding sections through all possible planes at once.

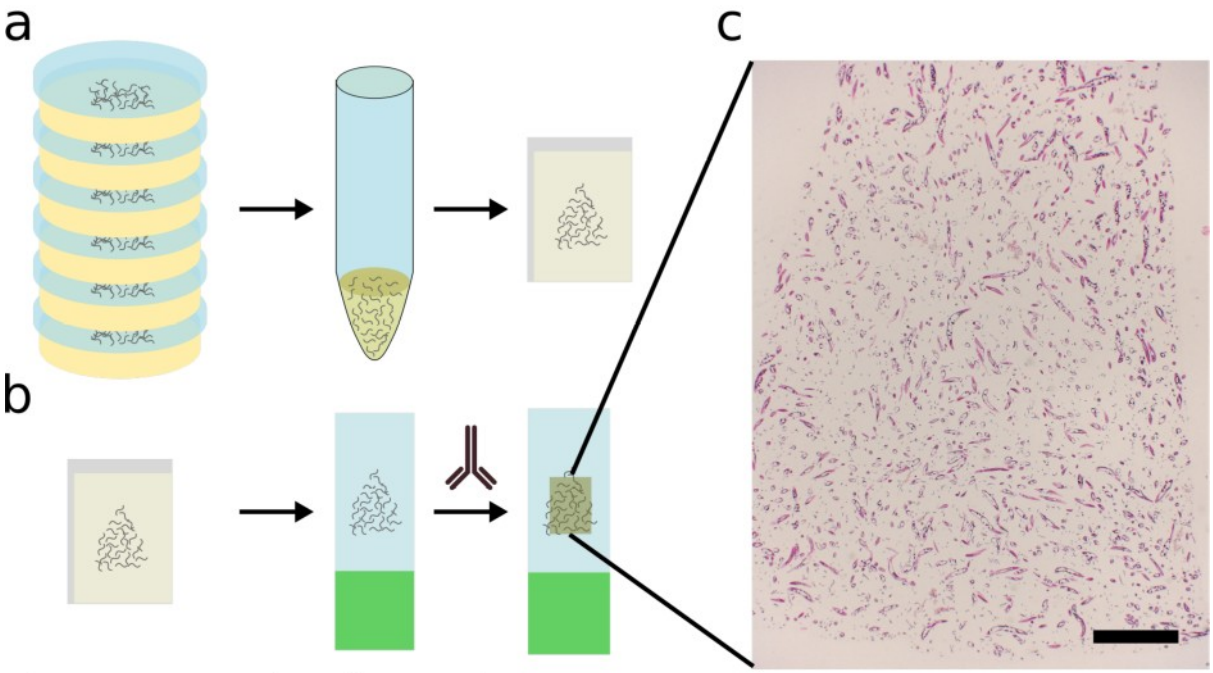

Figure 16: Generation of Worm Blocks

Generation of worm blocks starts by collecting a large number of synchronized worms, formalin fixation, and enmeshing the worms in a blood clot generated from blood plasma and thrombin, which is then fixed in formalin once again. From this point onwards, the specimen is treated like regular, macroscopic tissue, dehydrated and paraffin embedded (a). Once FFPE worm blocks are made, a large number of sections can be cut for histological examinations and stored for years (b). This format is suitable for the vast majority of histopathological labelings, in particular immunohistochemistry as indicated by the stylized antibody. Low magnification overview of an H&E stained paraffin section is shown in (c), scale bar = 1 mm.

Figure 17 shows sections of such a worm block made from wild type (N2) worms three days after synchronization, stained with hematoxylin and eosin. Sections through the pharynx inside the head of the worms as an anatomical landmark were chosen to unambiguously visualize some of the major anatomical structures of the nematode.

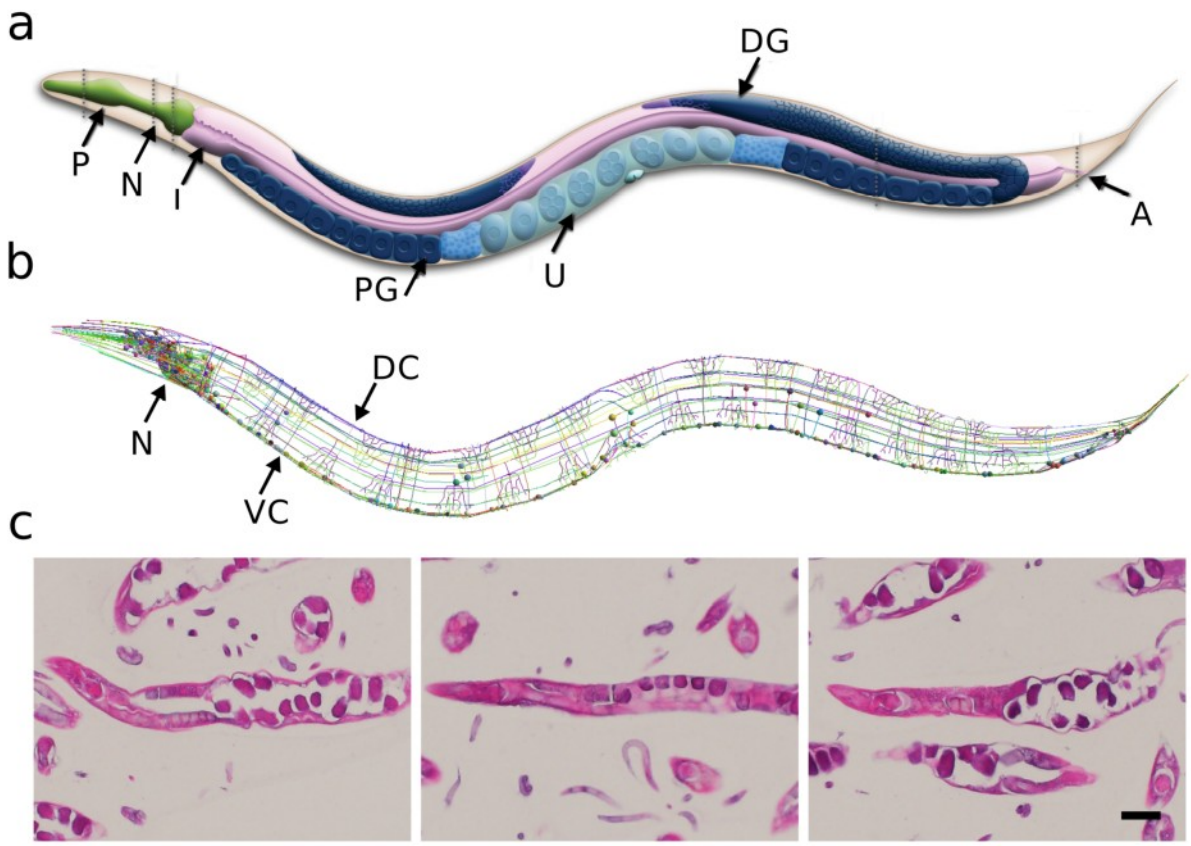

Figure 17: Anatomy of C. elegans and Worm Block Sections

Hematoxylin and eosin stained sections of a worm block made from adult N2 worms, three days after synchronization. Gross anatomy of an adult hermaphrodite (a), P: pharynx (green), N: location of nerve ring and head neurons (not shown), I: intestine (purple), PG: proximal gonad (blue), U: uterus (light blue), DG: distal gonad (blue), A: anus. Not shown are the body wall muscles and the nervous system, modified from http://wormatlas.org. Schematic representation of the 302 neurons and their neurites (b) rendered with neuroConstruct using data from the openWorm project. N: nerve ring and head neurons, VC: ventral nerve cord, DC: dorsal nerve cord. Selected sections through the longitudinal axis including the head (c). Pharynx, head neurons, intestine, and gonads can be readily identified. This orientation will be shown throughout this work. Scale bar = 50 µm.

To establish IHC with anti-hTau antibodies, we generated worm blocks of synchronized cultures of previously published hTau-expressing transgenic worm strains (Table 11 and Figure 18). The antibodies used, their epitope, dilutions and antigen retrieval protocols are listed in Table 10.

Antibody	Clone	Epitope (AA)	Phos.	Retrieval	Dilution
HT7	MN1000	159 - 163	no	CC1 24	1:500
AT8	MN1020	202/205	yes	CC1 24	1:4'000
AT100	MN1060	212/214	yes	CC1 24	1:800

Table 10: Anti-Tau Antibodies and Dilutions

Anti-hTau antibodies and dilutions used in this work unless otherwise indicated. All labellings were performed on an automated IHC slide staining system (Ventana Benchmark XT, Roche, Switzerland). Epitopes are listed in amino acid positions according to hTau (2N4R, wt) as indicated in the manufacturer's data sheets, Phos.: phosphorylation-dependent epitope, Retrieval: antigen retrieval according to the manufacturer's protocol for 24 min using “Cell Conditioning 1” solution (Ventana, Roche, Switzerland).

			Antibodies		
Publication	Strain	Tau Isoform	HT7	AT8	AT100
Kraemer et al.	CK10	hTau(1N4R, V337M)	pan++	pan++	cords+
Miyasaka et al.	FX10646	hTau(0N3R, wt)	single cells	-	-
	FX10519	hTau(0N4R, wt)	single cells	single cells	-
	FX11152	hTau(0N4R, P301L)	single cells	-	-
	FX12012	hTau(0N4R, R406W)	single cells	-	-
Brandt et al.	VH255	hTau(0N3R, wt)	pan++	pan+	cords+
	VH254	hTau(0N3R, PHP)	pan+	-	cords+
	VH420	hTau(0N3R, NP)	-	-	-

Table 11: IHC of Published C. elegans Models of Tauopathies

Tau IHC of some of the published strains discussed in section “C. elegans as Model System for Tauopathies”. Worm blocks of all strains were generated three days after synchronization (1 day old adults). The strains by Kraemer et al. and Brandt et al. express hTau pan-neuronally (Brandt et al., 2009; Kraemer et al., 2003), while strains of Miyasaka et al. express hTau primarily in the six touch neurons (Miyasaka et al., 2005). The transgenes created by Brandt et al. are not genomically integrated (Brandt et al., 2009). PHP: pseudo hyper phosphorylated hTau, NP: non-phosphorylated hTau. The labeling distribution and intensity was evaluated in a blinded fashion with respect to genotype and semi quantitatively described by two observers using the following abbreviations: pan = pan-neuronal, cords = ventral or dorsal nerve cords without apparent labelling of somata, with the modifier ++ indicating a stronger labelling over +, single cells = sparse labelling of individual neurons only.

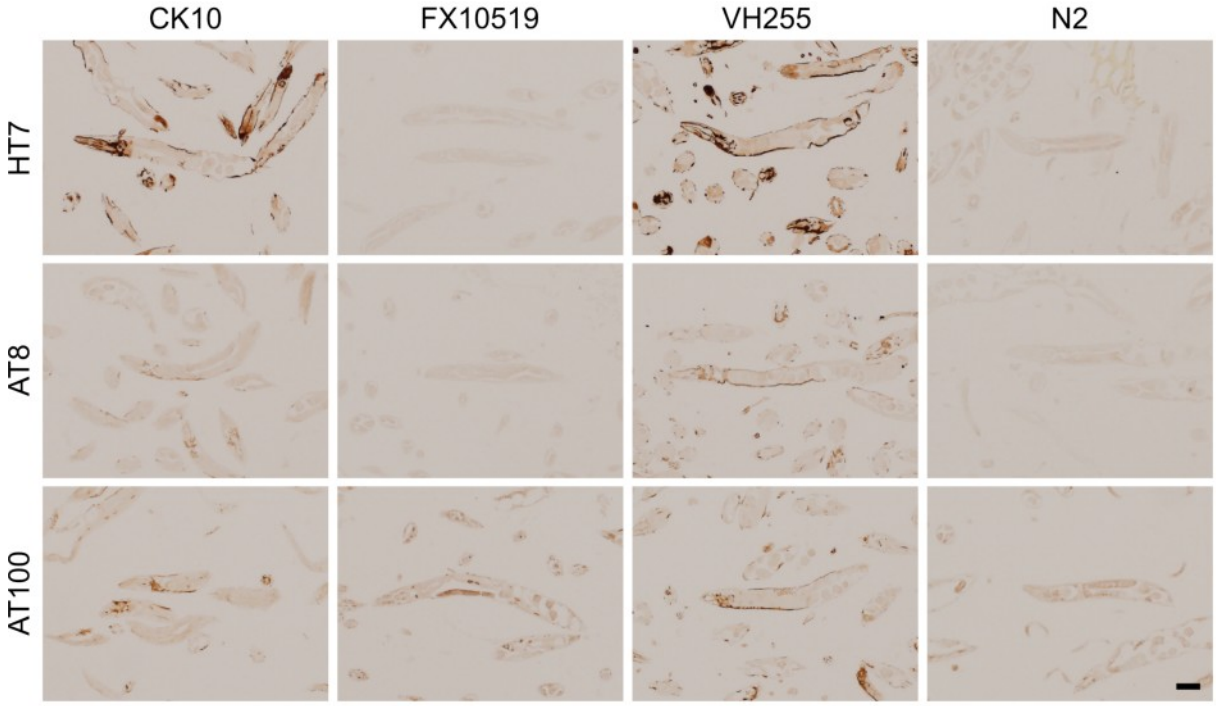

Figure 18: IHC on Published C. elegans Models of Tauopathies

Tau IHC of adult worms, three days after synchronization using phosphorylation-independent antibody HT7 (top row), and phosphorylation-dependent antibodies AT8 (middle row) and AT100 (bottom row). Longitudinal sections through the head were selected to demonstrate the extent of hTau labelling, wild type (N2) was used as negative control. Strains are described in Table 11. Scale bar = 50 µm for all images (bottom right). The strain FX10519 (Miyasaka et al., 2005) expresses hTau mainly in the six touch neurons, whose somata are not located within the head ganglia and therefore not visible in the sections presented.

One of the defining histopathological hallmarks of tauopathies is aggregated tau, which can be demonstrated with Gallyas silver impregnation. Figure 19 shows Gallyas silver impregnation of one of the published strains.

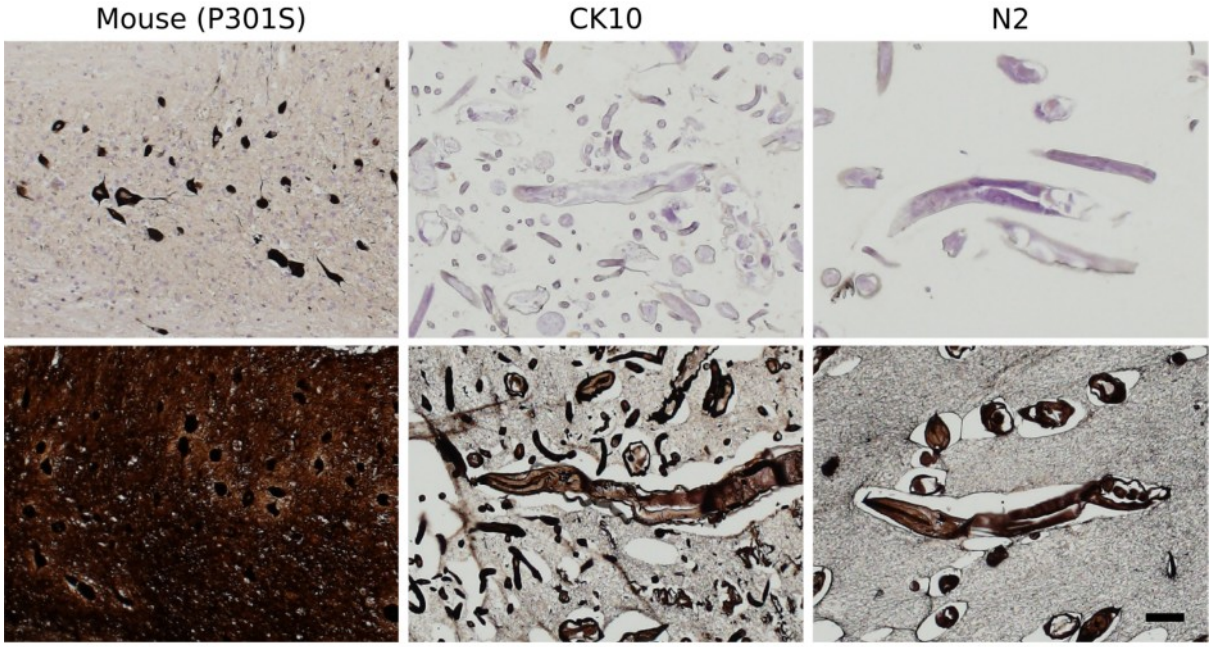

Figure 19: Gallyas Silver Impregnation on C. elegans

Automated Gallyas silver impregnation to demonstrate fibrillary hTau aggregates, a pathological hallmark of tauopathies. Mouse (P301S): sagittal section through brain stem of a 6 month old hTau (0N4R, P301S) expressing mouse (positive control), CK10 (Kraemer et al., 2003) mixed population of hTau (1N4R, V337M) expressing worms, N2: mixed population of wild type worms (negative control). Top row: incubation time optimized for positive control, bottom row: prolonged incubation time. Note that even the fibrin clot from the worm block has accumulated metallic silver. Scale bar = 50 µm for all images (bottom right).

3.3 Modelling Tauopathy in *C. elegans*

3.3.1 Replication of a Published Model

Since one of the reported models showed progressive paralysis, insoluble tau aggregation and structural alterations indicating neurodegeneration (Kraemer et al., 2003), we replicated the hTau construct used in this study to generate independent hTau lines and assess their locomotor performance using RAPID. We generated six lines expressing hTau (1N4R, wt), four lines expressing hTau (1N4R, P301S), and 14 lines expressing hTau (1N4R, V337M). Expression is driven by the promoter region 1.3 kb upstream of *aex-3* and 2.2 kb downstream of *unc-86* was inserted to serve as three prime untranslated region (3'-UTR). After backcrossing the integrated lines with N2, all lines were crossed with the strain SS104 carrying the *glp-4*(*bn2*) allele, rendering the worms sterile at assay conditions (> 25 °C). In addition, the strain CK10 (Kraemer et al., 2003) was crossed with SS104 resulting in the strain IFP134. This strain served as positive control in all IHC experiments. We created worm blocks of synchronized populations to check the expression and phosphorylation status of hTau in all our lines. The IHC results from adult worms grown for three days after synchronization are listed in Table 12.

		Antibodies		
Genotype	Strain	HT7	AT8	AT100
Positive Control	IFP134	pan++	cords+	cords+
Negative Control	SS104	-	-	-
hTau (1N4R, wt)	IFP141	pan++	pan+	-
	IFP142	pan++	pan+	-
	IFP144	pan++	pan+	-
	IFP148	pan+	single cells	-
	IFP224	pan++	single cells	few cords
	IFP225	pan++	single cells	few cords
hTau (1N4R, P301S)	IFP195	single cells	-	-
	IFP199	single cells	-	-
	IFP222	single cells	-	-
	IFP223	-	-	-
hTau (1N4R, V337M)	IFP187	pan+	single cells	-
	IFP191	pan++	pan+	-
	IFP196	pan+	single cells	-
	IFP197	pan++	single cells	-
	IFP200	pan++	single cells	-
	IFP208	single cells	-	-
	IFP211	pan+	-	-
	IFP212	pan+	single cells	-
	IFP213	pan+	-	-
	IFP214	single cells	-	-
	IFP217	pan++	pan+	-

		Antibodies		
Genotype	Strain	HT7	AT8	AT100
hTau (1N4R, V337M)	IFP218	pan++	pan+	-
	IFP220	pan+	single cells	-

Table 12: IHC on Generated Strains

Three day old worms (day 0 = day of synchronization) from synchronized worm cultures were formalin-fixed and paraffin-embedded for subsequent histology. The phosphorylation-independent antibody HT7 was used to assess the expression of total hTau as well as phosphorylation-dependent antibodies AT8 and AT100 to check the phosphorylation status of hTau as indicated in Table 10. Strain SS104 served as negative control while IFP134, a cross of CK10 (Kraemer et al., 2003) with SS104, served as positive control in all IHC experiments. The labelling distribution and intensity was evaluated blind to the genotype and semi quantitatively described using the following abbreviations: pan = pan-neuronal, cords = ventral or dorsal nerve cords without apparent labelling of somata with the modifier ++ indicating a stronger labelling over +, single cells = only sparse labelling of individual neurons, see Figure 20 for examples of labelling intensities and Figure 21 for representative examples of each genotype.

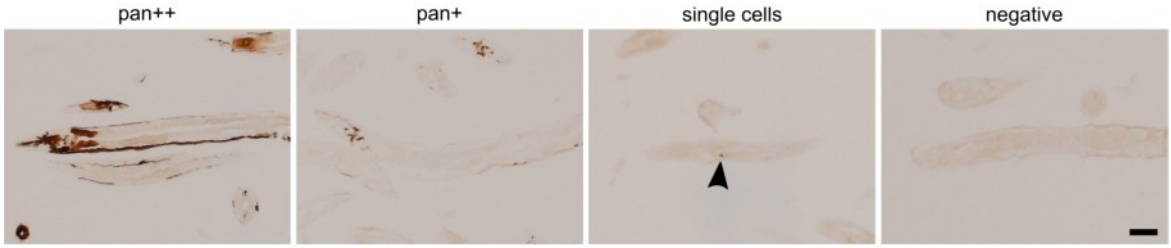

Figure 20: IHC Labelling Quantification

Labelling intensities demonstrated with HT7 IHC. The strains shown are IFP134 (pan++), IFP187 (pan+), IFP195 (single cells), and SS104 (negaitve). Pan++, pan+, and negative show sections through the pharynx to demonstrate labelling of the nerve ring, ventral and dorsal nerve cords recorded using the same exposure settings. The image “single cells” was recorded using a longer exposure and does not show the pharynx, arrow head points at the single positive cell. Scale bar = 50 µm for all images (bottom right).

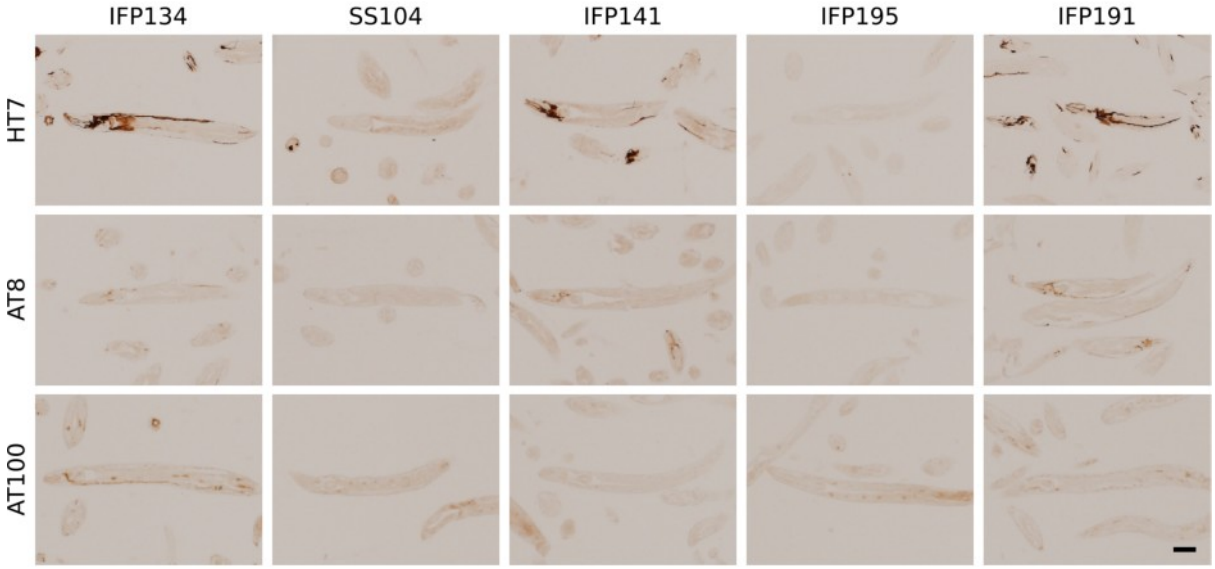

Figure 21: IHC of Selected Strains

Tau IHC of selected strains summarized in Table 12. Sections through the pharynx were chosen to demonstrate labelling of the nerve ring, ventral and dorsal nerve cords; heads are oriented to the left. Exposure and scale are the same for all images, scale bar = 50 µm (bottom right).

3.3.2 Longitudinally Measuring Stimulated Locomotor Performance of hTau-Expressing Strains Using RAPID

An often reported phenotype in hTau-expressing worm strains is uncoordinated locomotion. In order to objectively measure the lifelong locomotor performance of our newly generated hTau strains, we employed our Robot-Assisted Plate Imaging Device (RAPID) described in section “Manuscript: RAPID - High-throughput standardized health modelling in C. elegans”. Figure 22 shows an overview of all measured strains.

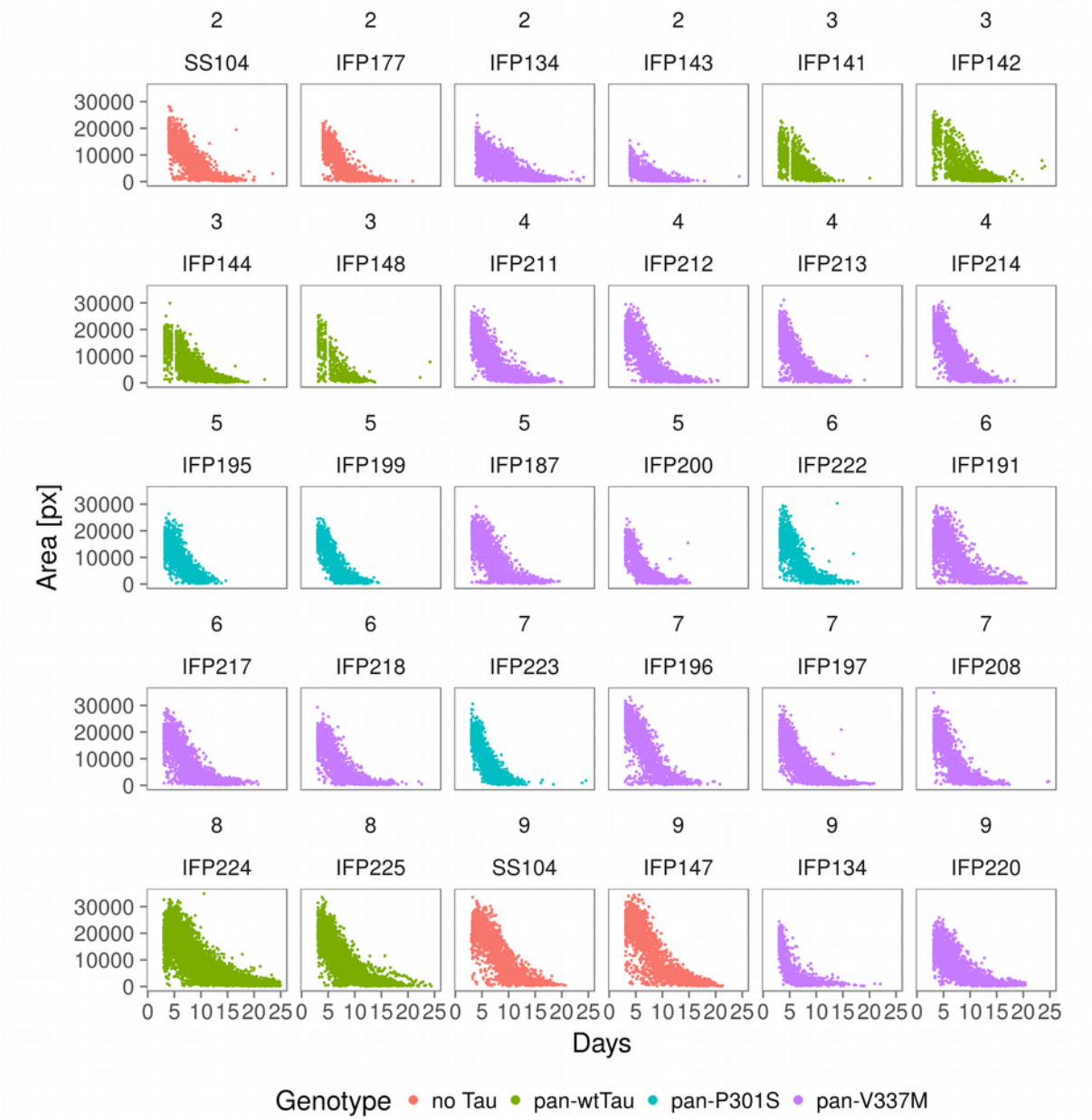

Figure 22: Strains Recorded Using RAPID

Plots of area [px] vs. chronological age [days] of all strains grouped by strain name and run (numbers above strain name, 2-9), recorded using RAPID. Runs 2-7 and 9 consisted of four strains with 70 worms per strain, while run 8 consisted of two strains with 140 worms each. Due to a technical failure during the recording of set 3, data between day 4 and 5 are missing. Colour indicates the hTau construct / genotype. The full list of genotypes can be found in Table 24. Table 13 summarizes the number of worms per strain per run shown in Figure 22.

	Run No.	Strain	Number of Worms	Mean Temperature [°C]
	2	IFP134	65	26.56
		IFP143	65	26.61
		IFP177	69	26.61
		SS104	68	26.6
	3	IFP141	68	26.58
		IFP142	67	26.56
		IFP144	70	26.53
		IFP148	58	26.59
	4	IFP211	65	26.86
		IFP212	63	26.87
		IFP213	65	26.88
		IFP214	70	26.89
	5	IFP187	64	26.6
		IFP195	69	26.65
		IFP199	69	26.62
		IFP200	57	26.63
	6	IFP191	67	26.59
		IFP217	69	26.58
		IFP218	64	26.59
		IFP222	67	26.57
	7	IFP196	58	26.48
		IFP197	66	26.54
		IFP208	69	26.4
		IFP223	69	26.36
	8	IFP224	138	26
		IFP225	134	26.09
	9	IFP134	67	25.53
		IFP147	62	25.62
		IFP220	63	25.64
		SS104	69	25.65
Sum	8	28	2114	

Table 13: Strains Recorded Using RAPID

Summary of the number of worms assessed per strain per run. Sum indicates the number of runs, number of unique strains and number of worms. Worms which were censored are excluded from this list. Mean temperature indicates the mean temperature of all non-zero measurements for each given strain.

The strains SS104 and IFP134 were assessed in duplicate. Strains having a unique genotype (IFP134, IFP143, IFP147 and IFP177) were excluded from the analysis, see section “Generation of Transgenic C. elegans“. RAPID data were arranged by genotype (Figure 23) and all strains with the same genotype can be combined (Figure 24).

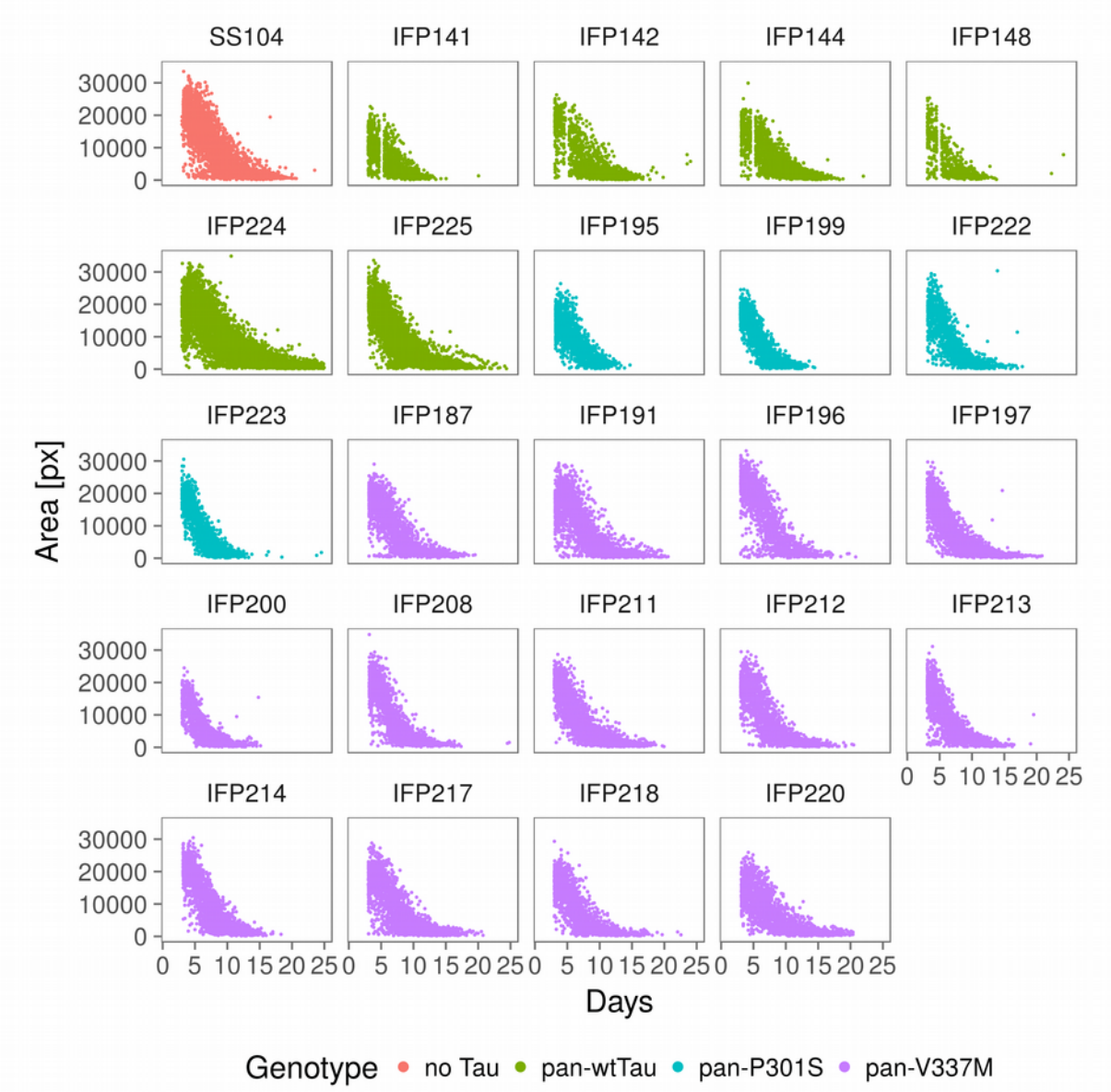

Figure 23: Selected Strains Recorded Using RAPID

Same plots as in Figure 22 but limited to the strains included in statistical analysis, ordered by genotype. See Table 24 for complete list of genotypes and alleles.

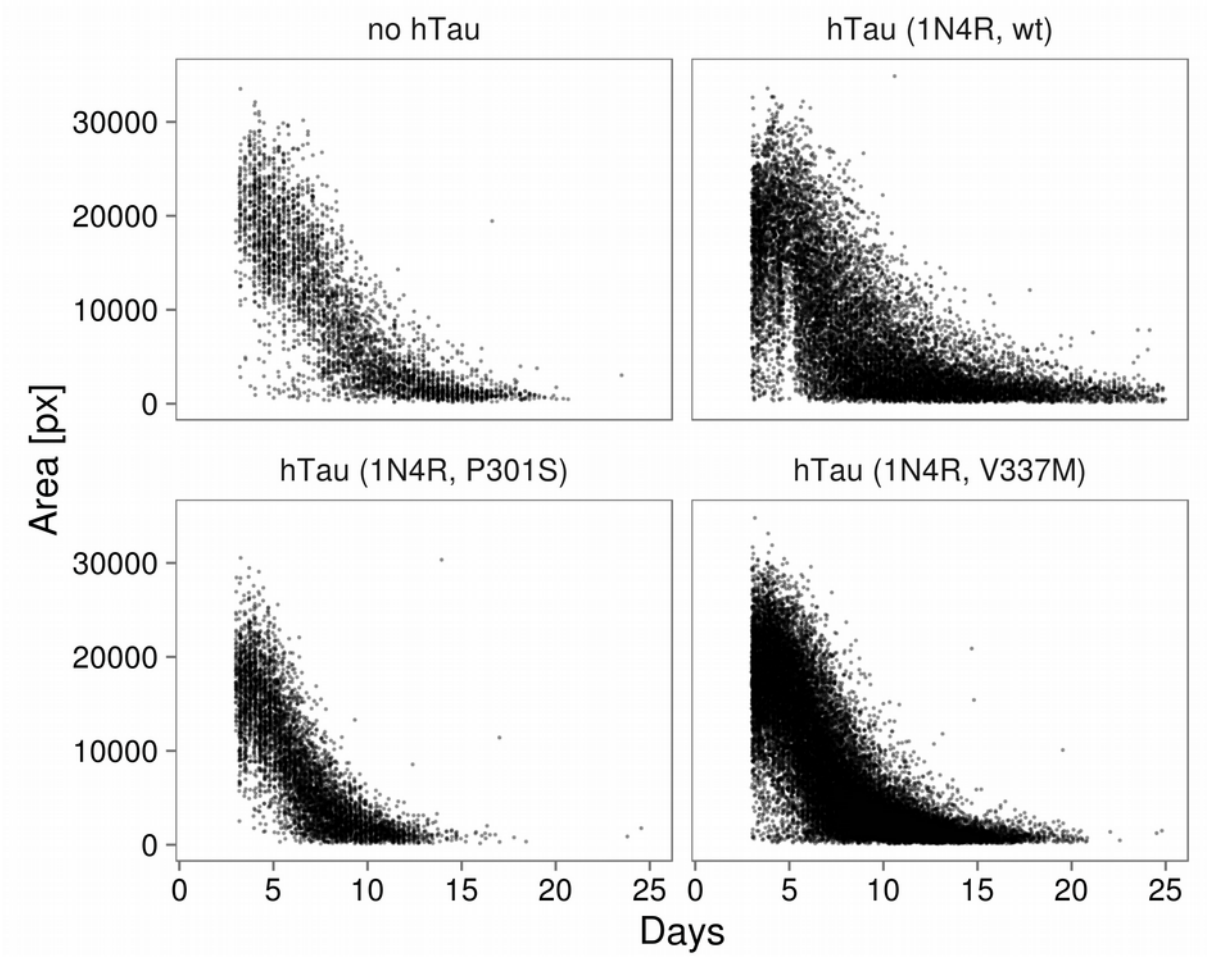

Figure 24: Selected Strains Recorded Using RAPID Combined According to hTau Genotype

Area vs. age plots, all strains of a given genotype are combined, see Figure 23 and Table 12 for list of strains and genotypes.

Although all strains of the same hTau genotype were generated in the same way using the same DNA construct for injection, IHC revealed varying expression of hTau. Figure 25 shows the strains arranged according to hTau expression level as listed in Table 12.

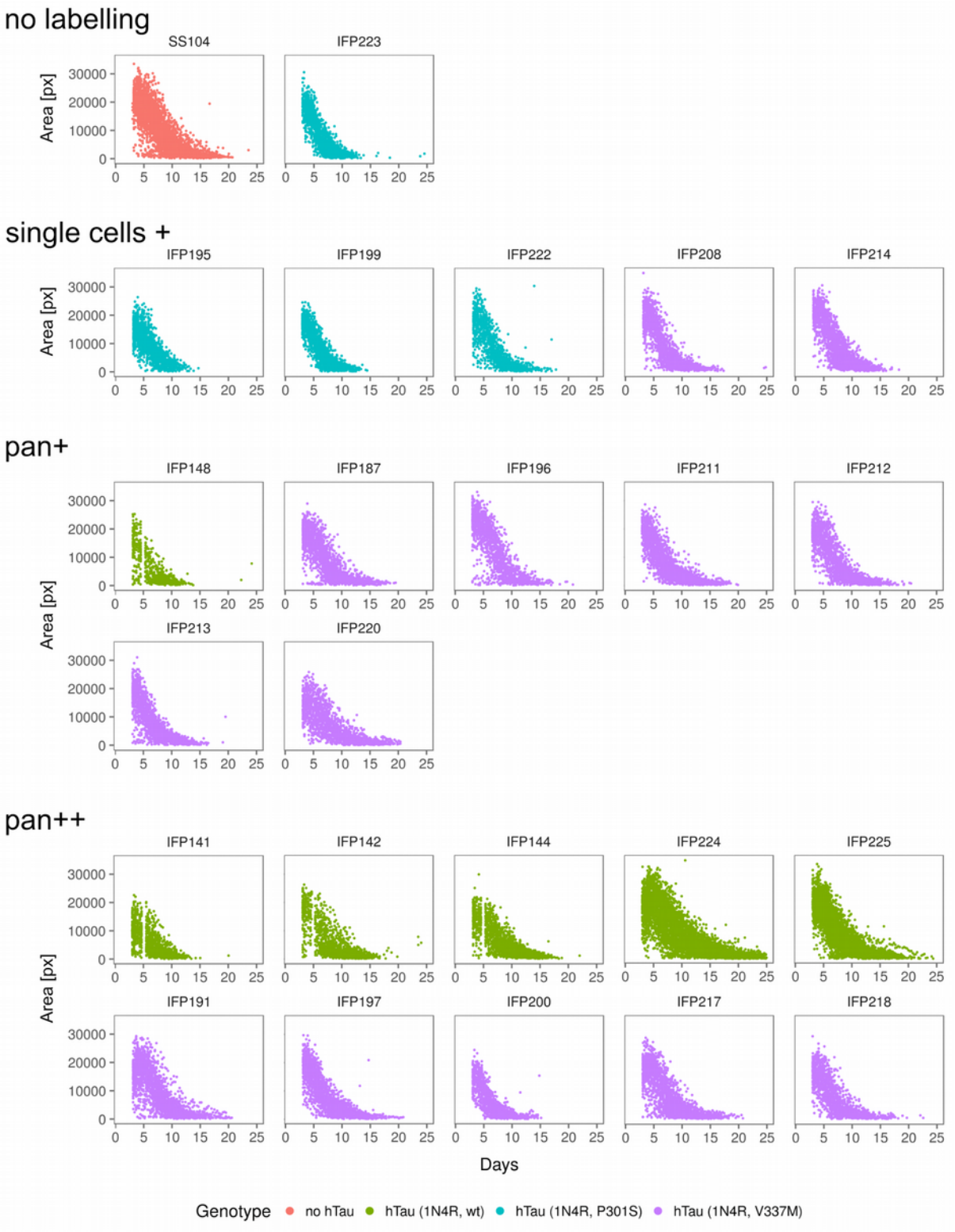

Figure 25: Strains Recorded Using RAPID Arranged by hTau Labelling

Area vs. age of hTau expressing strains, ordered according to hTau labelling using IHC with HT7 as listed in Table 12. Full list of genotypes can be found in Table 24.

Comparing the Effect of hTau Genotype on Stimulated Locomotor Performance

The effect of hTau genotype on locomotor performance was assessed using linear mixed-effect models as established in section “Manuscript: RAPID - High-throughput standardized health modelling in C. elegans”. Linear mixed-effect models are similar to multiple regression models. Coefficients of several predictor variables are estimated to best fit the observed measurements while taking the hierarchical structure of the data, i.e. longitudinal measurements, into account. The coefficients of those predictor variables are called the fixed effects. The predictors are *age*, *genotype*, and *temperature* during the measurement and the dependent variable is *area*. In order to test the effect of the predictor or fixed effect *genotype*, we constructed the following model:

$$area \sim age + age:genotype + genotype + age^2 + temperature \quad (1)$$

In equation (1), *area* is predicted by the coefficients of the fixed effects on the right hand side which are: *age*, the slope of the reference *genotype*, the interaction *age:genotype* describes relative changes in slope for a given genotype, and *genotype*, relative changes in the intercept for a given genotype. Furthermore, there are *genotype*-independent fixed effects: a quadratic term for age^2 and *temperature* indicates changes in *area* for a given temperature during the measurement.

Since individual strains are only a sample of all infinite, theoretically possible strains of a given genotype, they were included as random effects, nested in genotype, nested in runs, with random slopes and random intercepts per worm (section “Statistical Evaluation of RAPID Data” for full model descriptions). The predictions of this model are shown in Figure 26 and the estimated fixed effects of the model are listed in Table 14.

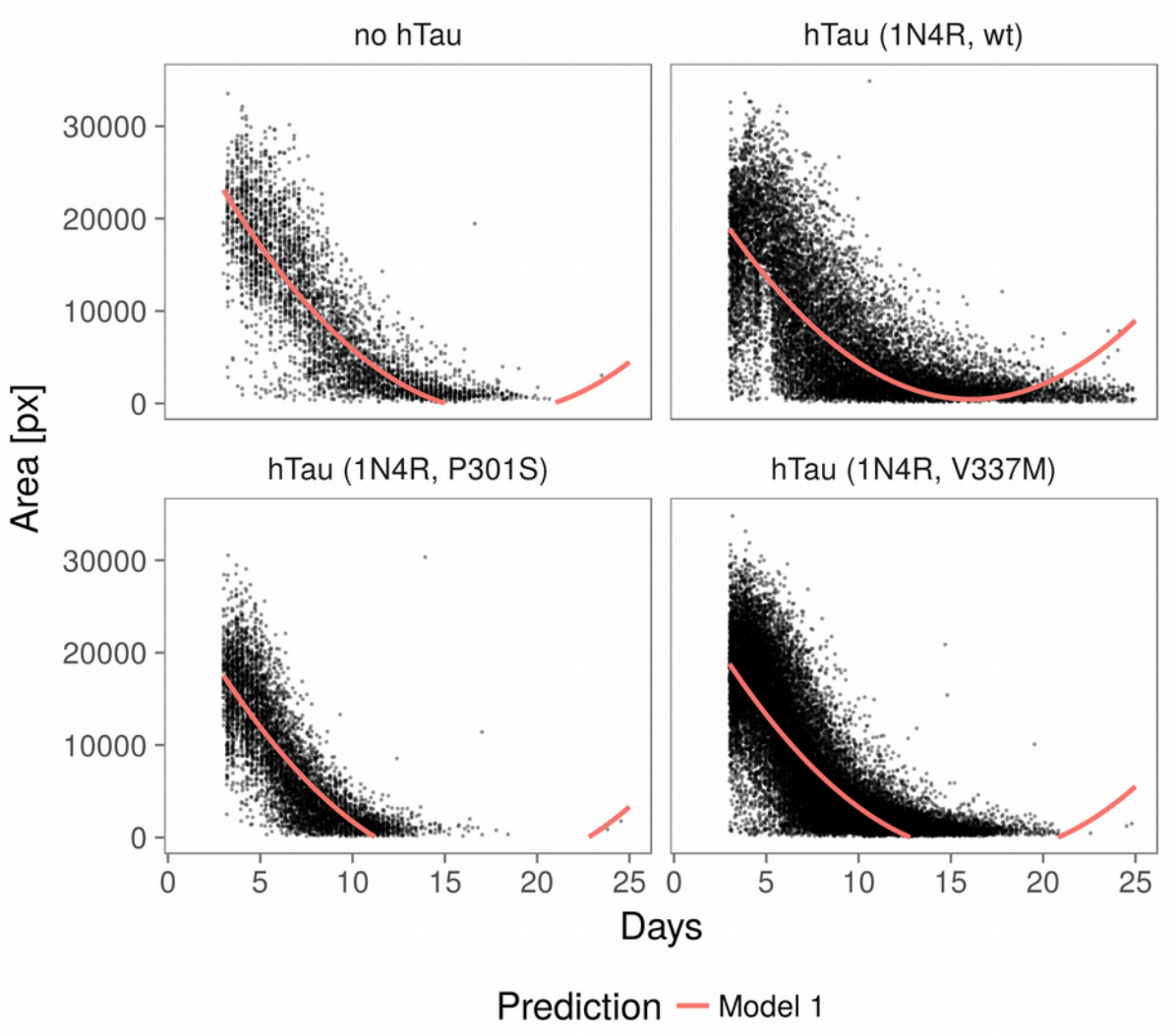

Figure 26: Predictions of Model 1

A linear mixed-effect model was fitted to determine the effect of *genotype* on locomotor performance. The data of all strains with a common genotype are pooled and shown as one plot to illustrate what was fitted. The line shows the prediction for each genotype. The strain SS104 with the *genotype* “no Tau” (top left) was used as reference to which the other genotypes are compared. The estimated fixed effects for the model are listed in Table 14.

Fixed Effect [per Unit]	Area [px]	Std. Error [px]	p-value
no Tau	28169	2837	<0.001
hTau (1N4R, wt)	-5371	3716	0.199
hTau (1N4R, P301S)	-6134	3360	0.088
hTau (1N4R, V337M)	-5023	2985	0.113
temperature [°C]	210	16	<0.001
age [day]	-3860	205	<0.001
age [day^2]	108	1	<0.001
age:hTau (1N4R, wt) [day]	395	262	0.132
age:hTau (1N4R, P301S) [day]	199	247	0.42
age:hTau (1N4R, V337M) [day]	243	218	0.265

Table 14: Estimated Fixed Effects of Model 1

Fitted fixed effects of the model described by equation (1). Fixed effects for *age* and the interaction *age:genotype* are indicated as changes per day, *temperature* is indicated as change in *area* per 1 °C, while fixed effects without unit indicate a change in intercept. The reference strain is SS104 with *genotype* “no Tau”. The p-value indicates the probability of obtaining the coefficient as listed, under the assumption that the fixed effect does not predict the outcome.

Comparing the Effect of Tau Expression Levels on Stimulated Locomotor Performance

In order to test the effect of hTau expression levels on locomotor performance, we constructed a linear mixed effect model which contains a fixed effect for labelling of hTau using anti-hTau antibody HT7 and IHC, according to equation (2).

$$area \sim age + age:labelling + labelling + age^2 + genotype + temperature \quad (2)$$

Since the evaluation of IHC labelling as listed in Table 12 was performed semi-quantitatively, the distinction between pan+ and pan++ is ambiguous. Therefore, the labelling was grouped into “tau positive” or labelling (i.e. pan+ and pan++) and "tau negative" or no labelling (i.e. single cells and no labelling).

Again, the coefficients of the right hand side of equation (2) are the fixed effects which are fitted to predict the *area* on a given *age* (in days). The fixed effect *age*, is the slope of the reference SS104 (“no Tau”, “no labelling”). If labelling is detected, the interaction *age:labelling* describes relative changes in slope, and *labelling* indicates relative changes in intercept. The amount of change in slope per day^2 is given by *age^2*, and *temperature* indicates changes in *area* for a given temperature during the measurement.

The predictions of this model are shown in Figure 27 and the estimated fixed effects of the model are listed in Table 15.

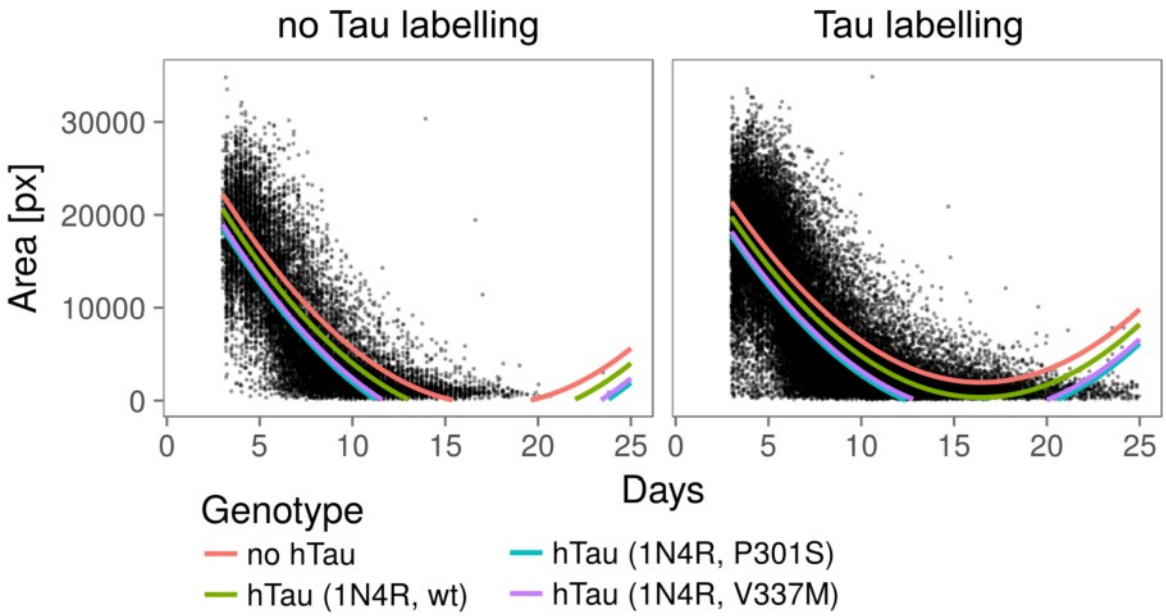

Figure 27: Predictions of Model 2

A linear mixed-effect model was fitted to determine the effect of hTau expression on locomotor performance as determined by HT7 IHC. Predictions of the linear model (2) are shown to illustrate what the model fits. The plot “no Tau labelling” on the left side shows pooled data of all strains in which no or only single cells were detected with HT7 anti-hTau antibody, while the plot “Tau labelling” on the right side shows pooled data from all strains in which HT7 was pan-neuronally detected according to the Table 12. Line colours indicate *genotype* as listed in the legend. The fitted coefficients for the model are listed in Table 15. Note: all theoretically possible combinations of *labelling* and *genotype* are shown even if they did not occur experimentally.

Fixed Effect [per Unit]	Area [px]	Std. Error [px]	p-value
no Tau, no labelling	27010	1752	<0.001
labelling	-1479	1570	0.362
hTau (1N4R, wt)	-1615	1558	0.34
hTau (1N4R, P301S)	-3692	1200	0.008
hTau (1N4R, V337M)	-3239	1336	0.029
temperature [°C]	210	16	<0.001
age [day]	-3768	102	<0.001
age [day^2]	108	1	<0.001
age:labelling [day]	228	101	0.025

Table 15: Estimated Fixed Effects of Model 2

Fitted fixed effects of the model described in equation (2). Fixed effects for *age* and the interaction *age:labelling* are indicated as changes per day, *temperature* is indicated as change in area per 1 °C, while fixed effects without unit indicate change in intercept. The reference was the strain SS104 with *genotype* “no Tau” and *labelling* “no labelling”. The p-value indicates the probability of obtaining the coefficient as listed, under the assumption that the fixed effect does not predict the outcome.

3.4 Additional Recordings Using RAPID

3.4.1 Recordings from Run 11 and 13

To check the sensitivity of RAPID, we recorded three different strains under various conditions. The results from these recordings are shown in Figure 28 and the number of worms used in each run is shown in Table 16.

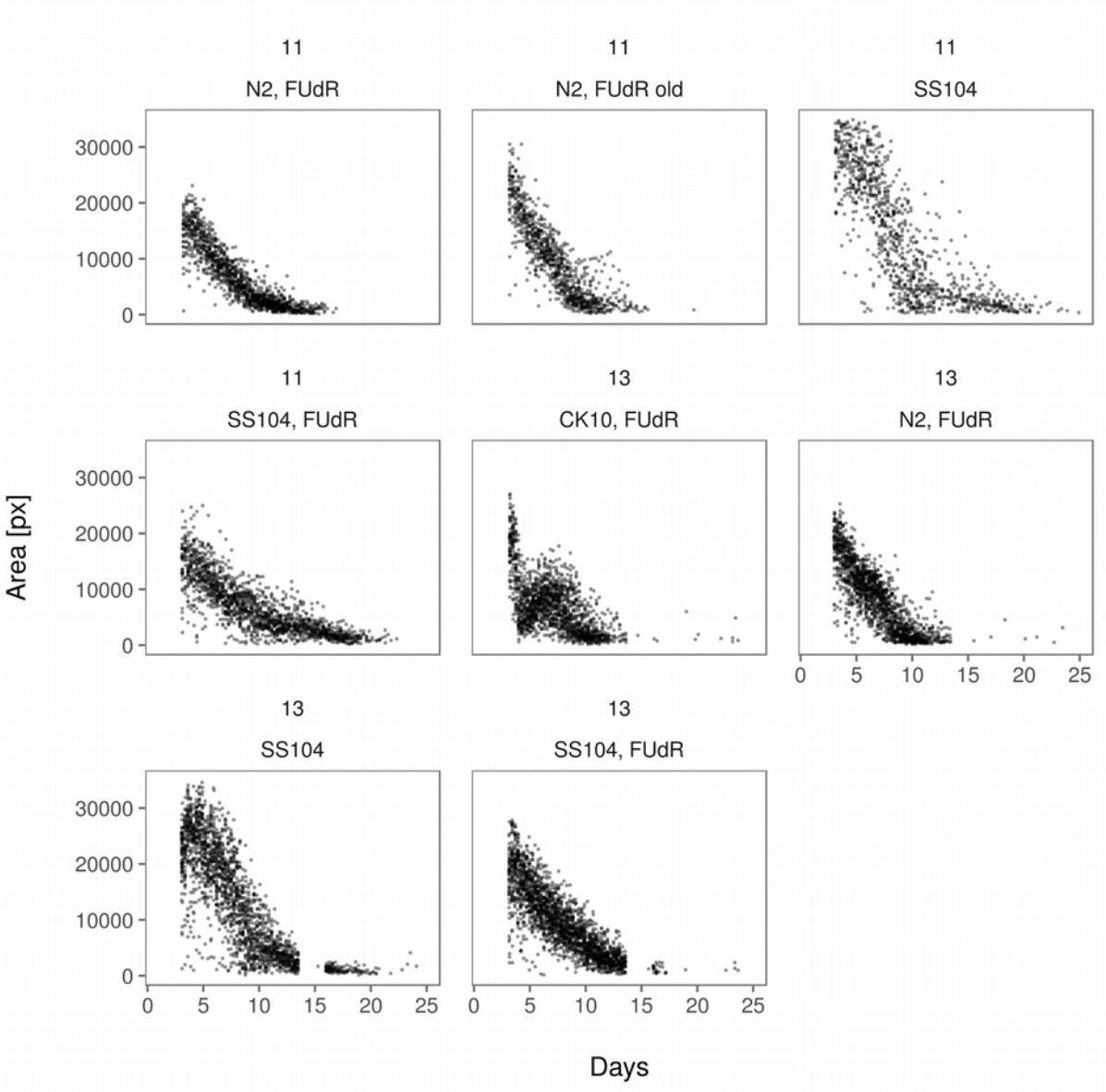

Figure 28: Additional Recordings Using RAPID

Recordings of the strains wild type (N2), SS104 and CK10, FUdR indicates the strain was recorded on NGM plates containing 10 µg/ml FUdR, FUdR old indicates, the strain was recorded on FUdR plates which were stored for more than 2 weeks.

Strain / Condition	Run 11	Run 13
N2, FUdR	37	65
SS104	37	69
SS104, FUdR	38	67
N2, FUdR old	38	-
CK10, FUdR	-	62
Temperature	25.7	26.7

Table 16: Additonal Strains Recorded Using RAPID

Number of worms used per strain and run. N2, FUdR, SS104, FUdR and CK10, FUdR were recorded on NGM plates containing 10 µg/ml FUdR. N2, FUdR old indicates, the strain was recorded on FUdR plates which were stored for more than 2 weeks. SS104 was recorded on standard NGM plates. Temperature indicates the average temperature during the respective run.

Since N2, and SS104 with and without FUdR was recorded in both runs, we can assess the variability between the runs. A linear mixed model was fitted as described in equation (1), treating each strain/condition per run as individual fixed effect for comparison.
Figure 29 shows the combined data from run 11 and run 13 as well as the predictions from the fitted model. The fixed effect coefficients are shown in Figure 29.

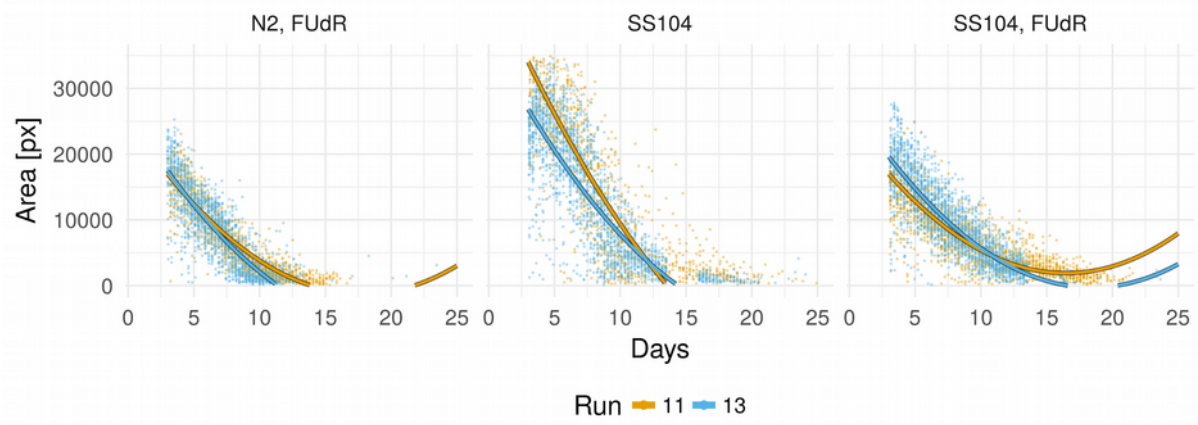

Figure 29: Comparison of Independent Runs

Three different strains/conditions were recorded in two independent runs. Run 13 was started almost 3 months after run 11. N2, FUdR and SS104, FUdR were recorded on NGM plates containing 10 µg/ml FUdR, while SS104 was recorded on regular NGM plates.

A linear mixed effect model was fitted to combined data obtained in run 11 and 13. *Area* is predicted by the fixed effects *age*, the interaction *age:strain*, *strain*, a quadratic fixed effect for age^2, and *temperature*. Strains from each run were treated independently. The lines show the predictions from the fitted model using the value of the fixed effects listed in Table 17.

Fixed Effect [per Unit]	Value [px]	Std.Error [px]	p-value
N2, FUdR (Run 11)	14761	1274	<0.001
N2, FUdR (Run 13)	1461	1023	0.154
SS104 (Run 11)	21931	1163	<0.001
SS104 (Run 13)	12388	1007	<0.001
SS104, FUdR (Run 11)	-677	1119	0.546
SS104, FUdR (Run 13)	2945	1006	0.004
temperature [°C]	394	38	<0.001
age [day]	-2963	93	<0.001
age [day^2]	83	3	<0.001
age:N2, FUdR (Run 13) [day]	-319	107	0.003
age:SS104 (Run 11) [day]	-1633	121	<0.001
age:SS104 (Run 13) [day]	-841	104	<0.001
age:SS104, FUdR (Run 11) [day]	224	113	0.048
age:SS104, FUdR (Run 13) [day]	-108	103	0.294

Table 17: Estimated Fixed Effects for Comparison Between Runs
Fixed effects fitted to data of Figure 29 for the combined data of run 11 and run 13. Each strain per run was treated as independent strain to enable comparison between the runs. The values of the fixed effects are listed in changes of area in pixels. N2, FUdR (Run 11) was chosen as reference (common intercept), to which the fixed effect of *strain* are added. Fixed effects *age*, *temperature* and the interaction *age:strain* indicate change in area per unit. The p-value indicates the probability of obtaining the coefficient as listed, under the assumption that the fixed effect does not predict the outcome.

Since FUdR is known to have an effect on body size when applied before maturation (Gandhi et al., 1980), we measured the width of 10 worms of each strain of run 11, using the images recorded with RAPID. The measurements are listed in Table 18.

Run 11	N2, FUdR [px]	SS104 [px]	SS104, FUdR [px]
	15.12	19.68	15.14
	14.76	16	14.54
	13.88	17.87	14.78
	14.43	20.13	13.9
	14.87	17.76	14.58
	13.2	17.9	14.63
	14.94	17.46	16.6
	15.79	18.5	15.76
	14.74	17.14	15.12
	15.73	18.88	14.75
mean [px]	14.75	18.13	14.98
SD [px]	0.78	1.22	0.75

Table 18: Effect of FUdR on Body Width

The width of 10 worms of each strain used in run 11 was measured. The values indicated are the width in pixel, mean: mean value of all measurements, SD: standard deviation.

3.5 Attempts to Create an Aggregation and Spreading Model

One of the defining hallmarks of tauopathies is the appearance of intraneuronal tau aggregates. As described in section “Induction of Tau Aggregation by Expression of Mutated Tau”, these tau aggregates can be induced in mice by expression of mutated hTau as well as by injection of preformed fibrils. In analogy to the mouse models expressing mutated hTau in restricted brain regions (de Calignon et al., 2012; Harris et al., 2012; Liu et al., 2012), we created worm strains expressing mutated hTau (1N4R, V337M) in the touch neurons, and strains expressing hTau (1N4R, wt) pan-neuronally. By crossing these lines and performing IHC at different timepoints, we investigated the possible seeding effect of the mutated hTau. Figure 30 shows epifluorescence images of the mutated hTau, wt hTau, and the crossbred double-homozygous transgenic animals.

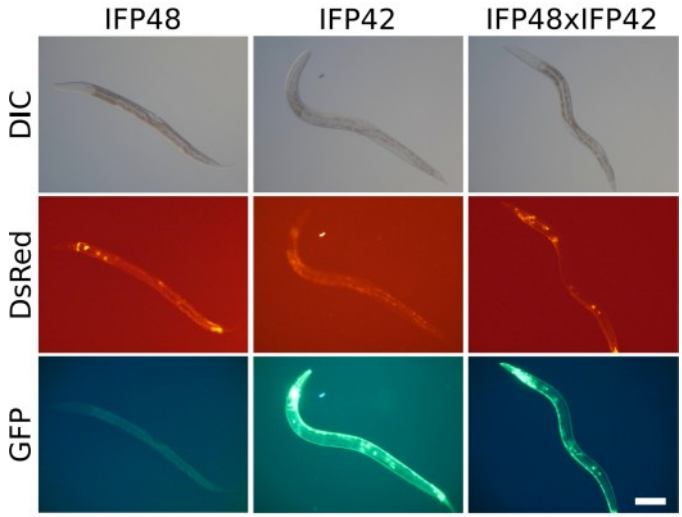

Figure 30: Attempted hTau Spreading Model in C. elegans

Spreading model of hTau in *C. elegans*, epifluorescence images of worms on day 2 after hatching. IFP48 expresses hTau (1N4R, V337M) and DsRed in the touch neurons, while IFP42 expresses hTau (1N4R, wt) and GFP pan-neuronally. IFP48xIFP42 inidcates the cross of both lines, thereby leading to expression of mutated hTau in the touch neurons and wt hTau in all neurons. DIC: differential interference contrast, DsRed: filter set for DsRed, GFP: filter set for GFP. Scale bar = 100 µm for all images (bottom right).

The IHC results of different time points are partially shown in Figure 31 and fully listed in Table 19.

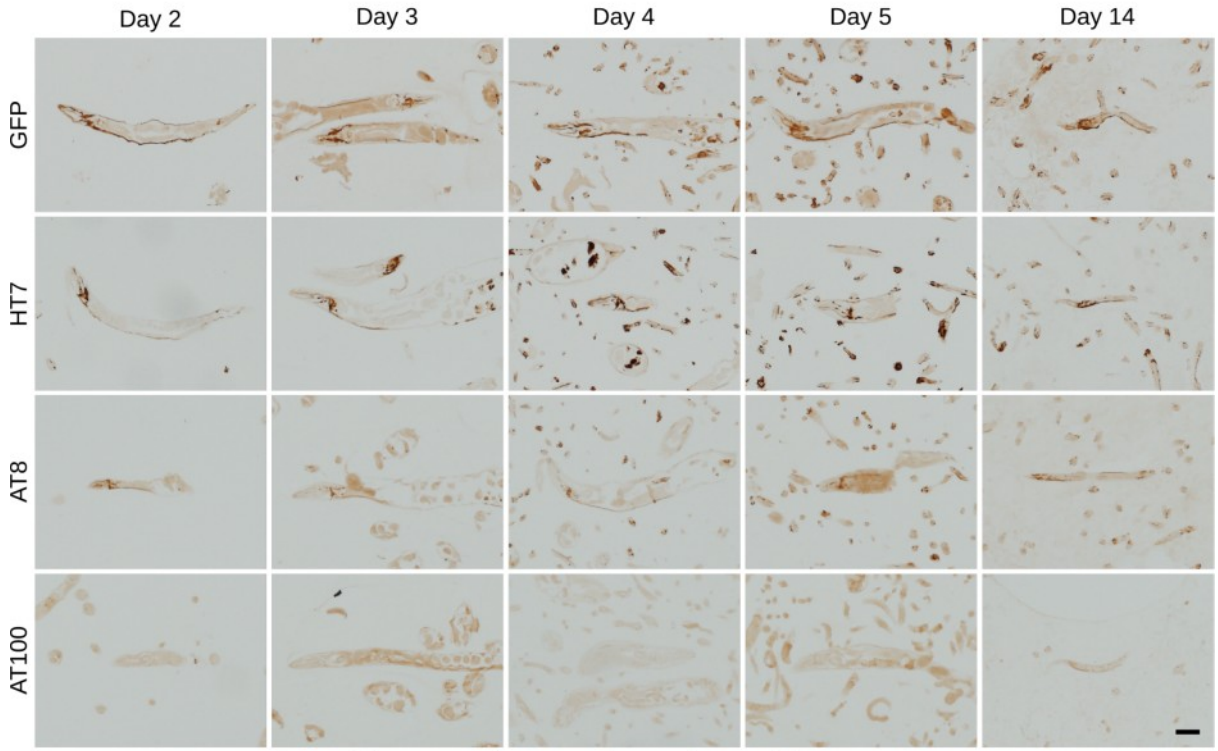

Figure 31: Expression of hTau and GFP Throughout Life

IHC of synchronized worm cultures from the hTau (1N4R, wt) and GFP expressing strain IFP42 at different time points indicated as chronological age in days since synchronization. Timepoints day 2 to day 5 are grown on standard NGM plates while day 14 were grown on NGM plates containing 125 µg/ml EtBr which leads to arrested larval development at stage L3 and therefore sterile worms. GFP: anti-GFP antibody, hTau antibodies used as listed in Table 10. The labelling intensity is comparable between the different timepoints, indicating stable expression of hTau and GFP. Scale bar = 50 µm for all images (bottom right).

Age	Strain	HT7	AT8	AT100	RFP	GFP
Day 2	IFP48	single cells+	-	-	single cells+	-
	IFP42	pan++	single cords+	-	-	pan++
	IFP48 x IFP42	pan++	pan++	single cells+	single cells+	pan++
Day 3	IFP48	-	-	-	single cells+	-
	IFP42	pan+	single cells+	-	-	pan++
	IFP48 x IFP42	pan++	pan+	-	single cells+	pan++
Day 4	IFP48	-	-	-	single cells+	-
	IFP42	pan++	pan+	-	-	pan++
	IFP48 x IFP42	pan++	pan++	cords+	single cells+	pan++
Day 5	IFP48	-	-	-	-	-
	IFP42	pan+	pan++	single cords+	-	pan++
	IFP48 x IFP42	pan++	pan++	single cords+	single cells+	pan++
Day 14	IFP48	-	-	-	NA	-
	IFP42	pan++	pan+	cords+	NA	pan+
	IFP48 x IFP42	pan++	pan+	cords+	NA	pan+

Table 19: IHC of hTau Spreading Model in C. elegans

Synchronized worm blocks of IFP48 (mutated hTau in touch neurons), IFP42 (wt hTau in all neurons) and the cross IFP48 x IFP42 at different timepoints; all transgenes in homozygous state. Timepoints day 2 to day 5 are grown on standard NGM plates while day 14 were grown on NGM plates containing 125 µg/ml EtBr which leads to arrested larval development at stage L3 and therefore sterile worms. The labeling distribution and intensity was evaluated in a blinded fashion in regard to strain or genotype and semi-quantitatively determined by comparison with the positive control CK10. Pan: pan-neuronal, cords: only processes, no labelling of somata, single cells: single cells in some of the worms, NA: not assessed.

3.5.1 Combining Gallyas and IHC to Locate Neurons

Since mutated hTau is co-expressed with DsRed and wt hTau is co-expressed with GFP, we used anti-GFP and anti-DsRed antibodies to locate these neurons. We combined IHC and Gallyas silver impregnation as shown in Figure 32.

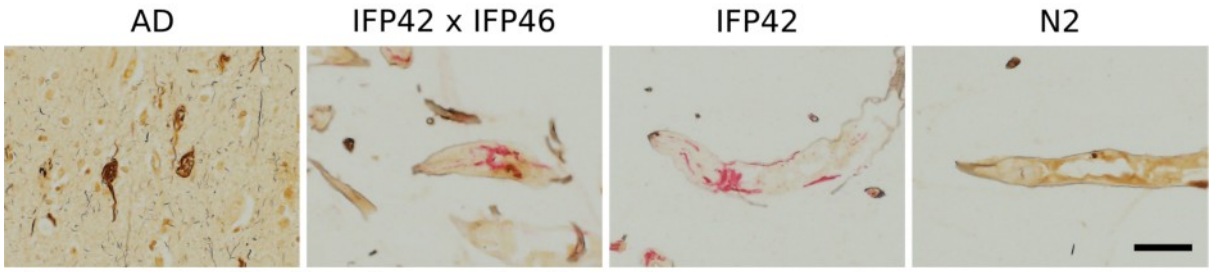

Figure 32: Combination of IHC and Gallyas Silver Impregnation

Anti-GFP (red) and Gallyas silver impregnation were successively applied to worm sections in order to locate neurons. AD: confirmed AD patient (positive control), IFP42 x IFP46: cross of pan-neuronal hTau (1N4R, wt) and touch neuronal hTau (1N4R, V337M) expressing strains, IFP42: pan-neuronal hTau (1N4R, wt), N2: wild type (negative control). All worm blocks were made from mixed populations of worms, scale bar = 50 µm for all images (bottom right).

3.6 Contributions to Manuscripts

3.6.1 Automated Quantification of Gallyas Silver Impregnation

To quantify the extent of tau aggregation as detected by Gallyas silver impregnation after intraperitoneal injection of brain homogenates from 6 month old homozygous hTau (0N4R, P301S) expressing mice into heterozygous hTau (0N4R, P301) expressing mice (Clavaguera et al., 2014), we developed an automated imaging pipeline and analysis tools. A microscope with a motorized x-y stage was equipped with a motorized focus to scan whole brain mouse sections. A predefined region of interest (ROI) was scanned with 20x magnification, recording a movie shifting the focus through the section from top to bottom. The stage is moved to the next field of view and the focus is shifted back up again. After the whole ROI is scanned, the sharpest image of each field of view is determined and the ROI is stitched to create an overview image. The overview image is used to annotate predefined anatomical landmarks and brain regions to be analysed. The original images are processed using colour deconvolution and thresholding of black, i.e. Gallyas-positive, and blue, i.e. nuclei structures for quantification. The images are coloured according to the ratio of Gallyas-positive structures to nuclei (G/N). All brain sections of the non-injected control and the injected experimental groups are superimposed using the defined anatomical landmarks. The average G/N ratio between the two groups are compared using a pixel-wise Student's *t*-test. The p-values of this *t*-test are plotted on a schematic representation of the mouse brain to reveal brain regions with significant differences in G/N ratio. Figure 33 shows an overview of a scanned brain section as well as the averages for the non-injected and the injected group and their comparison.

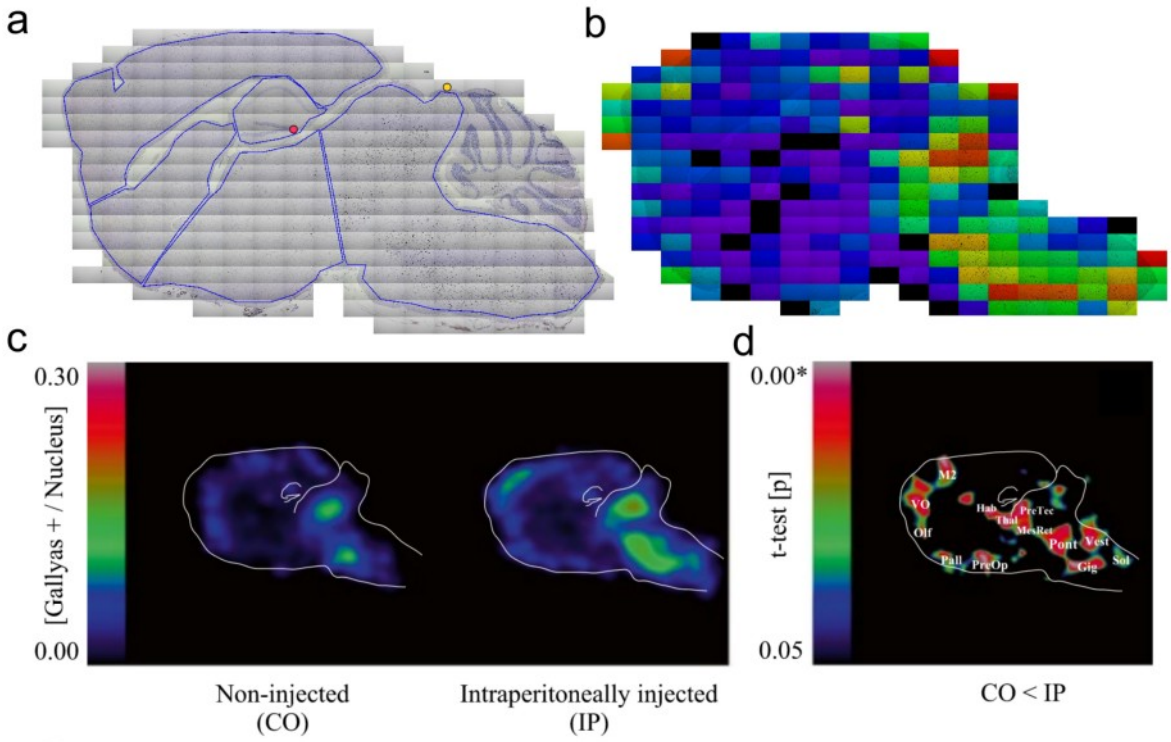

Figure 33: Automated Quantification of Gallyas Silver Impregnation

Automated brain scanning and comparison of tau aggregation in heterozygous hTau (0N4R, P301S) mice injected with brain homogenates from homozygous hTau (0N4R, P301S) mice, modified from (Clavaguera et al., 2014). The Gallyas stained whole brain sections are automatically scanned and stitched to create an overview for annotation of anatomical landmarks and brain regions for analysis (a). The ratio between Gallyas positive particles and nuclei (G/N) is determined using image processing and the image in (a) is coloured according to the G/N ratio (b) of the respective image tile. All brain sections of the non-injected control and injected experimental groups are superimposed and the average calculated (c). A pixel-wise Student's *t*-test reveals significant differences in the G/N ratios at specific brain regions between the two groups (d).

3.6.2 Correlative Light- and Electron Microscopy

A common problem in electron microscopy (EM) of tissue sections is unambiguous identification of the structure of interest. In our case, we intended to analyse tau aggregates ultrastructurally in the neurons of *C. elegans*. To identify the neurons before EM, we established IHC on epon embedded tissue as described in (Vidal et al., 1995). In addition, we successfully performed Gallyas silver impregnation on epon-embedded semithin sections of *post mortem* human tissue from an AD patient, see Figure 34.

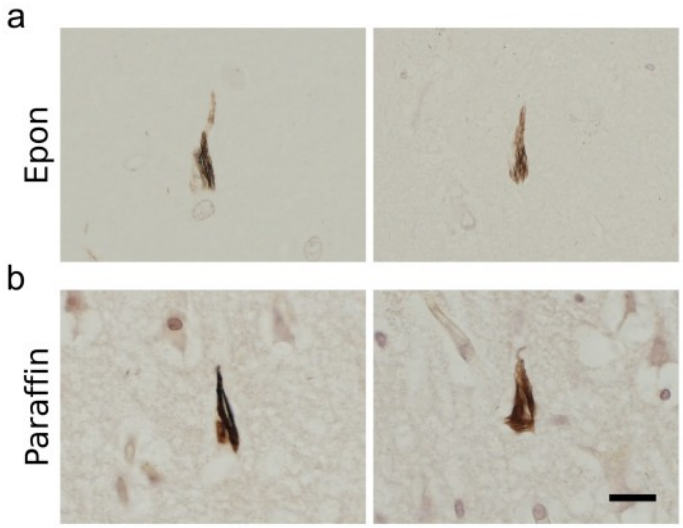

Figure 34: Gallyas Silver Impregnation on Epon Sections

Comparison of Gallyas silver impregnation on a human hippocampus. 1 µm thick epon sections, on which the epon was removed using a saturated solution of KOH in absolute EtOH to make the tissue permeable, stained with Gallyas silver impregnation (a). 4 µm thick sections from an adjacent slice of the same hippocampus, formalin-fixed, paraffin-embedded, and stained with Gallyas silver impregnation for comparison (b). Scale bar = 20 µm for all images (bottom right).

A region from the epon block shown in Figure 34 was trimmed for ultrathin sectioning size to include a tangle bearing neuron. Figure 35 shows an electron microscopy image of structures resembling PHFs.

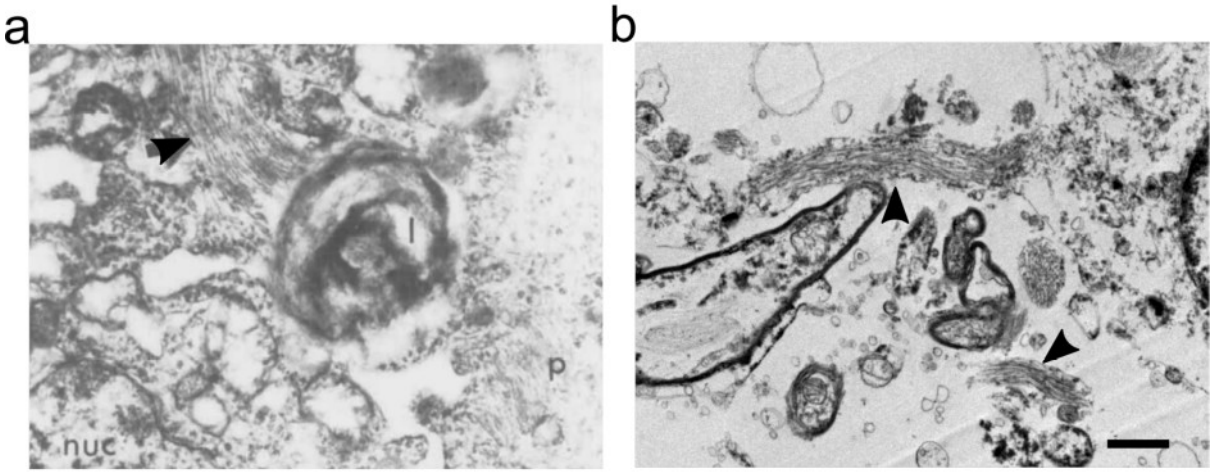

Figure 35: Transmission Electron Micorcopy of PHFs

Transmission electron microscopy images of tissue section from AD patients. Biopsy of a patient showing clinical signs of AD, adapted from (Gray, 1987) (a). Ultrathin sections of an autopsy derived sample from a confirmed AD patient (b), same block as shown in Figure 34 (top). Arrowheads: structures resembling PHFs. Scale bar = 1 µm for both images (bottom right).

Although our correlative light- and electron microscopy protocol was ultimately not used to study tau aggregates in *C. elegans*, we instead applied this technique to locate Lewy bodies in *post mortem* tissue of a patients who had suffered from Parkinson's disease, see Figure 36.

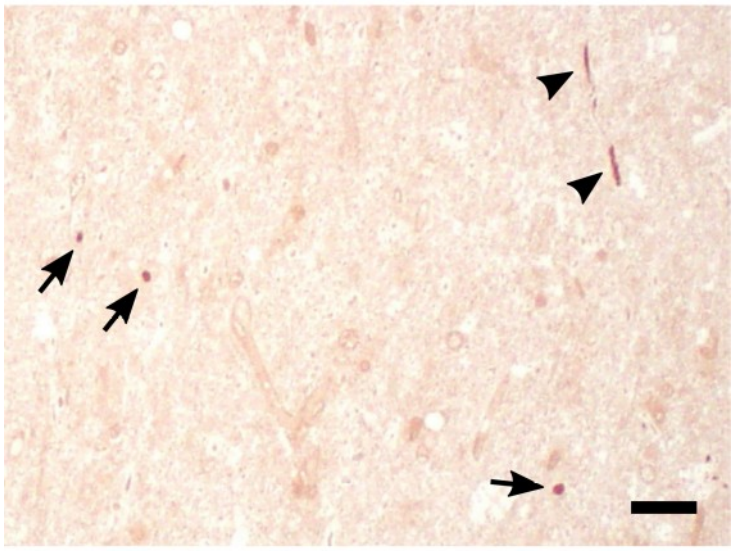

Figure 36: Detection of Lewy Bodies on Epon Sections

Semithin section of epon embedded human Parkinson's disease tissue. The epon was removed and IHC for α-synuclein was performed to locate the Lewy bodies (arrows) and Lewy neurites (arrowheads) within the section. By alternating semithin with ultrathin sections, the adjacent ultrathin section were used to image the located structures using EM. Scale bar = 25 µm.

The located Lewy bodies were then ultrastructurally examined by our collaborators. The results from these and other experiments were submitted for publication and are available as a preprint (Shahmoradian et al., 2017). In short, unambiguous distinction between Lewy bodies, Lewy neurites, and the more numerous Corpora amylacea which are easily mistaken as Lewy bodies, was facilitated.

3.6.3 Sample Preparation for Micro-Computed Tomography of Formalin-Fixed Brain Tissue

Histology is the gold standard for tissue examination and offers high lateral resolution but is usually limited to thin sections of several µm. To study larger volumes of tissue in all three dimensions, new imaging modalities are being developed. A method which offers sufficiently high resolution of low absorbing biological material without the use of contrast agents is micro-computed tomography (µCT). We introduced an FFPE sample preparation protocol for µCT imaging of human brain tissue and subsequently validated µCT data histologically. This preparation method was used to study the distribution of Purkinje cells in human cerebellum using hard X-ray phase tomography (Hieber et al., 2016) as well as to virtually extend histology to three dimensions using absorption-contrast µCT (Khimchenko et al., 2016).

3.7 References

Brandt, R., Gergou, A., Wacker, I., Fath, T., Hutter, H., 2009. A Caenorhabditis elegans model of tau hyperphosphorylation: induction of developmental defects by transgenic overexpression of Alzheimer's disease-like modified tau. Neurobiol. Aging 30, 22–33. doi:10.1016/j.neurobiolaging.2007.05.011

Clavaguera, F., Hench, J., Lavenir, I., **Schweighauser, G.**, Frank, S., Goedert, M., Tolnay, M., 2014. Peripheral administration of tau aggregates triggers intracerebral tauopathy in transgenic mice. Acta Neuropathol. 127, 299–301. doi:10.1007/s00401-013-1231-5

de Calignon, A., Polydoro, M., Suárez-Calvet, M., William, C., Adamowicz, D.H., Kopeikina, K.J., Pitstick, R., Sahara, N., Ashe, K.H., Carlson, G.A., Spires-Jones, T.L., Hyman, B.T., 2012. Propagation of Tau Pathology in a Model of Early Alzheimer's Disease. Neuron 73, 685–697. doi:10.1016/j.neuron.2011.11.033

Gandhi, S., Santelli, J., Mitchell, D.H., Wesley Stiles, J., Rao Sanadi, D., 1980. A simple method for maintaining large, aging populations of Caenorhabditis elegans. Mech. Ageing Dev. 12, 137–150. doi:10.1016/0047-6374(80)90090-1

Gray, E., 1987. Alzheimer's disease: paired helical filaments and cytomembranes. … Appl. Neurobiol. 91–110.

Harris, J.A., Koyama, A., Maeda, S., Ho, K., Devidze, N., Dubal, D.B., Yu, G.Q., Masliah, E., Mucke, L., 2012. Human P301L-Mutant Tau Expression in Mouse Entorhinal-Hippocampal Network Causes Tau Aggregation and Presynaptic Pathology but No Cognitive Deficits. PLoS One 7. doi:10.1371/journal.pone.0045881

Hench, J., Bratić Hench, I., Pujol, C., Ipsen, S., Brodesser, S., Mourier, A., Tolnay, M., Frank, S., Trifunović, A., 2011. A Tissue-Specific Approach to the Analysis of Metabolic Changes in Caenorhabditis elegans. PLoS One 6, e28417. doi:10.1371/journal.pone.0028417

Hieber, S.E., Bikis, C., Khimchenko, A., **Schweighauser, G.**, Hench, J., Chicherova, N., Schulz, G., Müller, B., 2016. Tomographic brain imaging with nucleolar detail and automatic cell counting. Sci. Rep. 6, 32156. doi:10.1038/srep32156

Jain, D., Mathur, S.R., Iyer, V.K., 2014. Cell blocks in cytopathology: A review of preparative methods, utility in diagnosis and role in ancillary studies. Cytopathology 25, 356–371. doi:10.1111/cyt.12174

Khimchenko, A., Deyhle, H., Schulz, G., Schweighauser, G., Hench, J., Chicherova, N., Bikis, C., Hieber, S.E., Müller, B., 2016. Extending two-dimensional histology into the third dimension through conventional micro computed tomography. Neuroimage 139, 26–36. doi:10.1016/j.neuroimage.2016.06.005

Kokkat, T.J., Patel, M.S., McGarvey, D., LiVolsi, V.A., Baloch, Z.W., 2013. Archived Formalin-Fixed Paraffin-Embedded (FFPE) Blocks: A Valuable Underexploited Resource for Extraction of DNA, RNA, and Protein. Biopreserv. Biobank. 11, 101–106. doi:10.1089/bio.2012.0052

Kraemer, B.C., Zhang, B., Leverenz, J.B., Thomas, J.H., Trojanowski, J.Q., Schellenberg, G.D., 2003. Neurodegeneration and defective neurotransmission in a Caenorhabditis elegans model of tauopathy. Proc. Natl. Acad. Sci. U. S. A. 100, 9980–5. doi:10.1073/pnas.1533448100

Liu, L., Drouet, V., Wu, J.W., Witter, M.P., Small, S.A., Clelland, C., Duff, K., 2012. Trans-synaptic spread of tau pathology in vivo. PLoS One 7, 1–9. doi:10.1371/journal.pone.0031302

Miyasaka, T., Ding, Z., Gengyo-Ando, K., Oue, M., Yamaguchi, H., Mitani, S., Ihara, Y., 2005. Progressive neurodegeneration in C. elegans model of tauopathy. Neurobiol. Dis. 20, 372–383. doi:10.1016/j.nbd.2005.03.017

Shahmoradian, S.H., Genoud, C., Graff-Meyer, A., Hench, J., Moors, T., **Schweighauser, G.**, et al., 2017. Lewy pathology in Parkinson's disease consists of a crowded organellar membranous medley. bioRxiv.

Vidal, S., Lombardero, M., Sánchez, P., Román, a, Moya, L., 1995. An easy method for the removal of Epon resin from semi-thin sections. Application of the avidin-biotin technique. Histochem. J. 27, 204–9.

4 Discussion

4.1 Reviewer Comments on RAPID Manuscript

As mentioned in section “Manuscript: RAPID - High-throughput standardized health modelling in C. elegans”, we received feedback from two reviewers concerning our manuscript “RAPID - High-throughput standardized health modelling in *C. elegans*” which is summarised and addressed in this section.

We were asked to compare RAPID with the Multi-Worm Tracker (MWT) (Swierczek, Giles, Rankin, & Kerr, 2011) and a more recent report (Podshivalova, Kerr, & Kenyon, 2017) in which two *daf-2* mutants were examined using the MWT. In general, we will need to provide more measurements obtained from long-lived mutants since the focus of our manuscript is centered around RAPID applied as a tool to study locomotor performance during ageing. We should address how the decline patterns of long-lived mutants compare with wild type and if this pattern was shared among long-lived mutants. By performing these experiments in replicates, we were asked to assess if RAPID was suitable for robust and standardized compound evaluation and therefore a useful addition to the *Caenorhabditis* Intervention Testing Program (CITP) (Lucanic et al., 2017). Lastly, a simultaneous conventional lifespan assay should be performed in parallel to validate automated lifespan determination based on RAPID datasets.

In contrast to MWT, RAPID allows longitudinal, high-throughput recordings of individual worms where each measurement can be unambiguously attributed to a particular animal. This sets RAPID apart from the majority of worm-tracking approaches including MWT, which was built to record and track up to 120 worms in parallel on the same plate (Swierczek et al., 2011), thereby prohibiting longitudinal studies. In order to make a direct comparison between the imaging performance of RAPID and the MWT, we might record video data with RAPID instead of series of still images and then use the MWTs image analysis module to extract locomotion parameters. Alternatively, we could integrate the tracking algorithm of MWT in our analysis pipeline. Similar to RAPID, MWT uses image subtraction to detect moving objects, i.e. worms, but then differs from our approach by using the detected pixels as starting point for a flood-fill operation to segment a worm. It remains to be evaluated how well the MWT algorithm performs under RAPID imaging conditions on standard NGM plates with living bacteria. Importantly, the subsequent statistical analysis of RAPID data is independent of the track extraction method and could be directly applied to longitudinal data recorded using another system such as the MWT.

For the proof-of-principle experiment outlined in the manuscript we chose worm strains displaying a variety of locomotor phenotypes. We discovered the true potential of RAPID in the study of ageing and health assessment and therefore acquired more long-lived mutants from the *Caenorhabditis* Genetics Center including strains with mutations in the insulin/IGF-1 pathway. This will enable a more in depth study of decline patterns of long-lived strains and compare how these different mutants age.

As discussed in the manuscript, we are aware of the fact that we underestimate the time of death of worms recorded using RAPID. Instead of performing a manual ageing assay in parallel by hand, we can inspect the recorded tracks visually and determine the time of death retrospectively. This would allow additional censoring of worms that “got lost” and died outside the field of view. However, accurate lifespan determination is not the aim of RAPID, since a more appropriate automated system was developed for this purpose (Stroustrup et al., 2013).

A more technical point of concern was the recreation of RAPID by other labs. Undoubtedly, RAPID is a complex system with different subsystems performing in concert. The three main subsystems are: the imaging platforms, the analysis software and a mechanism to switch the plates, in our case an industrial robotic arm. Importantly, these subsystems are interchangeable and RAPID is only one possible implementation. The value of RAPID is the general idea of recording single worms on standard NGM plates, increasing the throughput by multiplexing of the imaging platforms and using an automated system to load and unload the plates. This enables acquisition of longitudinal data which otherwise can not be easily obtained.

We designed RAPID based on open source software and all our soft- and hardware designs are released to the public on github (https://github.com/gabe0815/RAPID).

4.2 Histology of hTau-Expressing *C. elegans*

The generation of worm blocks using the cell block technique has proven to be an ideal method to study hTau expression and the phosphorylation state of tau. In theory, a worm block with 3 mm of tissue will yield 750 sections of 4 µm thickness, facilitating retrospective comparison of different worm blocks over a long period of time. No special equipment is needed and worm blocks can be generated with consistent quality. Induction of sterility by crossing worm strains with sterile mutants such as *glp-4(bn2)* or by using chemicals such as ethidium bromide or FUdR greatly facilitates the culture of synchronized worm populations past the onset of reproduction. The number of adult worms in a synchronized population is quickly outnumbered by the large amount of progeny which can not always be distinguished from the older adults. Generation of synchronized worm blocks from 1 day old adults is unaffected by these problems and can be obtained using fertile hermaphrodites.

Expression of hTau of the newly generated worm strains is similar to the worm strains obtained from Kraemer et al. (Kraemer et al., 2003) and Brandt et al. (Brandt, Gergou, Wacker, Fath, & Hutter, 2009) (see Figure 18 and Figure 21). Human tau is stably expressed throughout the nervous system, and is phosphorylated at the AT8 and AT100 epitope, indicating the presence of hTau phosphorylating kinases. Expression of hTau and its phosphorylation can be detected throughout life (Figure 30).

AT8 and AT100 labelling seems to be dependent on expression level of hTau, since the labelling intensities follow the form HT7 > AT8 > AT100. If we test this assumption for HT7 and AT8 we find a significant positive correlation (Figure 37).

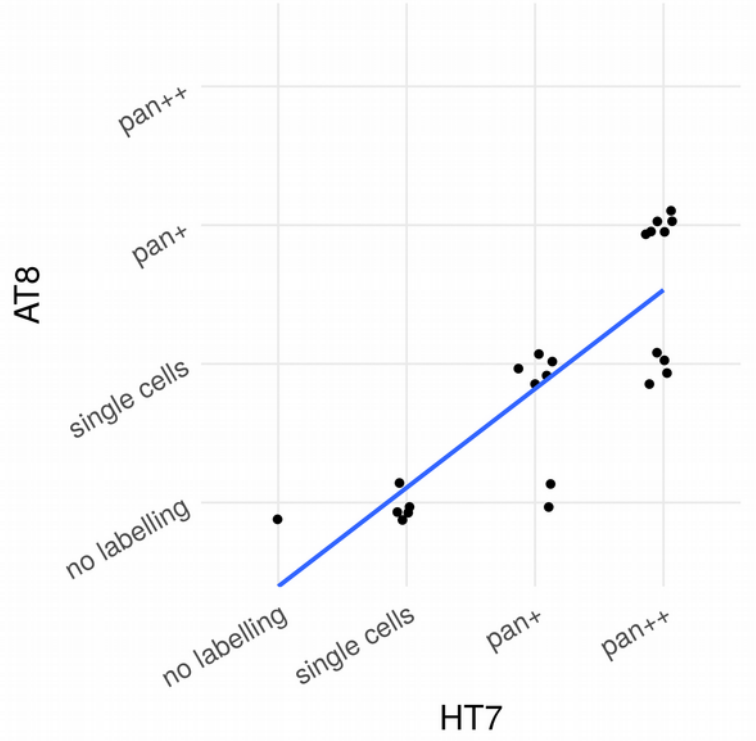

Figure 37: Corrleation Between AT8 and HT7 Labelling

AT8 labelling versus HT7 as summarized in Table 12 reveals a positive correlation between HT7 labelling and AT8 phosphorylation. The Spearman's rank correlation coefficient is 0.85. Individual points were scattered and linear regression was fitted for illustration purposes only.

This labelling pattern is also observed in mice expressing hTau (0N4R, P301S), where AT8-positive cells outnumber AT100-positive ones (Allen et al., 2002). The reason for this observation could be a lower detection sensitivity of AT8 and AT100 compared to HT7.

AT100 labelling does not seem to be dependent on the hTau construct expressed, since it is present in strains expressing hTau (1N4R, wt) as well as in the positive control expressing hTau (1N4R, V337M). None of the hTau (1N4R, P301S) strains were positive for AT8 nor AT100 labelling, again possibly due to the to the lower detection sensitivity. The strain VH254 listed in Table 11 indicates, that AT100 phosphorylation is not dependent on phosphorylation of AT8 epitope, since the respective transgene has a mutated AT8 epitope and is therefore AT8-negative. Hence, hTau phosphorylation in *C. elegans* differs from hTau phosphorylation *in vitro* (Zheng-Fischhöfer, 1998).

Diagnostic criteria common to tauopathies are neuronal inclusions of tau protein most of which can be demonstrated using various physical silver stains. Gallyas silver impregnation is one of the most sensitive silver staining methods for NFTs and able to detect filamentous tau made up of isoforms with four MT binding repeats (0N4R, 1N4R, and 2N4R) (Uchihara, 2007). Silver staining methods share a common principle: silver ions (Ag+) in solution penetrate the tissue and selectively attach to specific structures building silver-ion complexes. In a second step, often called developing, these attached silver ions are reduced to metallic silver *in situ*, rendering the structures opaque, appearing black under a light microscope. Once mixed, the developer solution contains silver ions as well as the reducing agent. The time between mixing the developer solution and immersion of the sections is critical, as the developer starts reacting by itself, continuously decreasing the amount of available silver ions and reducing agent. Hence the developing step is usually performed by hand under continuous visual inspection of a positive control slide for the staining intensity and stopped once the neurofibrillary tangles become evident. If the slides remain in the developed solution beyond this state, the entire tissue will be rendered black.

In order to systematically test Gallyas silver impregnation on sections of hTau-expressing *C. elegans* worm blocks, the staining procedure was standardized using a modified autostainer which allows consistent timing between automated mixing of the developer components, immersion, and stopping of the developing process.

No silver positive inclusions could be unambiguously demonstrated in the worm (Figure 19). If the developing step was intentionally prolonged, the worm sections were rendered black, still without apparent filamentous inclusions. To corroborate these findings, IHC was combined with Gallyas silver impregnation to localize the neurons based on detection of GFP, and although NFTs remained detectable in human control tissue after IHC, there were no silver-positive structures detectable within worm neurons (Figure 32).

Gallyas silver impregnation may fail due to some inherent differences of worm tissue; alternatively, hTau in *C. elegans* may actually not form silver-positive inclusions. Although the

size difference between *C. elegans* and mammalian neurons is considerable, Gallyas silver impregnation does stain the fine NTs in murine and human neurons which are similar in size to *C. elegans* neurites (Figure 19 and Figure 32).
Tau aggregation was observed ultrastructurally by electron microscopy, however the aggregates do not appear to be filamentous in nature (Kraemer et al., 2003). The reports on hTau-expressing worms summarized in section “C. elegans as Model System for Tauopathies” and Table 2 mostly focused on sequential extraction and western blotting to determine the solubility of tau.

As silver-positive tau inclusions were undetectable (or do not exist) in hTau-expressing worms, *C. elegans* seems rather unsuited to model and study the spreading phenomena of tau aggregates or the induction thereof. In sum our attempts failed to establish a *C. elegans* spreading model system expressing mutant hTau (1N4R, V337M) in a subset of neurons in a background where a pan-neuronal promoter drives hTau (1N4R, wt).

Instead of focussing on surrogate markers of tau aggregation and neurodegeneration as described in section “Surrogate Markers for Neurodegeneration”, we shifted our focus towards quantification of the functional consequences induced by expression of wt and mutated hTau in *C. elegans*.

4.3 Measuring Locomotor Decline Using RAPID

4.3.1 RAPID Sensitivity and Variation Between Runs

In order to assess the sensitivity of RAPID measurements, we recorded additional data from wild type N2 with FUdR and from the temperature-sensitive sterile mutant SS104 with and without FUdR in two different runs (Figure 28 and Figure 29).

Although the trajectory of a given strain between the two runs shows similarity, all of the estimated fixed effects for *strain* and the interaction *age:strain* are significantly different, except for the change in intercept for N2, FUdR (Run 13), SS104, FUdR (Run 11) and the interaction *age:SS104*, FUdR (Run 13). The differences in change of intercept in SS104 are almost twice as high in run 11 compared to run 13. The interaction *age:strain* is lower for run 13 than for run 11. Since the standard errors of fixed effects are comparable between the runs, we speculate that there are more fixed effects which could explain the difference between runs than we currently include in the model. Variation between the runs could arise due to differences in the assay plates, bacteria and bacterial density on the plates, temperature, temperature fluctuations, and epigenetic drift of the strains. These factors are known to have an effect on lifespan (Gruber et al., 2009) and hence might also impact locomotor performance.
The temperature during assay recording is not constant and therefore continuously recorded. By treating temperature as a fixed effect in our models, we can correct for temperature induced differences of performance at a given time point. However, we can not correct for the “cumulative” temperature the worm has experienced up until this point, since this parameter will differ between individuals. Although we adhere to the protocol described in section “Preparation of Worms for RAPID Assay”, some variation can not be excluded. As an exaggerated example, we performed and assay with N2 kept on NGM plates with FUdR which were stored longer than 2 weeks (Figure 28). The locomotor performance of these worms is appreciably different than N2 recorded on freshly prepared NGM plates containing FUdR. In sum, these experiments demonstrates, that the sensitivity of RAPID is sufficient to systematically investigate the effects of some of those factors.

Different genotypes recorded with RAPID were distributed across individual runs (Figure 22). This averages potential systematic effects of each run, leading to less biased data.

In runs 11 and 13 it can be appreciated that SS104 growing on FUdR plates perform worse than on regular NGM. FUdR decreases the body width of SS104 animals by almost 20 % which will also decrease the measured track area by at least the same amount. The apparent difference in locomotor performance measured by RAPID is therefore in part due the change in body width. A tracking method with worm segmentation and centroid speed extraction is unsusceptible to changes in body size and could be employed to determine the effect of FUdR on locomotor performance. Nonetheless, smaller worms will have different biomechanics of locomotion and centroid speed may not completely compensate for these differences.

To characterize the direct effect of FUdR on locomotor performance using RAPID, we will have to repeat the experiments with various concentrations of FUdR on SS104. We have

performed this experiment on wild type (N2) worms and did not observe an effect of FUdR concentration on locomotor performance (Figure 5).

4.3.2 Variation Within a Strain and the Rate of Ageing

From the broad distribution of measurements (Figure 23) we recognize that besides inter-strain differences variation can also be found between individual recordings of the same strain.

To determine how this distribution arises, we plotted individual worm trajectories. Since we are able to determine the lifespan of each worm, we can sort the individuals according to this parameter. Figure 38 shows all individuals of SS104 recorded in run 9.

Figure 38: Individual Trajectories of SS104

Individual trajectories of SS104 recorded in run 9, arranged according to their individual lifespan from left to right and top to bottom. The longest-lived individuals appear top left and the shortest-lived ones bottom right. The colour of each measurement indicates whether a worm is still alive (black) or if a particular measurement was determined to represent the time of death (red) as described in section “Modelling and statistical tests”. No additional censoring was applied, therefore the time of death may potentially be underestimated.

To compare the different rates of decline, we can fit each individual worm trajectory with a linear regression and colour the graphs according to lifespan (Figure 39).

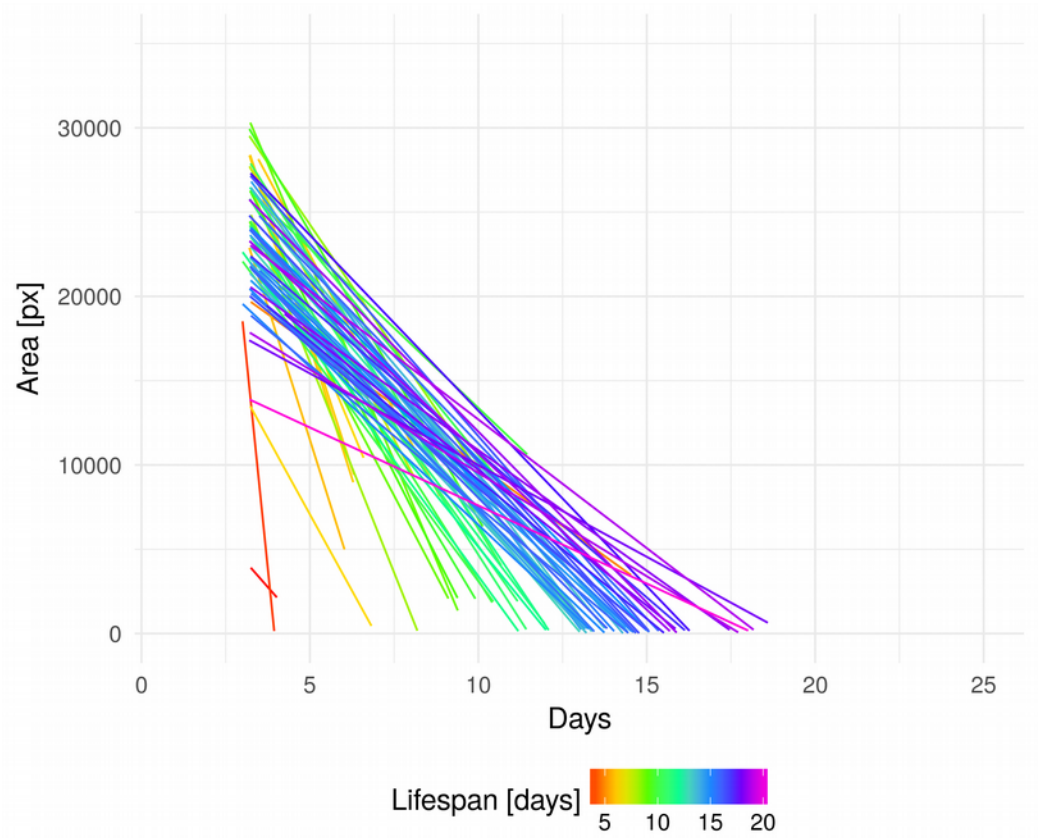

Figure 39: Rate of Ageing of SS104

Rate of ageing from SS104 recorded in run 9. Each line represents the linear regression through all the measurements of a single worm, same data as in Figure 38. Colour indicates the lifespan of the respective worm.

From Figure 38 and Figure 39 it can be appreciated that the long-lived lived individuals have a slower decline in locomotor performance and an extended period of poor performance later in life, whereas the short lived individuals show a faster decline without an extended period of poor performance. This notion is consistent with previous findings (Zhang et al., 2016). The rate of ageing was studied in an isogenic culture of wild type worms using longitudinal recordings of several physiological biomarkers of ageing, including locomotion. The authors report that short-lived individuals do not simply die prematurely and in fact undergo the same changes as the long lived individuals, but within a shorter period of time. They noted different

trajectories even among long-lived individuals, indicating that the ageing process itself is highly stochastic. Recently, a necropsy study on isogenic wild type worms was performed (Zhao et al., 2017). The reason for the early death of some individuals was attributed to a swelling of the pharynx due to bacterial infection. Interestingly, resistance to colonization of the pharynx by *E. coli* was also discovered as one mechanism for an extended state of poor performance late in life of long-lived *daf-2* mutants (Podshivalova et al., 2017). If infections are prevented by feeding dead bacteria, wild type worms live longer and also show a prolonged state of poor performance similar to the *daf-2* mutants (Podshivalova et al., 2017). To further test this hypothesis, we could employ RAPID on worms grown on dead bacteria and examine if these distinct rate of ageing trajectories still exist.

4.3.3 Effect of hTau Genotype on Stimulated Locomotor Performance

In order to compare the locomotor performance of hTau-expressing strains, we subjected 23 newly generated strains expressing hTau (1N4R, wt), hTau (1N4R, P301S), and hTau (1N4R, V337M) as well as a non transgenic control to a lifelong locomotor assessment using RAPID. Figure 23 shows all measurements per strain, coloured according to genotype. Figure 24 combines all measurements of each strain according to their hTau genotype. The plots reveal no obvious systematic differences between the hTau transgenic strains and the non transgenic control. Within each genotype there is a broad range of locomotor decline patterns.

Due to a technical failure during the recording of set 3, data are missing between day 4 and 5. Since the data are missing at random timepoints and not due to a biological trait of the strains recorded, the recordings remain valid for statistical evaluation.

To compare locomotor decline throughout life, we applied linear mixed-effect models as described in section “Manuscript: RAPID - High-throughput standardized health modelling in C. elegans”, and hereby estimated the effect of genotype on locomotor performance.
Model 1 was constructed to contain fixed effects for *age*, interaction *age:genotype*, *genotype*, age^2, and *temperature*. The model predicts the measured area at a given time by estimating an overall intercept and the fixed effects. The fixed effect *age* indicates the change in area per day, *age:genotype* additional change per day for a given genotype, *genotype* the change of area for a given genotype, age^2 changes in area per day^2, and *temperature* the change in area for a given temperature during the recording.

The model was fit to the data presented (Figure 23) with SS104 as reference. The predictions for the model are plotted in Figure 24.

To visualize how well the model predicts the measurements, we plotted the measured area against the predicted area per genotype (Figure 40).

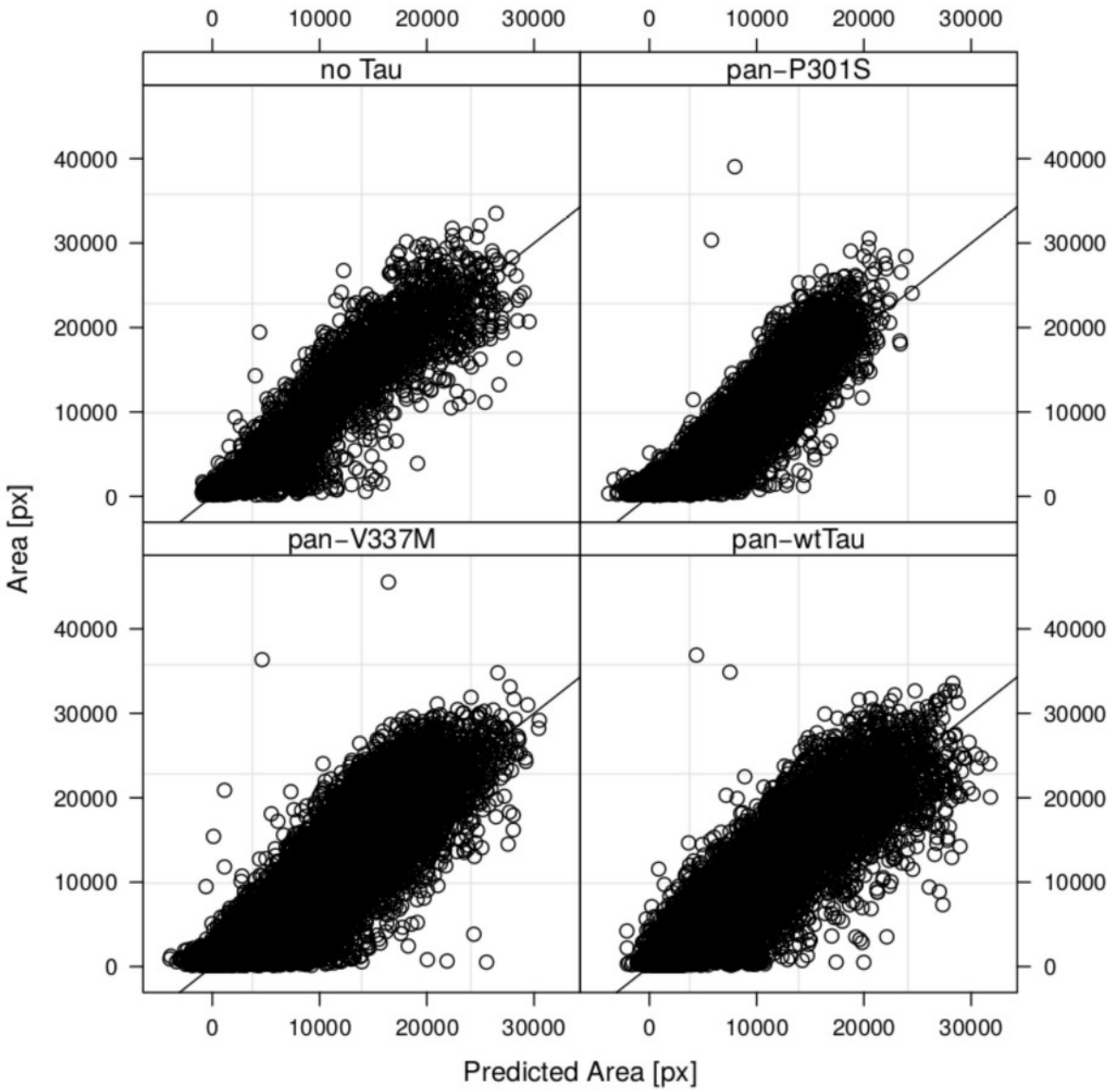

Figure 40: Measured Area vs Prediction for Model 1

Measured area vs. predicted area for model 1 per genotype. Each circle in the plot corresponds to one measurement and is plotted on the y-axis. The parameters for this particular measurement are applied to the model and the resulting prediction is plotted on the x-axis. The black line indicates the case for which the measured area corresponds to the predicted area (y = x).

This plot emphasizes, that the model describes all genotypes equally well and that there is quite some deviation from the ideal case (y = x). Furthermore, we can acknowledge outliers, possibly artifacts which were not detected during visual inspection. The estimated fixed effects for this model are listed in Table 14. Of the fixed effects of model 1, only *temperature*, as well as *age*, and age^2 are significant. A rise in temperature by 1 °C leads to an increase in area by 210 px, while each day decreases the area by 3860 px and increases the area by 108 px per day^2. Neither the fixed effects *genotype* nor the interactions *age:genotype* are significant, indicating hTau genotype does not have an effect on the locomotor performance nor its rate of decline.

4.3.4 Effect of hTau Expression Status on Stimulated Locomotor Performance

We verified hTau expression and phosphorylation state by immunohistochemical staining in each of the worm strains recorded by RAPID. The results are summarized in Table 12 and representative histological image examples are shown in Figure 21. Since the effect of hTau phosphorylation on neurodegeneration remains unclear, especially in the context of transgene overexpression, we focused our analysis on hTau expression detected by the phosphorylation-independent antibody HT7. For this experiment, analysis was only performed at one time point in life, since we previously determined that the hTau expression with these constructs is stable throughout life (Figure 30).

Each transgenic strain is expected to have a different expression level of hTau, since integration of extrachromosomal arrays leads to formation of multicopy arrays with different copy numbers (Mello, Kramer, Stinchcomb, & Ambros, 1991). To test whether the expression level of hTau has an effect on locomotor performance, we constructed a linear mixed-effect model. Model 2 contains fixed effects for *age*, interaction *age:labelling*, a fixed effect for hTau expression level which we termed *labelling*, age^2, *genotype*, and *temperature*. This model estimates an overall intercept for the reference condition SS104, which has the *labelling* state “no labelling” and the *genotype* “no Tau”. The interpretation of the fixed effects is the same as described for model 1, with the exceptions that if labelling is detected, the interaction *age:labelling* estimates relative changes in area per day and *labelling* relative changes of the intercept.

The labelling intensities were assessed in a semi-quantitative manner and the distinction between pan++ and pan+ is not always as pronounced as depicted in Figure 20. Therefore we have grouped pan++ and pan+ together as tau-positive or labelling and single cells and negative as tau-negative or no labelling for the labelling status in model 2.

Figure 27 shows the predictions from the fitted model 2, grouped by the *labelling* status and coloured according to the hTau genotype using the fixed effects listed in Table 15. To check how well model 2 predicts the measured data, we plotted the measured values against the prediction (Figure 41).

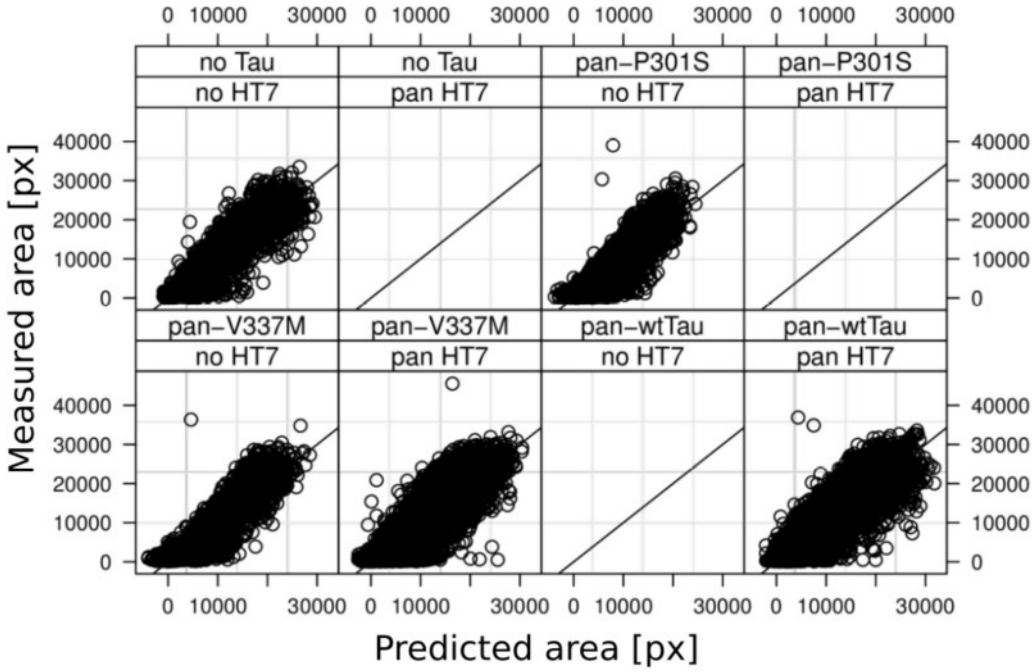

Figure 41: Measured Area vs Prediction for Model 2

Measured area vs. predicted area of model 2 for all combinations of *labelling* (no HT7 or pan-neuronal HT7 labelling) and *genotype*. Since not all combinations exist, the respective plots are omitted. Each circle corresponds to one measurement and is plotted on the y-axis. The parameters for this particular measurement are applied to the model and the resulting prediction is plotted on the x-axis. The black line indicates the case for which the measured area corresponds to the predicted area (y = x).

The model describes all strains reasonably well, and as with model 1, there is a high amount of deviation from the ideal line (y = x) in all the strains.

Estimated fixed effects are compared with the reference SS104, which has the *labelling* status “no labelling” and *genotype* “no Tau”. Fixed effects for *temperature*, *age*, and age^2 are significant. Raising the temperature by 1 °C increases the measured area by 210 px, each day decreases the area by 3768 px and increases it by 108 px for each day^2. The *genotypes* hTau (1N4R, P301S) decreases the intercept by 3692 px and hTau (1N4R, V337M) decreases the intercept by 3239 px, while the change in intercept for the *genotype* hTau (1N4R, wt) is not significant. This indicates that the genotypes hTau (1N4R, P301S) and hTau (1N4R, V337M) perform worse than the reference SS104, which has the genotype “no Tau”. The fixed effect *labelling* significantly increases the area by 228 px per day, indicating tau has an unexpected small, but positive effect on the rate of decline, irrespective of the actual hTau genotype.

4.3.5 Comparison of Model 1 and Model 2

In model 1, the fixed effect *genotype* is not significantly different from the reference in any of the genotypes, while in model 2 *genotype* is significantly different for hTau (1N4R, P301S) and hTau (1N4R, V337M). We recorded all strains generated for this study without prior screening for hTau expression and used GFP expression as surrogate marker for integration of both constructs. This did not result in all possible combinations of *genotype* and *labelling* (Figure 41, Table 12). After applying a classification that defines tau-positive as pan-neuronal staining and less prominent immunoreactivity as tau negative, all four hTau (1N4R, P301S) strains are tau-negative and all six of the hTau (1N4R, wt) strains are tau-positive. Interestingly, the performance of the labelling negative hTau (1N4R, P301S) strains is marginally worse than the reference and worse than the labelling positive hTau (1N4R, wt) strains (Figure 23).

Given our data, model 2 predicts that transgenic hTau expression ameliorates the performance decline during ageing. An alternative explanation is, that the model attributes the differences between the genotypes hTau (1N4R, wt) and hTau (1N4R, P301S) to the fixed effect *labelling* since it coincidentally defines the two groups. The reason for the lack of high expressing hTau (1N4R, P301S) worms might be due to a toxic effect of this construct. This would lead to a bias towards low-expressing lines. Nonetheless, we successfully generated high-expressing lines of a different mutant hTau (1N4R, V337M) and others (Kraemer et al., 2003) generated a strain expressing hTau (1N4R, P301L). If such a selection towards low expression of hTau (1N4R, P301S) existed, this would imply a unique, strong toxic effect of P301S hTau mutation in *C. elegans*. To investigate this further, we could crossbreed two of the low expressing strains with integration sites located on different chromosomes. Alternatively, we could generate more independent integrated strains, from a different non-integrated strain. All the hTau (1N4R, P301S) strains were integrated from the same progenitor strain, therefore it is possible, that the extrachromosomal array in this strain had fewer copies of the transgene than the other hTau construct variants.

If we ignore hTau expression levels as detected by IHC, we arrive at model 1. This model attributes all differences in performance and performance decline to the genotype alone. Model 1 tells us, that none of the hTau genotypes significantly alters locomotor performance compared to the sterile mutant SS104 which does not express hTau.

4.3.6 Comparison of our Data with Published Work

As summarized in section “C. elegans Models of Tauopathies“ and Table 2, four of the seven reviewed publications assessed the locomotor phenotypes in thrashing assays. Worms are placed in a drop of liquid and the number of body bends are counted during a defined period of time by an observer. The results from each thrashing assay can not be directly compared due to varying assay conditions such as temperature, time until the assay was performed, definition of body bends etc., but we can compare the strains within each report to their respective control and each other. Thrashing rates were extracted as numerical values from published figures and then plotted accordingly (Figure 42).

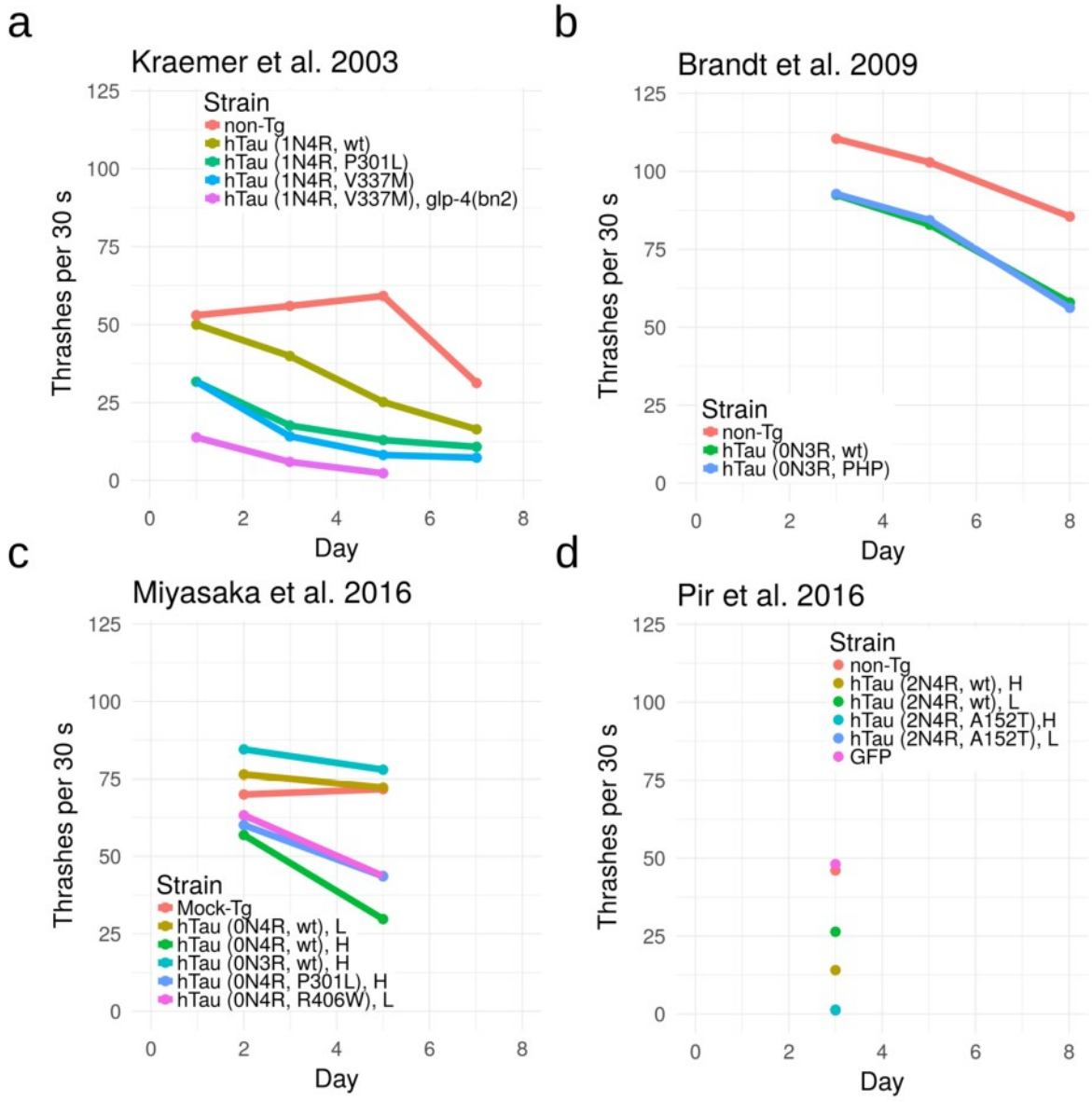

Figure 42: Published Thrashing Rates of hTau-Expressing C. elegans

Thrashing assay data published by Kraemer et al. (Kraemer et al., 2003) (a), Brandt et al. (Brandt et al., 2009) (b), Miyasaka et al. (Miyasaka et al., 2016) (c), and Pir et al. (Pir, Choudhary, Mandelkow, & Mandelkow, 2016) (d). The data were provided as graphs only, therefore the points were extracted using PlotDigitizer (http://plotdigitizer.sourceforge.net) and replotted. Thrashing rates of all strains were adjusted to thrashes per 30 s, day indicates days since hatching. The genotype of the strains is shown in the legend of the respective plot, non-Tg: non transgenic, Mock-Tg: integrated empty vector, H: high expression levels, L: low expression levels.

The published data are in part contradictory. The hTau (0N3R, wt) expressing strain by Brandt et al. (Brandt et al., 2009) performs worse than the non-Tg control while the high expressing hTau (0N3R, wt) strain performs better than the mock-Tg strain by Miyasaka et al. (Miyasaka et al., 2016). Furthermore, low expression of hTau (0N4R, wt) improves thrashing rates over the control whereas high expression of the same wt hTau construct results in reduced performance, being worse than in the mutant hTau-expressing strains. In

Pir et al. (Pir et al., 2016), low expression of hTau (2N4R, wt) thrashes less frequent than the control and high expressing hTau (2N4R, wt) perform worse than low-expressing strains. The effect of 4R hTau expression is reported to depend on expression levels but the functional effect largely differs between the studies. The toxic effect of wt hTau was attributed to an overstabilization of MTs (Brandt et al., 2009). If this is the case, then wt hTau expressing worms should be more tolerant towards MT-destabilizing drugs such as colchicine (Margolis & Wilson, 1977). Wether hTau exerts a stabilizing function on MTs in *C. elegans* was not assessed *in vivo* nor *in vitro*.

Mutated hTau was reported to have a pronounced negative impact on thrashing performance, even at low expression levels and independent of the mutation itself. The mutations P301S/L and V337M lie within the MT binding domains and R406W lies outside the MT repeats. All of these mutant forms were shown to exhibit a decreased MT binding affinity and a decreased MT stabilization ability *in vitro* (Hong, 1998) indicating a possible loss-of-function in carriers of this mutation. Since *C. elegans* does not have a close homologue to hTau, a phenotypic effect of a loss-of-function due to a hTau mutation is unlikely.

The published (Brandt et al., 2009; Kraemer et al., 2003; Miyasaka et al., 2005, 2016; Pir et al., 2016; Xie et al., 2014) as well as our IHC experiments agree, that the phosphorylation profiles of mutated and wt hTau are congruent. Hence, the phosphorylation status is not a distinctive feature of mutated hTau. Furthermore, neither Miyasaka et al. (Miyasaka et al., 2016) nor Pir et al. (Pir et al., 2016) detected detergent insoluble hTau. To date, no pathomechanism of any of these rare familial hTau mutations is known in humans and therefore a possible gain of toxicity of mutated hTau in *C. elegans* remains elusive.

4.3.7 RAPID Recordings of a Published hTau Strain

One of the preexisting mutant strains (Kraemer et al., 2003) expressing hTau (1N4R, V337M) was assessed in two independent RAPID runs (Figure 22). Figure 43 shows the data plotted from both runs.

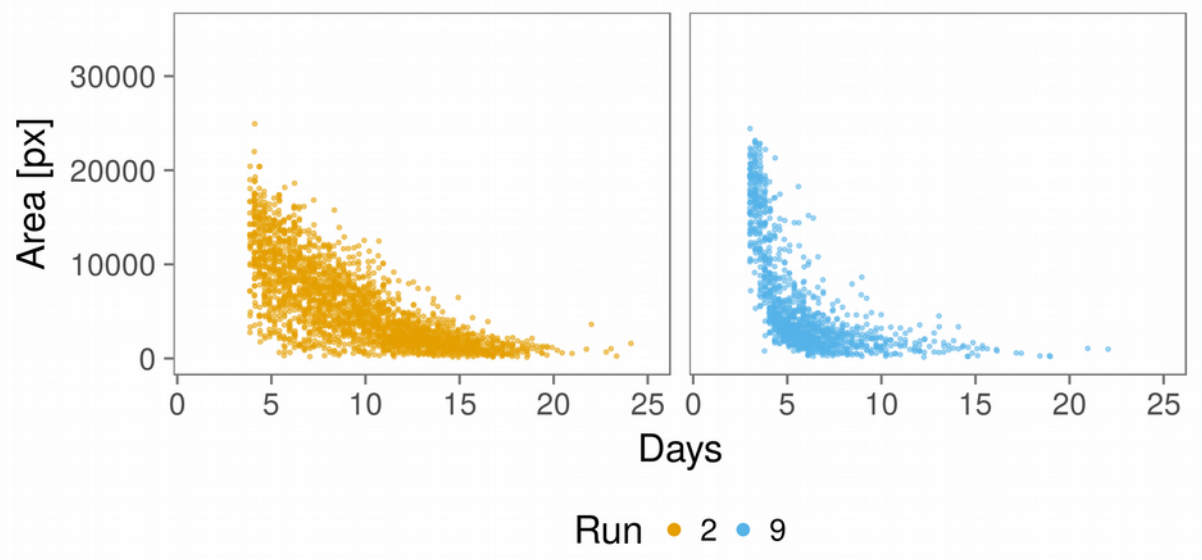

Figure 43: RAPID Recordings of IFP134

Measurements from the strain IFP134 by run. This strain a cross of CK10 (Kraemer et al., 2003) hTau (1N4R, V337M) with SS104 *glp-4(bn2)*, the same strain which is shown in Figure 42 (a).

There is a significant difference between the locomotor performance of the same strain recorded in two different runs, 8 month apart. The differences between the two runs also apparent in their survival curves (Figure 44).

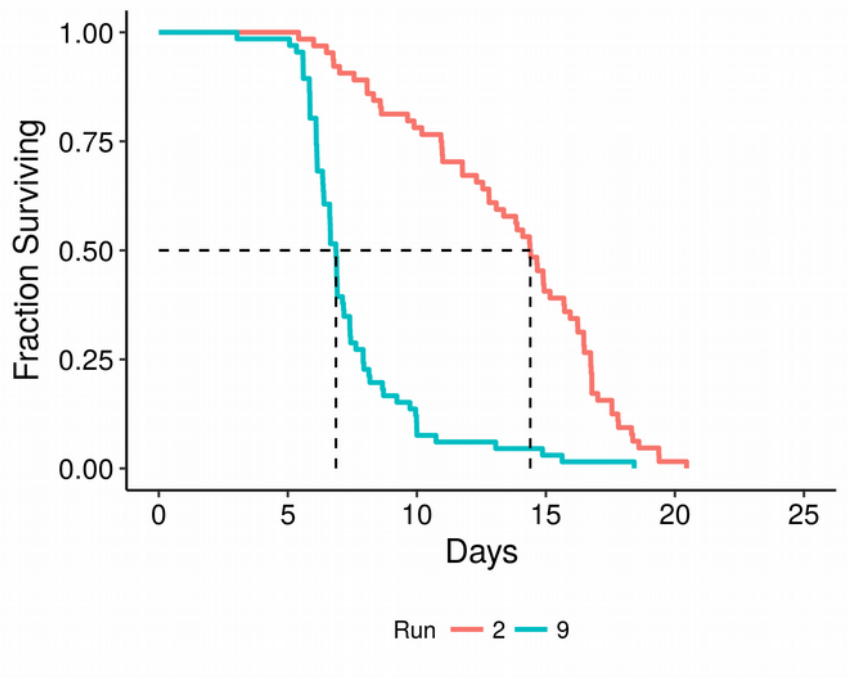

Figure 44: Survival Curves of IFP134

Survival curves of IFP134 recorded in run 2 and in run 9, indicated by colour, dashed line indicates the median survival, which is 14.4 days for run 2 and 6.9 days for run 9.

The observed difference between the two runs of IFP134 is much larger than what we observed otherwise (Figure 29) and therefore might be caused by other factors than discussed before (section “RAPID Sensitivity and Variation Between Runs”). The strain IFP134 recorded in run 2 might have experienced an (epi)genetic drift while in culture before the assay was performed. Epigenetic imprinting was shown to alter the expression of transgenes over several generations (Sha & Fire, 2005). Although we did not generated a worm block for IHC from this particular batch of IFP134, we never observed a reduction in hTau expression in this strain before. To exclude a possible phenotype caused by a bystander mutation due to integration, we could backcross IFP134 several times with N2 wild type. The outcrossed line could then be subjected to a RAPID assay and worm blocks for IHC generated to examine hTau expression levels.

IFP134 recorded in run 2 contains more long-lived individuals which show a slower decline compared to IFP134 recorded in run 9 which primarily consist of short-lived, fast declining individuals. The decline rate observed in run 9 are in agreement with the reported decline in thrashing rates (Figure 42 (a)), although the initial performance is higher than reported (Kraemer et al., 2003).

Furthermore, we recorded the original CK10 strain kindly provided by Kraemer et al. (Kraemer et al., 2003) on plates containing 10 µg/ml FUdR (Figure 28). This strain shows a distinct locomotor performance trajectory, with a steep decline between day 3 and 5 followed by a recovery and a final decrease. Figure 45 shows the individual trajectories of this strain.

Figure 45: Individual Trajectories of CK10

Individual trajectories of CK10 recorded during run 13 on NGM plates containing 10 µg/ml FUdR.

Some of the individuals show the same behaviour as observed in CK10 as a group (Figure 28). An initial decline, followed by a recovery and a final decline until death. This particular pattern does not seem to be an artifact, since the measurements span several days and worms from different strains recorded in the same run do not show this behaviour (Figure 46). Long-term retention of habituation is only achieved in distributed trainings with blocks of repeated stimuli and interstimulus intervals of 60 s (Rose, Kaun, & Rankin, 2002).

Since our measurements are 6.2 h apart, habituation is unlikely and was never observed in any other strain. To test this hypothesis, we could adapt RAPID for habituation experiments.

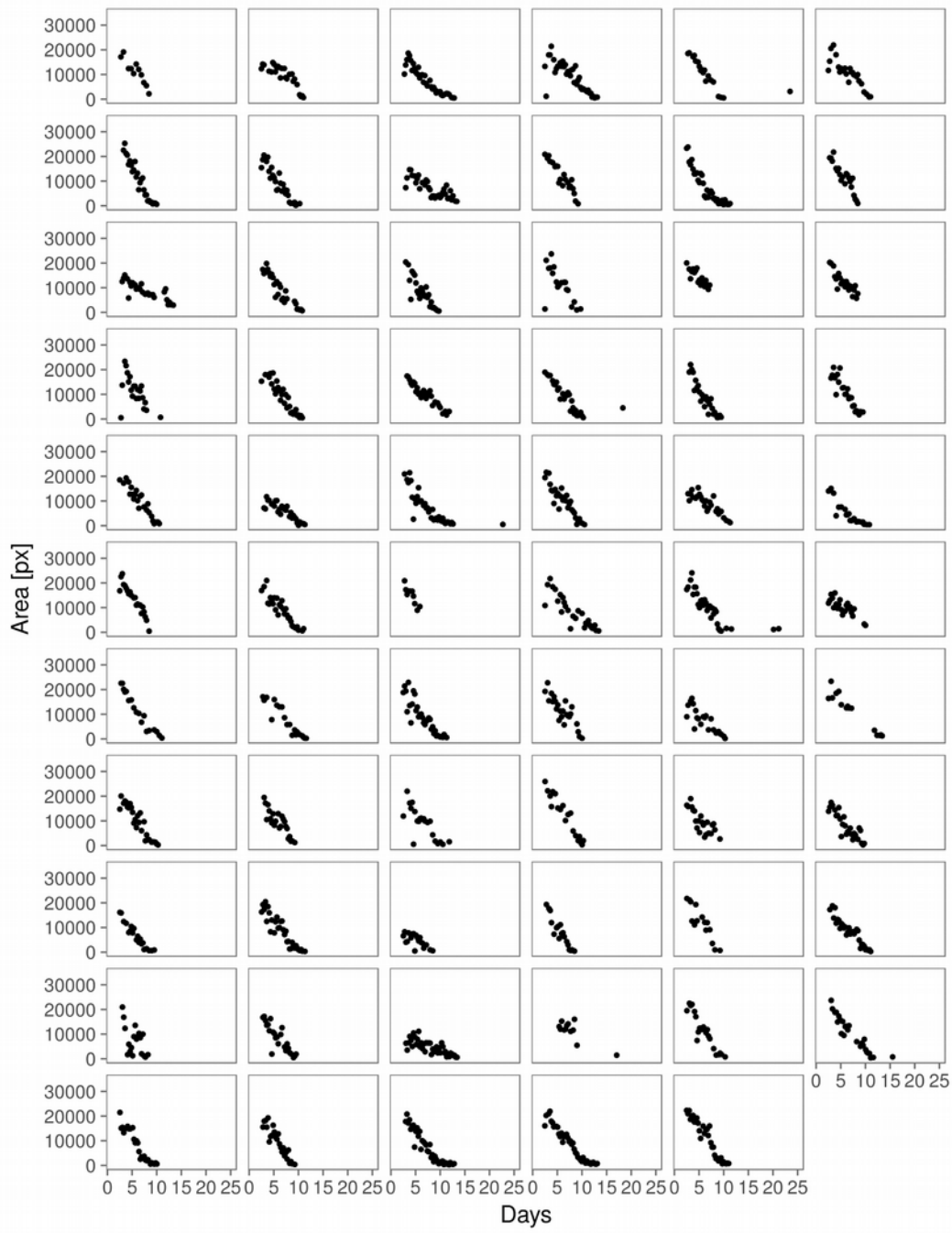

Figure 46: Individual Trajectories from N2

Individual worm plots of the wild type (N2) recorded in run 13 on NGM plates containing 10 µg/ml FUdR.

4.3.8 Generation of Transgenic *C. elegans*

Generation of stable transgenic *C. elegans* strains usually involves the induction of DNA double-strand breaks by UV, X-ray, or ɣ-ray irradiation. This does not only lead to the desired integration of the extrachromosomal array, but also induces mutations and complex rearrangements of the chromosomes (Rosenbluth, Cuddeford, & Baillie, 1985; Stewart, Rosenbluth, & Baillie, 1991). Some of these rearrangements can be removed by outcrossing the integrated strain with wild type. However, mutations and rearrangements of the chromosome affected by the integration can only be removed by recombination with a wild type chromosome during meiosis. Lastly, the site of integration will most likely remain disturbed by the integration of the transgene, which can have a deleterious effect on the resulting strain regardless of the transgene expression itself. Since the integration site is random, the effects of the disruption will conceivably be different for each created strain. To exclude phenotypes caused by the integration event, several independent transgenic strains of the same construct should be studied. We therefore excluded genotypes from the statistical analysis if only one strain was available.

Previously published thrashing assays were mostly conducted on a single transgenic strain per hTau construct, with 10 - 60 worms each (Table 20).

Construct	Integrated	Publication	Strains	Worms	Observations	Observed Time [s]
0N3R, NP	no	1	1	20	3	600
0N3R, PHP	no	1	1	20	3	600
0N3R, wt	no	1	1	20	3	600
0N3R, wt	yes	2	1	60	2	3600
0N4R, P301L	yes	2	1	60	2	3600
0N4R, R406W	yes	2	1	60	2	3600
0N4R, wt	yes	2	2	60	2	7200
1N4R, P301L	yes	3	1	10	4	1200
1N4R, V337M	yes	3	1	10	4	1200
1N4R, wt	yes	3	1	10	4	1200
2N4R, A152T	yes	4	2	30	1	1800
2N4R, wt	yes	4	2	30	1	1800
Total				390	31	27000

Table 20: Summary of Published Observations on hTau-Expressing C. elegans

Number of examined worms per hTau construct, number of observations and total observation time from the published thrashing assays. Multiplying the number of worms with the number of observations and the assay duration (10 - 30 s) results in the total observed time. Publications: 1 = (Brandt et al., 2009), 2 = (Miyasaka et al., 2016), 3 = (Kraemer et al., 2003), 4 = (Pir et al., 2016).

As summarized in Table 21, RAPID enabled us to record functional data of 4 to 13 independent strains per hTau construct, with an unprecedented number of hTau-expressing worms assayed and a total observation time two orders of magnitude larger than what was reported before.

Construct	Strains	Worms	Observations	Observed Time [s]
1N4R, P301S	4	274	5543	166290
1N4R, V337M	13	839	22864	685920
1N4R, wt	6	531	13062	391860
Total		1644	41469	1244070

Table 21: Summary of Observations Recorded Using RAPID

Number of assayed worms per construct, number of observations and total observed time recorded using RAPID. Multiplying the number of worms with the number of observations and the assay duration (30 s) results in the total observed time.

As an alternative to genomic integration via random double-strand breaks, site-directed integration techniques could be employed such as *MosTIC/MosSCI* (Frøkjær-Jensen et al., 2008; Robert, Katic, & Bessereau, 2009). Mobilization of a transposon generates double-strand breaks at defined loci and enables integration of the transgene through homologous repair. More recently, locus-specific integration of transgenes was achieved through the powerful CRISPR/Cas9 system (Yoshina, Suehiro, Kage-Nakadai, & Mitani, 2016). To exclude phenotypes due to developmental defects caused by transgene overexpression during embryogenesis, inducible transgenes could be employed. Temporal control of tissue specific transgene expression was achieved using the FLP recombinase driven by a heat-shock promoter (Davis, Morton, Carroll, & Jorgensen, 2008; Voutev & Hubbard, 2008). Expression of the FLP recombinase excises a transcriptional terminator sequence, leading to permanent expression of the transgene. These newer techniques may help to attribute phenotypes with higher confidence to transgene expression than the traditional method which can be very disruptive.

4.4 References

Allen, B., Ingram, E., Takao, M., Smith, M. J., Jakes, R., Virdee, K., … Goedert, M. (2002). Abundant tau filaments and nonapoptotic neurodegeneration in transgenic mice expressing human P301S tau protein. *The Journal of Neuroscience : The Official Journal of the Society for Neuroscience*, *22*(21), 9340–51. Retrieved from http://www.ncbi.nlm.nih.gov/pubmed/12417659

Brandt, R., Gergou, A., Wacker, I., Fath, T., & Hutter, H. (2009). A Caenorhabditis elegans model of tau hyperphosphorylation: induction of developmental defects by transgenic overexpression of Alzheimer's disease-like modified tau. *Neurobiology of Aging*, *30*(1), 22–33. http://doi.org/10.1016/j.neurobiolaging.2007.05.011

Davis, M. W., Morton, J. J., Carroll, D., & Jorgensen, E. M. (2008). Gene activation using FLP recombinase in C. elegans. *PLoS Genetics*, *4*(3). http://doi.org/10.1371/journal.pgen.1000028

Frøkjær-Jensen, C., Davis, M. W., Hopkins, C. E., Newman, B., Thummel, J. M., Olesen, S., … Jorgensen, E. M. (2008). Single copy insertion of transgenes in C. elegans. *Nat. Genet.*, *40*(11), 1375–1383. http://doi.org/10.1038/ng.248.Single

Gruber, J., Ng, L.F., Poovathingal, S.K., Halliwell, B., 2009. Deceptively simple but simply deceptive - Caenorhabditis elegans lifespan studies: Considerations for aging and antioxidant effects. FEBS Lett. 583, 3377–3387. doi:10.1016/j.febslet.2009.09.051

Hong, M. (1998). Mutation-Specific Functional Impairments in Distinct Tau Isoforms of Hereditary FTDP-17. *Science*, *282*(5395), 1914–1917. http://doi.org/10.1126/science.282.5395.1914

Kraemer, B. C., Zhang, B., Leverenz, J. B., Thomas, J. H., Trojanowski, J. Q., & Schellenberg, G. D. (2003). Neurodegeneration and defective neurotransmission in a Caenorhabditis elegans model of tauopathy. *Proceedings of the National Academy of Sciences of the United States of America*, *100*(17), 9980–5. http://doi.org/10.1073/pnas.1533448100

Lucanic, M., Plummer, W. T., Chen, E., Harke, J., Foulger, A. C., Onken, B., … Phillips, P. C. (2017). Impact of genetic background and experimental reproducibility on identifying chemical compounds with robust longevity effects. *Nature Communications*, *8*, 14256. http://doi.org/10.1038/ncomms14256

Margolis, R. L., & Wilson, L. (1977). Addition of colchicine-tubulin complex to microtubule ends: the mechanism of substoichiometric colchicine poisoning. *Proceedings of the National Academy of Sciences of the United States of America*, *74*(8), 3466–3470. http://doi.org/10.1073/pnas.74.8.3466

Mello, C. C., Kramer, J. M., Stinchcomb, D., & Ambros, V. (1991). Efficient gene transfer in C.elegans: extrachromosomal maintenance and integration of transforming sequences. *EMBO Journal*, *10*(12), 3959–70. http://doi.org/10.1016/0168-9525(92)90342-2

Miyasaka, T., Ding, Z., Gengyo-Ando, K., Oue, M., Yamaguchi, H., Mitani, S., & Ihara, Y. (2005). Progressive neurodegeneration in C. elegans model of tauopathy. *Neurobiology of Disease*, *20*(2), 372–383. http://doi.org/10.1016/j.nbd.2005.03.017

Miyasaka, T., Xie, C., Yoshimura, S., Shinzaki, Y., Yoshina, S., Kage-Nakadai, E., … Ihara, Y. (2016). Curcumin improves tau-induced neuronal dysfunction of nematodes. *Neurobiology of Aging*, *39*, 69–81. http://doi.org/10.1016/j.neurobiolaging.2015.11.004

Pir, G. J., Choudhary, B., Mandelkow, E., & Mandelkow, E.-M. (2016). Tau mutant A152T, a risk factor for FTD/PSP, induces neuronal dysfunction and reduced lifespan independently of aggregation in a C. elegans Tauopathy model. *Molecular Neurodegeneration*, *11*(1), 33. http://doi.org/10.1186/s13024-016-0096-1

Podshivalova, K., Kerr, R. A., & Kenyon, C. (2017). How a Mutation that Slows Aging Can Also Disproportionately Extend End-of-Life Decrepitude. *Cell Reports*, *19*(3), 441–450. http://doi.org/10.1016/j.celrep.2017.03.062

Robert, V. J. P., Katic, I., & Bessereau, J. L. (2009). Mos1 transposition as a tool to engineer the Caenorhabditis elegans genome by homologous recombination. *Methods*, *49*(3), 263–269. http://doi.org/10.1016/j.ymeth.2009.02.013

Rose, J. K., Kaun, K. R., & Rankin, C. H. (2002). A New Group-Training Procedure for Habituation Demonstrates That Presynaptic Glutamate Release Contributes to Long-Term Memory in Caenorhabditis elegans. *Learning & Memory*, *9*(3), 130–137. http://doi.org/10.1101/lm.46802

Rosenbluth, R. E., Cuddeford, C., & Baillie, D. L. (1985). Mutagenesis in Caenorhabditis elegans. II. A spectrum of mutational events induced with 1500 r of gamma-radiation. *Genetics*, *109*(3), 493–511.

Sha, K., & Fire, A. (2005). Imprinting capacity of gamete lineages in Caenorhabditis elegans. *Genetics*, *170*(4), 1633–1652. http://doi.org/10.1534/genetics.104.040303

Stewart, H. I., Rosenbluth, R. E., & Baillie, D. L. (1991). Most ultraviolet irradiation induced mutations in the nematode Caenorhabditis elegans are chromosomal rearrangements. *Mutation Research*, *249*(1), 37–54. Retrieved from http://www.ncbi.nlm.nih.gov/pubmed/2067542

Stroustrup, N., Ulmschneider, B. E., Nash, Z. M., López-Moyado, I. F., Apfeld, J., & Fontana, W. (2013). The Caenorhabditis elegans Lifespan Machine. *Nature Methods*, *10*(7), 665–70. http://doi.org/10.1038/nmeth.2475

Swierczek, N. A., Giles, A. C., Rankin, C. H., & Kerr, R. A. (2011). High-throughput behavioral analysis in C. elegans. *Nature Methods*, *8*(7), 592–598.

Uchihara, T. (2007). Silver diagnosis in neuropathology: principles, practice and revised interpretation. *Acta Neuropathologica*, *113*(5), 483–99. http://doi.org/10.1007/s00401-007-0200-2

Voutev, R., & Hubbard, E. J. A. (2008). A “FLP-out” system for controlled gene expression in Caenorhabditis elegans. *Genetics*, *180*(1), 103–119. http://doi.org/10.1534/genetics.108.090274

Xie, C., Miyasaka, T., Yoshimura, S., Hatsuta, H., Yoshina, S., Kage-Nakadai, E., … Ihara, Y. (2014). The homologous carboxyl-terminal domains of microtubule-associated protein 2 and Tau induce neuronal dysfunction and have differential fates in the evolution of neurofibrillary tangles. *PLoS ONE*, *9*(2). http://doi.org/10.1371/journal.pone.0089796

Yoshina, S., Suehiro, Y., Kage-Nakadai, E., & Mitani, S. (2016). Locus-specific integration of extrachromosomal transgenes in C. elegans with the CRISPR/Cas9 system. *Biochemistry and Biophysics Reports*, *5*, 70–76. http://doi.org/10.1016/j.bbrep.2015.11.017

Zhang, W. B., Sinha, D. B., Pittman, W. E., Hvatum, E., Stroustrup, N., & Pincus, Z. (2016). Extended Twilight among Isogenic C. elegans Causes a Disproportionate Scaling between Lifespan and Health. *Cell Systems*, *3*(4), 333–345.e4. http://doi.org/10.1016/j.cels.2016.09.003

Zhao, Y., Gilliat, A. F., Ziehm, M., Turmaine, M., Wang, H., Ezcurra, M., … Gems, D. (2017). Two forms of death in ageing Caenorhabditis elegans. *Nature Communications*, *8*(May), 15458. http://doi.org/10.1038/ncomms15458

Zheng-Fischhöfer, Q. (1998). Sequential phosphorylation of Tau by glycogen synthase kinase-3β and protein kinase A at Thr212 and Ser214 generates the Alzheimer-specific epitope of antibody. *European Journal of Biochemistry*, *552*, 542–552. Retrieved from http://onlinelibrary.wiley.com/doi/10.1046/j.1432-1327.1998.2520542.x/full

5 Conclusion

5.1 RAPID - A Novel Tool to Study Neurodegeneration, Ageing, and Health

With RAPID we developed a novel tool to study lifelong stimulated locomotor performance of single worms, enabling longitudinal studies of worm health under various conditions. RAPID consists of a series of independent imaging platforms with script-enabled consumer-grade cameras, a software pipeline for the extraction of locomotor data, a statistical framework for analysis and a robotic plate changing mechanism. Our modular design entirely relies on open source software enabling other researchers to adapt and extend the RAPID platform for their purposes. Archival of the imaging data enables retrospective analysis and extraction of additional locomotor parameters.

In contrast to existing worm trackers, RAPID enables high-throughput, single worm recordings on standard NGM plates. Measuring stimulated locomotor performance allows assessment of worm health instead of focussing on time to death or lifespan as a read-out. Lifespan-extending interventions are not desireable if they do not increase the amount of time that is spent in good health. In a proof-of-principle experiment we demonstrated that RAPID is able to determine the locomotor performance of long-lived and uncoordinated worm strains and how they compare to the wild type strain. None of the long-lived strains showed a better performance than the wild type, indicating that this kind of life extension does not improve healthy ageing.

5.2 *C. elegans* as Model of Tauopathy

We generated 23 genomically integrated *C. elegans* strains expressing either wild type or mutated hTau in the nervous system to evaluate the possible toxic effect of hTau and neurodegeneration. To estimate the expression levels and determine the phosphorylation status of hTau, we developed a synthetic tissue which we termed worm block, enabling conventional histology and immunohistochemistry on a large number of synchronized worm populations. Worm blocks allow the use of automated tissue processing techniques and autostainer platforms for high throughput histology which also ensure reproducibility across replicates.

IHC on our newly generated worm strains demonstrated, that the expression levels vary. In accordance with published work, phosphorylation at the two epitopes examined is not a unique feature of mutated hTau but is also found in wild type hTau-expressing strains. Phosphorylation of one epitope correlates with the amount of total hTau expression.

To test whether hTau expression in *C. elegans* is neurotoxic, we examined our strains in a lifelong stimulated locomotor performance test using RAPID. The data show considerable variation among individual animals within any given strain. This variation is in part caused by the stochastic nature of the ageing process itself. All strains show distinct decline trajectories, but there is no acknowledgeable difference between the hTau genotypes and the non-transgenic control. For statistical evaluation, we constructed a linear mixed-effect model which contains hTau genotype as a fixed effect. All strains with a given genotype are grouped and compared to the reference strain. The fixed effect for *genotype* does not significantly change the baseline performance nor does it affect the rate of decline, indicating that hTau does not have an effect on stimulated locomotor performance.

Since our IHC experiments revealed different expression levels among the hTau-expressing strains, we classified them into hTau positive (labelling), and hTau negative (no labelling). In analogy to the first model, we grouped all strains with labelling and compared them to the group with no labelling. The fixed effect *labelling* does not significantly change the baseline performance. However, the effect of hTau labelling on the rate of decline is significant but small, leading to a slightly slower decline in hTau positive worms. The model also includes a fixed effect for *genotype*, which decreases the baseline performance of the two mutant hTau constructs, but not of the wild type hTau. This outcome can be partially attributed to how the groups are composed. One mutant hTau genotype contains lower performing strains with no labelling, while the wild type hTau genotype consists of strains with labelling. To definitely determine how expression levels affect the locomotor performance of different hTau genotypes, all combinations of labelling and genotype need to be available for testing.

Our data disagrees with the published literature on the reported deleterious effects of hTau expression in *C. elegans*. In contrast to earlier reports, we generated and analysed 4, 6, and 13 independent strains per hTau genotype and examined several hundred worms using lifelong longitudinal recordings, outnumbering all previous observations combined. Our data indicate that neither mutant nor wild type hTau expression leads to a pronounced locomotor phenotype, arguing against a previously postulated, toxic effect of neuronal hTau expression.

6 Outlook

6.1 RAPID - Improvements and Additions

RAPID is a stable and reliable platform on which experiments can run for several week without experimenter interventions. Nonetheless, RAPID consists of mechanical parts which are in constant use and therefore will wear out over time. These parts include the camera's moving lenses, a relay switching the vacuum pump, the pump itself and the attached electromagnetic valve. Failure of one camera will lead to missing data on 1/4 of the plates recorded. Once the faulty camera is identified, it can be easily replaced with only a short interruption. Due to missing redundancy, failures in the vacuum system are more critical. Plates can be dropped, flipped and switched in position. Since each plate is labelled with a unique identifier and plate position, the plates can always be put back to their designated position. Possible switching of plates can be detected and in most cases also corrected, since each plate has unique track patterns in the *E. coli* lawn, produced by the moving worm. If unambiguous identification is not possible, the corresponding data sets are censored. In the current implementation, RAPID does not have sensors to detect plate pick up errors due to a failure in the vacuum pick-up system. A sensor at the calibration position could be used to detect the presence of a plate and report it back to the host computer. In case of a missing plate, the assay could be interrupted and the operator notified to prevent error propagation due to switched plates etc.

The light sources are conventional incandescent halogen light bulbs due to a constant brightness and homogeneity of the illumination. Recently, we switched to LEDs with comparable light characteristics which we are currently evaluating. LEDs are desirable since they emit less heat. To improve the imaging quality of RAPID further, we could replace the magnifying lens assembly with an achromatic lens. As discussed in section "Discussion", the current lenses have spherical- and chromatic aberrations, which leads to blurred tracks near the edge of the field of view. Furthermore, the construction material used for the frame which holds the imaging platforms, diffuser and light sources is made of plywood and wooden boards, since it is easy to work with and does not require specialized tools. Ideally, the next version of the frame will be made of extruded aluminium to make the structure more rigid.

To improve the temperature stability during our experiments, we should separate the heat generating components such as the robot controller from the assay compartment. Additional installation of a small air conditioning unit may stabilize the temperature at 25 °C. Due to the arrangement of the imaging platforms and the plate storage array, it is not possible to enclose the plates of the storage array in a temperature controlled cabinet.

For optogenetics experiments, a secondary light source could be coupled to the imaging system using a dichroic mirror/beamsplitter. Alternatively, a second excitation illumination ring could be installed around the light source. Since stimulation with the vibratory stimulus worked reliably, we have not yet tested any of these potential implementations.

As with the hardware, our software was designed to work robustly with our assay conditions. For this reason we compare the area covered by the worm. Ideally, we would like to compare

the track length instead which is independent of the worm body size and changes therein during life. Skeletonization is the operation which reduces a given area/contour to a line of one pixel width. Counting the number of pixels results in the length of the track. In addition, the general shape of the track is preserved. Initial tests using skeletonization were not satisfactory, since it produced artifacts such as branching, falsely increasing track length. This can be improved by employing pruning to remove branches. An attractive contestant to skeletonization would be to fit a B-spline along the medial axis of a track area, thereby avoiding the possibility of branching. Having a line representation of a track would further enable the extraction of features beside length, such as amplitude, wavelength, bending angles etc., which are currently not quantifiable. We aim to evaluate the worm detection algorithm employed by the Multi-Worm Tracker, combining image subtraction with flood-fill operation to detect worm outlines. Since RAPID preserves all raw image data, we can evaluate new tracking algorithms on our large data set and compare their performance. However, extracting additional locomotor parameters will require different means of statistical analyses. It is not apparent, how parameters such as bending angles can be compared, or even become meaningless once sinusoidal movement ceases.

6.2 RAPID - Additional Experiments

We will continue to use RAPID in the study of ageing, performing more experiments on long-lived mutants and life prolonging interventions. Moreover, we will address the issues raised by the reviewers and revise our manuscript on RAPID accordingly. RAPID can furthermore be employed to study the effect of compounds on health and ageing. Since the system is capable to deal with NGM plates containing living bacteria, we might test the system's capability as a platform for functional RNAi screening by feeding RNAi expressing bacteria.

6.3 Worm Blocks as Synthetic Reference Tissue

We envisage the use of our worm block technique for use in routine diagnostics as reference tissue for IHC and molecular pathology. Proteins or short peptides containing an epitope could be expressed in the pharynx, a structure which can be readily identified in longitudinal- and transversal sections. By generating several strains with varying expression levels, the reference tissue can be selected to optimally cover the detection range of a given diagnostic test. Similar attempts were made by creating artificial tissues from cell cultures. However, *C. elegans* is less challenging in cultivation, and requires no special equipment nor expensive culturing media. The use of worm blocks as reference tissue is not limited to antigen expression, but can also be used for DNA-based assays by incorporation of specific DNA sequences. In particular, distribution of engineered reference *C. elegans* strains is simpler than distribution of cell cultures, which could aid in standardization across molecular diagnostic pathology laboratories.

6.4 *C. elegans* as Model System of Tauopathies

To further study the effect of expression of hTau on locomotor performance, it would be helpful to create new sets of hTau expressing strains with all combinations of hTau genotype and expression levels. Instead of focusing on overall performance, more subtle change in locomotion could be detected by extracting additional locomotor parameters. To avoid bystander mutations and phenotypes due to random integration, site-directed insertion method should be employed. This would make strains with different hTau genotypes more comparable as with conventional genomic integration, since they would have a more uniform genetic background. To avoid phenotypes, hTau expression could also be made inducible. Instead of using non-transgenic worms as control, strains with a scrambled copy of the hTau constructs should be employed. Lastly, phenotypic scoring should be carried out using automated systems, allowing unbiased and experimenter-independent observations.

7 Appendix

7.1 List of Primers and Constructs

Region	Name	Sequence (5’ - 3’)
Promoter	mec-7p_fwd	GAGCTTTCAACACCCCGCAC
	mec-7p_MAPT_rev	tcctggcggggctcagcCATGTTGCTTGAAATTTGGACCCGA
	aex-3p-.1.3_fwd	TGCCGCTTCAATTCTCCATGTG
	aex-3p_MAPT_rev	tcctggcggggctcagcCATTTTTTATTAGGATAGGTACATTGGTGCA
	aex-3p_GFP_rev	ctccagtgaaaagttcttctcctttactCATTTTTTATTAGGATAGGTACATTGGTGC
	mec-7p_DsRed2_rev	gatgacgttctcggaggaggcCATGTTGCTTGAAATTTGGACCCGA
3'-UTR	MAPT_unc-86-UTR_fwd	tggccaagcagggtttgtgaTTTCGTTTTCGTGAACACATTTTCCC
	unc-86-UTR_fwd	GGCGGGTTAACAAGCAGGTC
	unc-86_nested_rev	ACACTATGCAAGCATCAATCGCC
	GFP_unc-86_fwd	cacatggcatggatgaactatacaaatagTTTCGTTTTCGTGAACACATTTTCCC
	DsRed2_unc-86_fwd	cgccaccacctgttcctgtagTTTCGTTTTCGTGAACACATTTTCCC
MAPT	MAPT_fwd	gctgagccccgccagga
	MAPT_rev	tcacaaaccctgcttggcca
GFP	GFP_fwd	agtaaaggagaagaacttttcactggag
	GFP_rev	ctatttgtatagttcatccatgccatgtg
DsRed2	DsRed2_fwd	gcctcctccgagaacgtcatc
	DsRed2_rev	ctacaggaacaggtggtggcg
Sequencing	MAPT_nested_fwd	TGCCCATGCCAGACCTGAA
	mec-7p_150bp_upstream_fwd	GATGGGGCACCGAGATGTG
	aex-3p_200bp_upstream_fwd	TTGTAATCTATCATGTAAACAGTTACAC
	unc-86_150bp_downstream_rev	CTTGTCGCTAAAAATGTTGAGGAAC
	MAPT_mid_rev	TGTGGCGATCTTCGTTTTACCAT
Mutagenesis	V337M_fwd	GAGGTGGCCAGATGGAAGTAAA
	V337M_rev	TTTACTTCCATCTGGCCACCTC
	V337M_no1_fwd	GGTGGCCAGATGGAAGTAAAATCTGAGAA
	V337M_no1_rev	ACTTCCATCTGGCCACCTCCTGGTTTAT
	P301S_no1_fwd	CAAACACGTCTCGGGAGGCGGC
	P301S_no1_rev	CCTCCCGAGACGTGTTTGATATTATCCTTTGAG

Table 22: Primer Seqeunces

Primer 1	Primer 2	Template	Product
mec-7p_fwd	mec-7p_MAPT_rev	N2 genomic	mec-7p_MAPT
mec-7p_fwd	mec-7p_DsRed2_rev	N2 genomic	mec-7p_DsRed2
aex-3p-.1.3_fwd	aex-3p_MAPT_rev	N2 genomic	aex-3p_MAPT
aex-3p-.1.3_fwd	aex-3p_GFP_rev	N2 genomic	aex-3p_GFP
MAPT_fwd	MAPT_rev	prk172 (1N4R)	MAPT
MAPT_fwd	V337M_rev	prk172 (1N4R)	V337M(5')
V337M_fwd	MAPT_rev	prk172 (1N4R)	V337M(3')
GFP_fwd	GFP_unc-86_fwd	OH4134 genomic	GFP_unc-86-UTR
DsRed2_fwd	DsRed2_unc-86_fwd	OH4134 genomic	DsRed2_unc-86-UTR
MAPT_unc-86-UTR_fwd	unc-86_nested_rev	N2 genomic	MAPT_unc-86-UTR
GFP_unc-86_fwd	unc-86_nested_rev	N2 genomic	GFP_unc-86-UTR
DsRed2_unc-86_fwd	unc-86_nested_rev	N2 genomic	DsRed2_unc-86-UTR
aex-3p-1.3_fwd	MAPT_rev	aex-3p_MAPT + MAPT	aex-3p::MAPT
aex-3p-1.3_fwd	GFP_rev	aex-3p_GFP + GFP	aex-3p::GFP
mec-7p_fwd	DsRed2_rev	mec-7p_GFP + DsRed2	mec-7p::DsRed2
mec-7p_fwd	V337M_rev	mec-7p_MAPT + V377M(5')	mec-7p::V337M(5')
MAPT_fwd	unc-86_nested_rev	MAPT + MAPT_unc-86-UTR	MAPT::unc-86_UTR
GFP_fwd	unc-86_nested_rev	GFP + GFP_unc-86-UTR	GFP::unc-86-UTR
DsRed2_fwd	unc-86_nested_rev	DsRed2 + DsRed2_unc-86-UTR	DsRed2::unc-86-UTR
V337M_fwd	unc-86_nested_rev	V337M(3') + MAPT_unc-86-UTR	V337M(3')::unc-86-UTR
aex-3p-1.3_fwd	unc-86_nested_rev	aex-3p::MAPT + MAPT::unc-86_UTR	aex-3p::MAPT::unc-86_UTR
aex-3p-1.3_fwd	unc-86_nested_rev	aex-3p::GFP + GFP::unc-86-UTR	aex-3p::GFP::unc-86_UTR
mec-7p_fwd	unc-86_nested_rev	mec-7p::V337M(5') + V337M(3')::unc-86-UTR	mec-7p::V337M::unc-86_UTR
mec-7p_fwd	unc-86_nested_rev	mec-7p::DsRed2 + DsRed2::unc-86-UTR	mec-7p::DsRed2::unc-86_UTR

Table 23: Amplifications for DNA constructs

Combination of primers and templates used to generate the constructs. The final amplicons were ligated into the pCR 2.1-TOPO TA vector as described in section “Plasmid Construction and Generation of Transgenic Worm Lines”.

7.2 List of Strains and Genotypes

Strain	Allele(s)	Tau Construct	Genotype	Source
N2		no Tau		CGC
SS104	*bn2*		*glp-4(bn2)*	CGC
IFP177	*bn2; juIs76*		*unc-25p*::*gfp* + *lin-15(+)*; *glp-4(bn2)*	
IFP147	*npbIs12*		*aex-3p*::*gfp*::*unc-86*UTR + *mec-7p*::*dsRed*::*unc-86*UTR	
IFP42	*npbIs1*	hTau (1N4R, wt)	*aex-3*p::*gfp*::*unc-86*UTR + *aex-3p*::hTau(1N4R, wt)::*unc-86*UTR	
IFP141	*npbIs16; bn2*		*aex-3p*::*gfp*::*unc-86*UTR + *aex-3p*::hTau(1N4R, wt)::*unc-86*UTR; *glp-4(bn2)*	
IFP142	*npbIs18; bn2*			
IFP144	*npbIs19; bn2*			
IFP148	*npbIs15; bn2*			
IFP224	*npbIs2; bn2*			
IFP225	*npbIs1; bn2*			
IFP195	*npbIs24; bn2*	hTau (1N4R, P301S)	*aex-3p*::*gfp*::*unc-86*UTR + *aex-3p*::hTau(1N4R, P301S)::*unc-86*UTR	
IFP199	*npbIs31; bn2*			
IFP222	*npbIs43; bn2*			
IFP223	*npbIs42; bn2*			
IFP134	*bkIs10; bn2*	hTau (1N4R, V337M)	*aex-3p*::hTau(1N4R, V337M)::*unc-54*UTR + *myo-2p::gfp; glp-4(bn2)*	
IFP143	*bkIs10; bn2; juIs76*		*aex-3p*::hTau(1N4R, V337M)::*unc-54*UTR + *myo-2p::gfp*; *glp-4(bn2)*; *unc-25p::gfp* + *lin-15(+)*	
IFP187	*npbIs28; bn2*	hTau (1N4R, V337M)	*aex-3p*::*gfp*::*unc-86*UTR + *aex-3p*::hTau(1N4R, V337M)::*unc-86*UTR; *glp-4(bn2)*	
IFP191	*npbIs26; bn2*			
IFP196	*npbIs30; bn2*			
IFP197	*npbIs33; bn2*			
IFP200	*npbIs25; bn2*			
IFP208	*npbIs27; bn2*			
IFP211	*npbIs23; bn2*			
IFP212	*npbIs29; bn2*			
IFP213	*npbIs37; bn2*			
IFP214	*npbIs39; bn2*			
IFP217	*npbIs32; bn2*			
IFP218	*npbIs35; bn2*			
IFP220	*npbIs36; bn2*			
CK10	*bkIs10*	hTau (1N4R, V337M)	*aex-3p*::hTau(1N4R, V337M)::*unc-54*UTR	*Kraemer et al.*
FX10646	*tmIs110; su1006*	hTau (0N3R, wt)	mec-7p::hTau(0N3R, wt)::unc-86UTR; rol-6(su1006)	*Mitani et al.*
FX10519	*tmIs82; su1006*	hTau (0N4R, wt)	*mec-7p*::hTau(0N4R, wt)::*unc-86*UTR; *rol-6(su1006)*	
FX11152	*tmIs81; su1006*	hTau (0N4R, P301L)	*mec-7p*::hTau(0N4R, P301L)::unc-86UTR; *rol-6(su1006)*	
FX12012	*tmIs146; su1006*	hTau (0N4R, R406W)	*mec-7p*::hTau(0N4R, R406W)::unc-86UTR; *rol-6(su1006)*	

Strain	Allele(s)	Tau Construct	Genotype	Source
VH255	*hdEx82; e2123*	hTau (0N3R, wt)	*rgef-1p*::hTau(0N3R, wt) + *pha-1(+)*; *pha-1(e2123)*	Hutter et al.
VH254	*hdEx81; e2123*	hTau (0N3R, PHP)	*rgef-1p*::hTau(0N3R, PHP) + *pha-1(+); pha-1(e2123)*	
VH420	*hdEx180; e2123*	hTau (0N3R, NP)	*rgef-1p*::hTau(0N3R, NP) + *pha-1(+)*; *pha-1(e2123)*	

Table 24: Strains, Allels and Genotypes

List of all the strains and genotypes used in this work. Duplicate hTau constructs and genotypes are omitted, strains without source reference were created by us.

7.3 Diagnostic Plots of Models 1 and 2

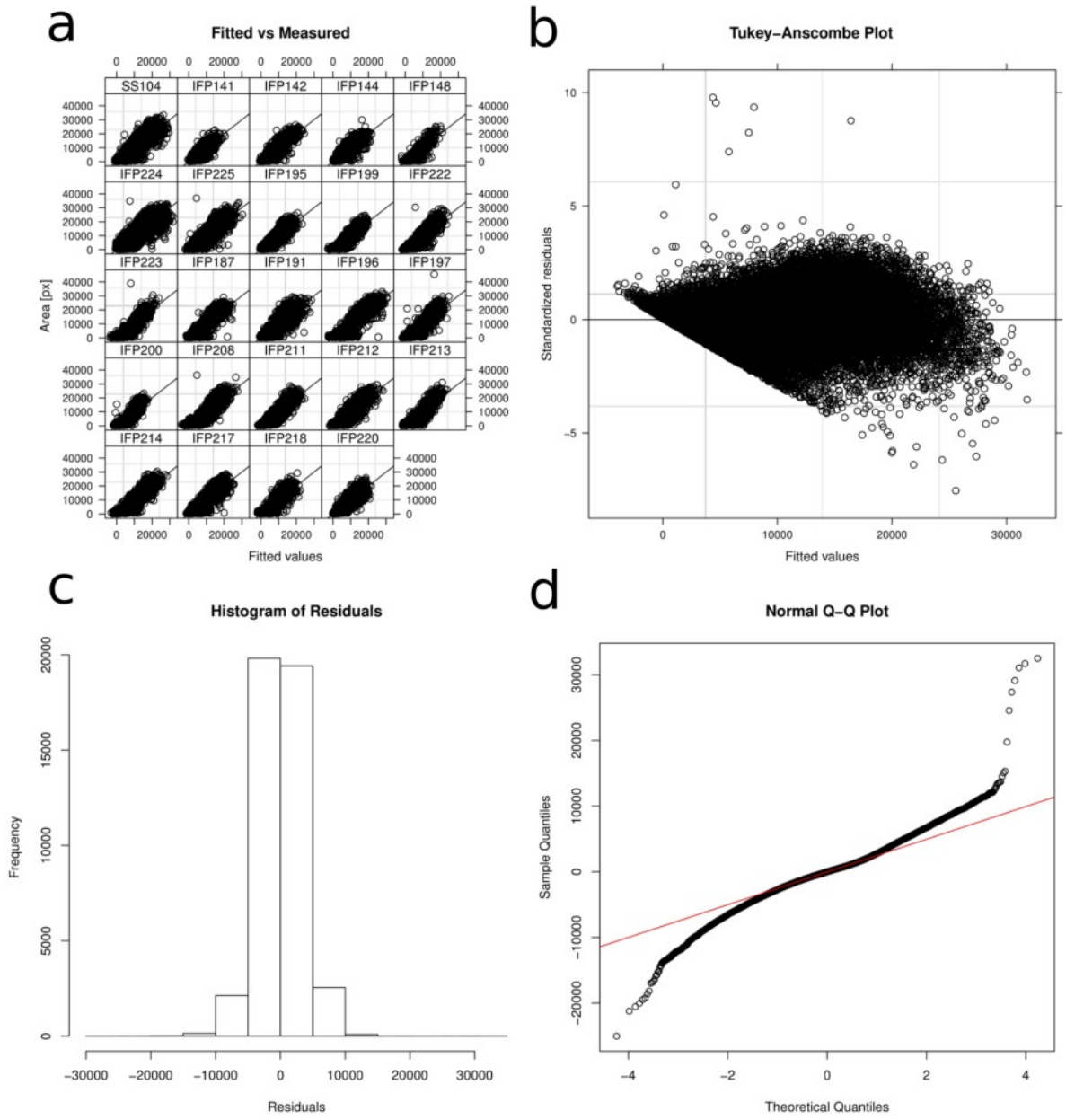

Figure 47: Diagnostic Plots for Model 1

Diagnostic plots of all strains recorded using RAPID. Measured vs. predicted area (a) same as in Figure 26, Tukey-Anscombe plot (b), histogram of residuals (c), and normal Q-Q- plot of residuals (d).

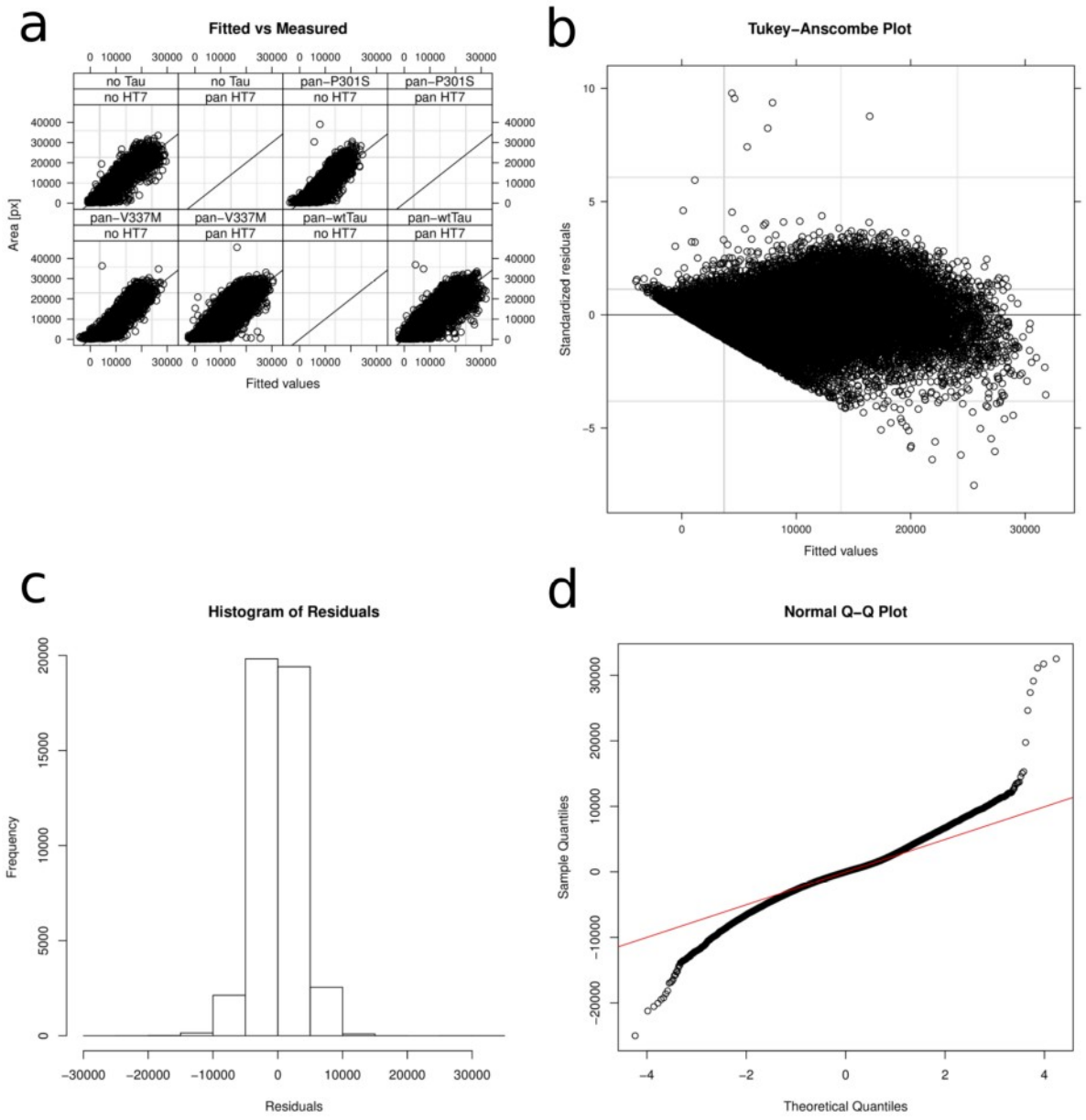

Figure 48: Diagnostic Plots of Model 2

Diagnostic plots of all strains recorded using RAPID. Measured vs. predicted area (a) same as in Figure 27, Tukey-Anscombe plot (b), histogram of residuals (c), and normal Q-Q- plot of residuals (d).

7.4 RAPID - Image Processing and Censoring

Once the imaging of a plate is complete, the images are downloaded to the host computer and compressed into a video. Data from each recording is saved into a folder together with additional metadata. A demon running in the background constantly checks for new videos and performs the image processing with track extraction. Figure 49 shows the results of the image subtraction and track extraction.

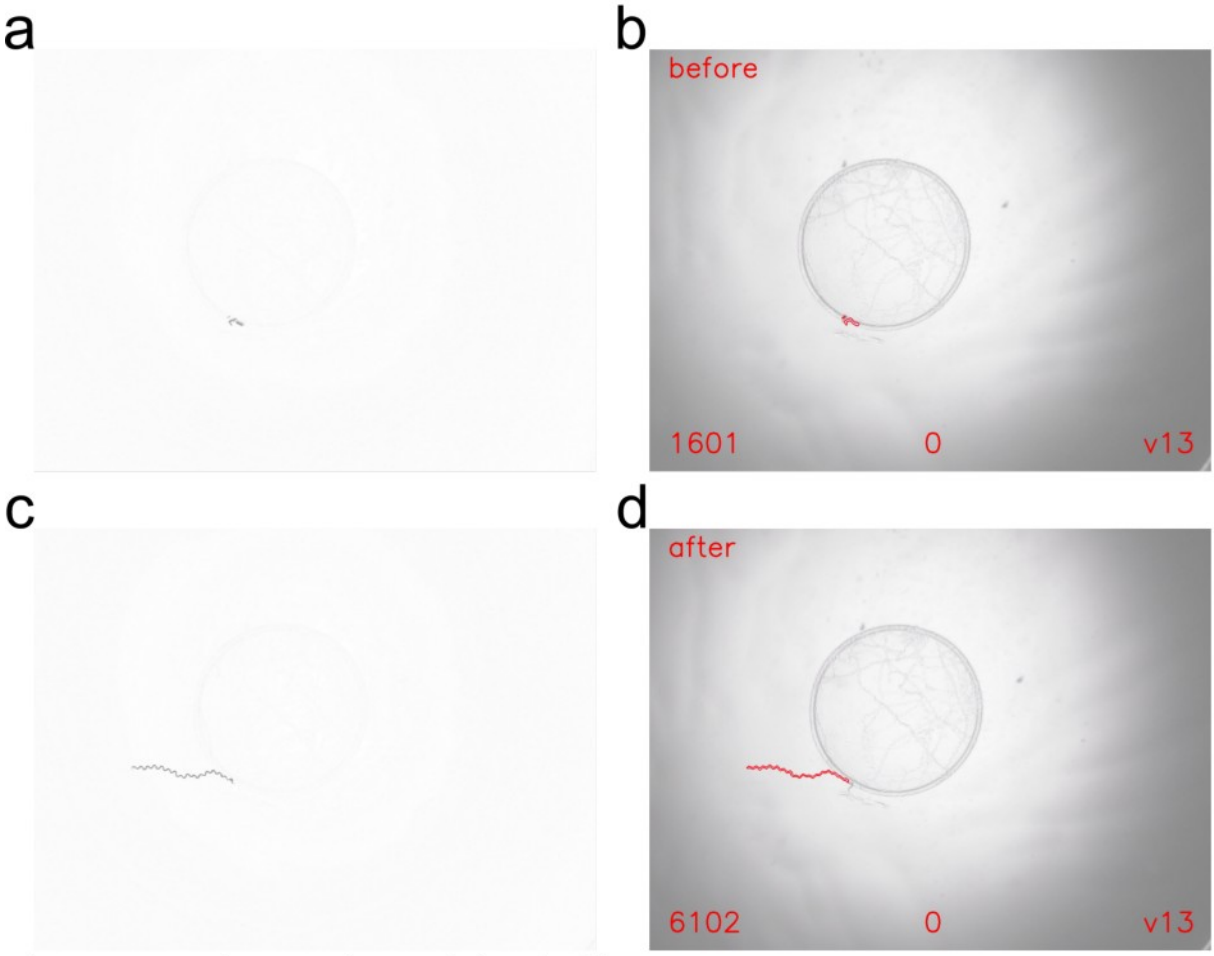

Figure 49: Track Extraction and Thresholding

Image processing of RAPID data. Image subtraction of images recorded before (a), and after the vibratory stimulus (b) leads to an image showing only pixel which have changed, i.e. the worm track. The track area is extracted from these images using adaptive thresholding. The result is overlaid onto the first image of the series along with indication of the period, before (b) or after the stimulus (d). The area in pixels (bottom left), track is censored due to the worm being too close to the edge of the image (middle), and the version of the image processing pipeline (bottom right corner) are indicated. All timepoints of a given worm are compiled into a mosaic, visually inspected and censored if the thresholding failed. For this work we only analysed the track area recorded after the vibratory stimulus.

After the track area has been extracted and the overlays generated, all timepoints are assembled into a large mosaic for each worm. These mosaics are then visually inspected and individual timepoints are censored (Figure 50).

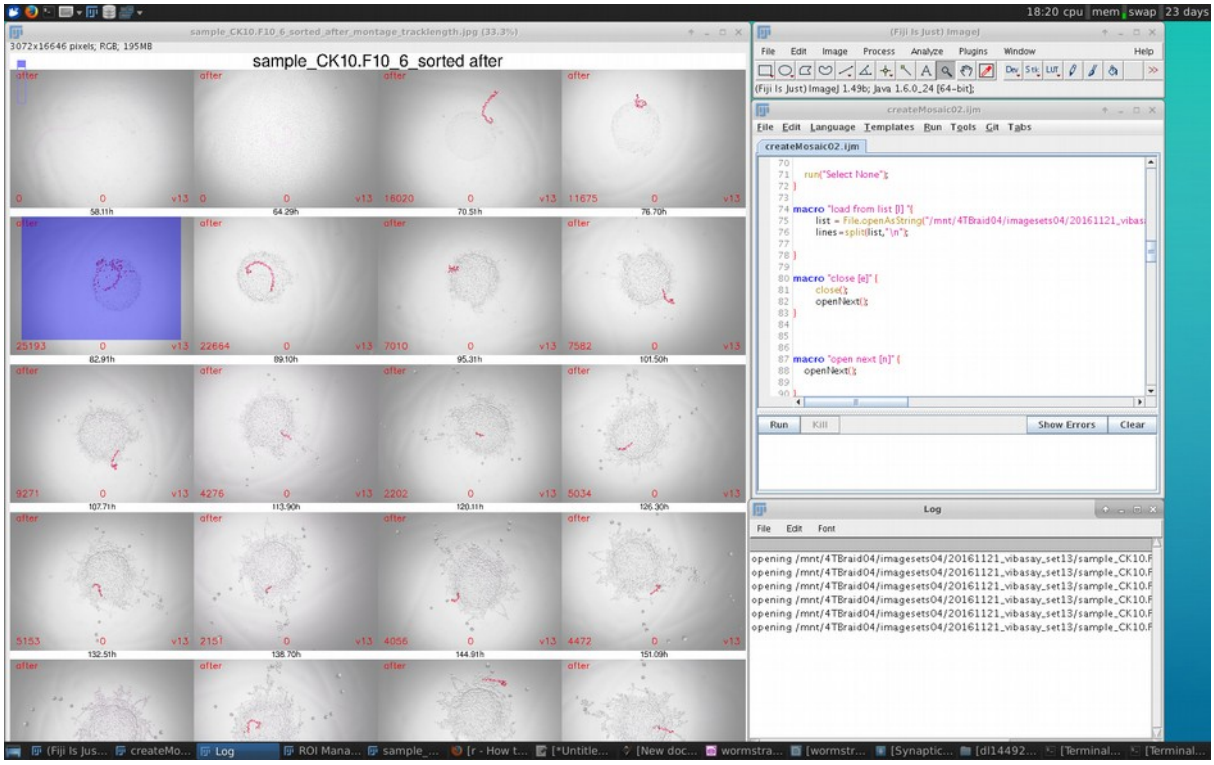

Figure 50: Manual Censoring of RAPID Data

ImageJ is used to display the mosaic assemblies of all time points of each worm and visually inspected. Thresholding artifacts are identified and censored, which is indicated with a purple rectangular overlay. After censoring is complete, ImageJ will write the censoring state for each time point in a text file within the folder of this particular timepoint. In this example, only the first 16 time points of >100 timepoints recorded for this worm are visible. The mosaics are presented in a scrollable window and censoring is performed interactively by pointing at a given time point and pressing a key.

After processing and censoring, the folder contains the following files:

```
dl1449254930_1_1_3
├── camera.txt
├── imgseries_h264.AVI_2fps.AVI
├── imgseries_h264.AVI_2fps.AVI_0_25_before.jpg
├── imgseries_h264.AVI_2fps.AVI_0.jpg_before_overlay.jpg_tracklength.jpg
├── imgseries_h264.AVI_2fps.AVI_27_55_after.jpg
├── imgseries_h264.AVI_2fps.AVI_27.jpg_after_overlay.jpg_tracklength.jpg
├── imgseries_h264.AVI_metadata.txt
├── sampleID.txt
├── temperature.txt
├── timestamp.txt
├── trackLength.tsv
└── version.txt
```

The .AVI file contains the compressed raw image data, the .jpg files result from the image processing, track area, number of contours and edge indication are summarized in the .tsv file. The .txt files contain various meta data relating to the recording conditions such as sample id, current time, temperature, camera serial number, imaging platform etc. Once a run has finished and image processing and censoring are complete, all data is gathered using R and compiled in a single data frame. The data frames of each run can be combined for statistical evaluation and modeling. The structure and information contained in this data frame is shown in Table 25.

Column	Type	Example
sampleID	factor	SS104_143
birthTimestamp	num	1449086400
currentTimestamp	num	1449427804
trackVersion	factor	trackVersion.v13
beforeLength	num	0
beforeArea	num	5210
beforeEdge	num	0
beforeContours	num	140
afterLength	num	0
afterArea	num	20398
afterEdge	num	0
afterContours	num	46
trackCensoredBefore	factor	NA
trackCensoredAfter	factor	NA
cameraSerial	factor	860869D768724772A766819D1BAD8411
cameraVersion	factor	0.9
device	factor	3

Column	Type	Example
temperatureAssay	num	28.75
temperatureTable	num	27.5
setID	factor	2
days	num	3.950845
groupID	factor	SS104
date	num	06.12.15 19:49
genotype	factor	no Tau
HT7	factor	no HT7

Table 25: Data Frame Structure and Examples

Columns of the *R* data frame in which all assay data is collected for visualization and statistical analysis. Each row of the data frame contains all information for a specific measurement. Factor indicates a categorical variable with distinct levels, while num stands for continuous variables, NA indicates a missing entry. Certain columns such as beforeLength and afterLength are placeholder and not yet populated. Columns below temperatureTable are constructed from other columns or added by the user.

7.5 Development of RAPID

The development of RAPID has gone through various design stages before we arrived at the current implementation (Figure 51).

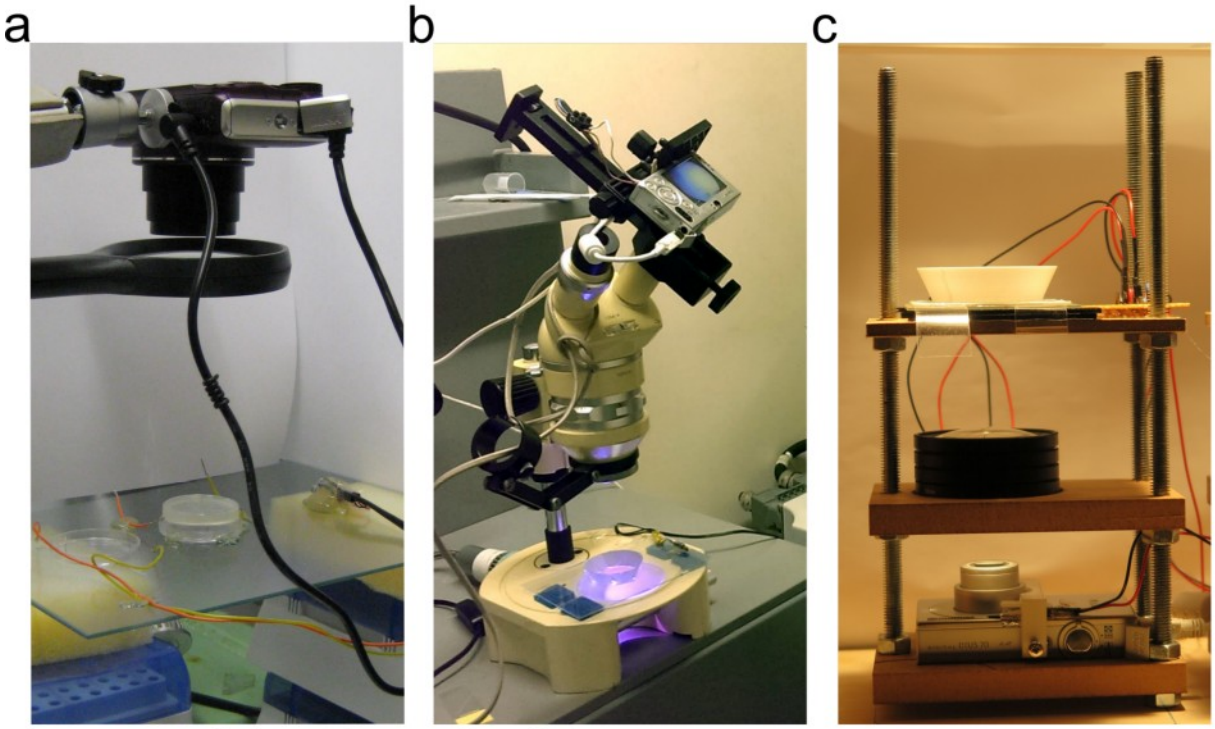

Figure 51: Evolution of the Imaging Platform

Evolution of the imaging platforms for stimulated locomotor assessment. The first prototype (a) was operated manually by putting plates on to the plate holder and the assay was performed recording videos through a magnifying glass and the vibration motor was directly controlled by a computer. This version was used to evaluate provoked locomotion using vibratory stimuli. The next version (b) was constructed from a stereo microscope with camera adapter and plates were handled by a robotic arm (Figure 53) to load and unload plates from the stereo microscope, allowing longitudinal recordings for the first time. The vibration motor was switched by the robot controller and the setup was limited to one imaging device. Current version of the imaging platform (c) termed RAPID. The vibration motor is directly controlled by the camera, enabling multiplexing of the imaging stages and independent operation.

The first version of the imaging platform was used to evaluate the effectiveness of a vibratory stimuli to provoke locomotion of the worms (Figure 52).

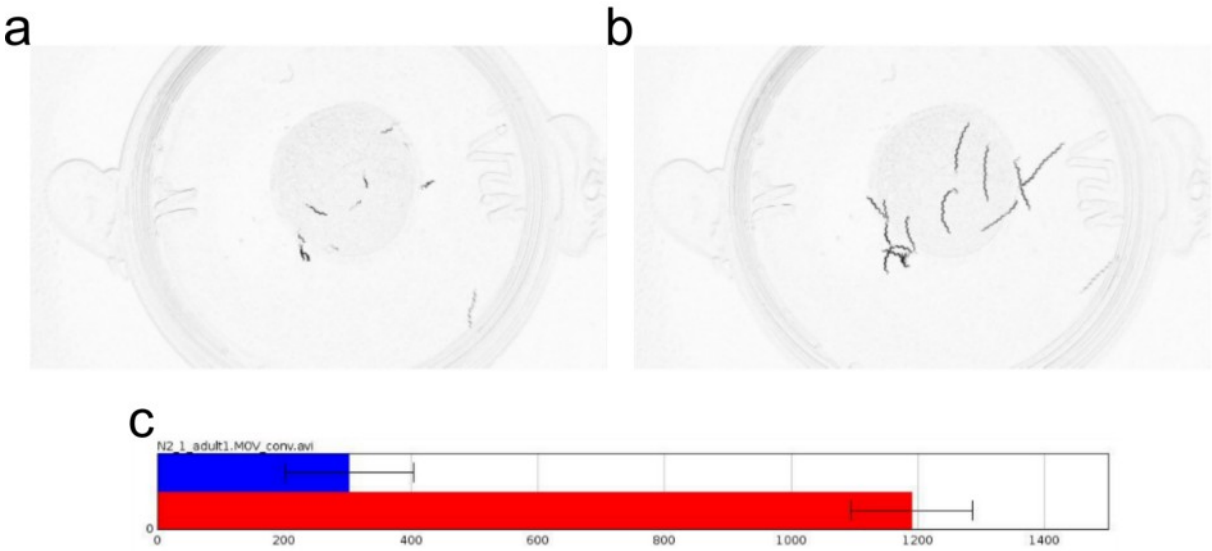

Figure 52: Prototype of Track Area Extraction

Early version of track extraction using image subtraction on videos recorded using the first imaging platform (Figure 51 a). Track area before (a) and track area after stimulus (b) are compared (c). From these experiments we concluded to switch to locomotor assessment on single worms, since the number of worms can not be reliably determined due to overlapping tracks.

Switching to single worm recordings prompted us to develop an automated plate switching device. The solution was the use of a robotic arm in combination with a stereo microscope (Figure 53).

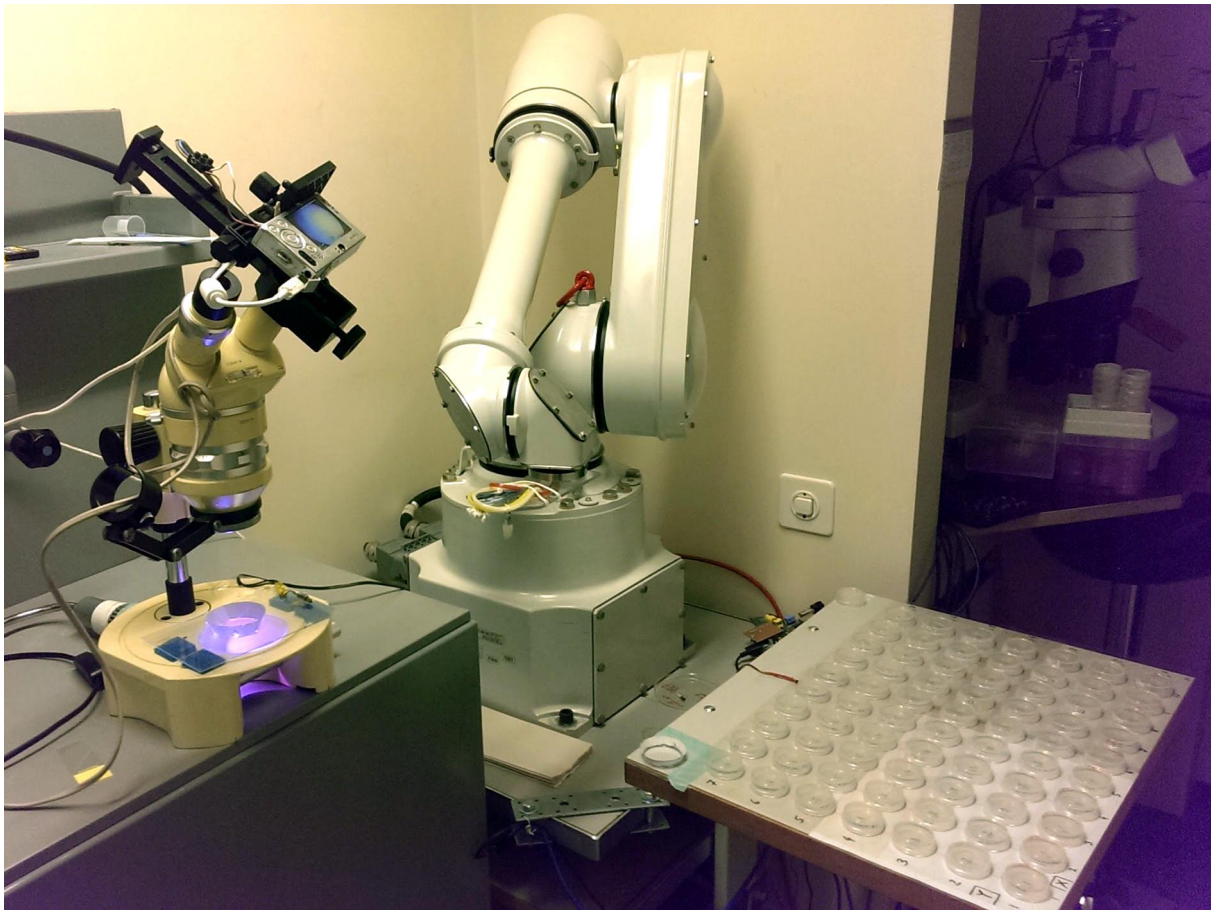

Figure 53: Prototype of Automated Locomotion Assessment

First version of an automated locomotion assessment capable of recording 70 plates using the same camera as the current version of RAPID in combination with a stereo microscope. This enabled longitudinal locomotor performance recordings. Since the capacity was limited to 70 plates, we developed a more compact imaging platform, enabling parallel recordings of several plates at the time.

While this version worked well, the plate capacity was limited to 70 plates per run. In order to record all the generated strains in a reasonable amount of time, we had to increase the capacity and multiplex the image acquisition. Since we did not have four identical stereo microscopes and only limited space, we developed a more compact imaging platform from generally available components (Figure 51 c).